

Dissertation
submitted to the
Combined Faculty of Natural Sciences and Mathematics
of the Ruperto Carola University Heidelberg, Germany
for the degree of
Doctor of Natural Sciences

Presented by Mgr Jakub Czuchnowski
born in: Kraków, Poland
Oral examination on 25.03.2021 Heidelberg, Germany

**Establishing a high-sensitivity
photoacoustic tomography system for
applications in life sciences**

Referees: Dr. Martin Jechlinger

Prof. Dr. Ana Martin-Villalba

Abstract

Understanding biology across various spatial scales requires appropriate tools that allow the collection and analysis of information about specific events throughout the organism of interest. Imaging techniques are one of the most powerful tools of modern biology enabling direct visualisation of structures and processes with high spatial resolution and often in real time. Especially potent imaging modalities were developed based on light microscopy that allow high resolution imaging in the cellular and subcellular regimes. Unfortunately, these techniques are not suitable for imaging in highly scattering and thick samples such as mammalian tissues. While those can be imaged by biomedical imaging techniques such as MRI or CT, they typically achieve much lower lowered spatial and temporal resolution as well as are incompatible with the large toolkit of molecular probes and approaches used in life sciences (e.g. fluorescent proteins).

Here, emerging technologies based on photoacoustic imaging (where light is used to excite acoustic waves inside the tissue) enable bridging the biomedical and biological techniques by combining light based excitation (that is compatible with the optical toolkit of life sciences) with deep penetration capabilities characteristic for the biomedical regime. Several techniques of photoacoustic imaging were developed with photoacoustic tomography emerging as a particularly interesting modality for large-volume, high-quality imaging in mammalian tissues, due to its ability to simultaneously record information from the whole volume of interest. In particular, there is a rising interest in developing all-optical photoacoustic approaches which use light both for exciting and detecting the acoustic waves. These bring promise of simplification and miniaturisation of the detector elements which would allow for easier animal handling and enable combination with other light based modalities such as multiphoton microscopy.

The aim of this thesis was to establish a high-performance state-of-the-art all-optical photoacoustic system based on a Fabry-Pérot pressure sensor that could be used in life sciences for imaging applications in mouse biology. In particular, I explored possible improvements in speed and sensitivity with the long-term goal to enable whole-brain calcium based neuroimaging in mice. In this thesis, I describe my work towards the realization of this system including the detailed discussion of the system design and operating principles. I show preliminary imaging experiments in fish and mice to validate the capabilities of our photoacoustic tomography setup to perform high resolution *in vivo* imaging.

The main part of the thesis is then concerned with the description of various approaches for increasing photoacoustic tomography sensitivity, including the use of adaptive optics for enhanced cavity coupling, passive photodiode amplification as well as deep learning based denoising. Furthermore, a full theoretical framework is presented for explaining the effects of interactions between optical aberrations and Fabry-Pérot cavity modes, which is then extended to explain fundamental optical processes in adaptive optics. Moreover, two frameworks are described for increasing the volume rate of Fabry-Pérot based systems including optimising the scanning trajectory as well as using optical multiplexing for parallel readout from the sensor. Finally, further directions of work are discussed including tackling the effects of skull induced acoustic aberrations on the image resolution and the choice of possible candidates for photoacoustic calcium sensors.

Zusammenfassung

Das Verständnis der Biologie über verschiedene räumliche Skalen hinweg erfordert geeignete Werkzeuge, mit denen Informationen über bestimmte Ereignisse im gesamten Organismus von Interesse gesammelt und analysiert werden können. Bildgebende Verfahren sind eines der leistungsfähigsten Werkzeuge der modernen Biologie und ermöglichen die direkte Visualisierung von Strukturen und Prozessen mit hoher räumlicher Auflösung und häufig in Echtzeit. Auf der Grundlage der Lichtmikroskopie wurden besonders wirksame Bildgebungsverfahren entwickelt, die die hochauflösende Abbildung im zellulären und subzellulären Bereich ermöglichen. Leider sind diese Techniken nicht für die Bildgebung in stark streuenden und dicken Proben wie Säugetiergeweben geeignet. Diese können zwar durch biomedizinische Bildgebungstechniken wie MRT oder CT abgebildet werden, allerdings erreichen diese Verfahren typischerweise eine viel geringere räumliche und zeitliche Auflösung und sind nicht kompatibel mit dem großen Toolkit molekularer Sonden und Ansätzen, die in den Biowissenschaften verwendet werden (z. B. fluoreszierende Proteine).

Hier ermöglichen neue Technologien, die auf der photoakustischen Bildgebung basieren (bei der Licht zur Anregung von Schallwellen im Gewebe verwendet wird), die Überbrückung der biomedizinischen und biologischen Techniken, indem sie lichtbasierte Anregung (die mit dem optischen Toolkit der Biowissenschaften kompatibel ist) mit hoher Penetrationsfähigkeit wie sie typisch für das biomedizinische Regime ist kombinieren. Es wurden verschiedene Techniken der photoakustischen Bildgebung entwickelt, wobei sich die photoakustische Tomographie als besonders interessante Modalität für die großvolumige, qualitativ hochwertige Bildgebung in Säugetiergeweben herausstellte, da sie gleichzeitig Informationen aus dem gesamten Volumen von Interesse aufzeichnen kann. Insbesondere besteht ein wachsendes Interesse an der Entwicklung rein optischer photoakustischer Ansätze, bei denen Licht sowohl zur Anregung als auch zur Erfassung der Schallwellen verwendet wird. Diese versprechen eine Vereinfachung und Miniaturisierung der Detektorelemente, die eine einfachere Handhabung der Versuchstiere ermöglichen und die Kombination mit anderen lichtbasierten Modalitäten wie der Multiphotonenmikroskopie ermöglichen würden.

Ziel dieser Arbeit war es, ein hochleistungsfähiges rein optisches photoakustisches System auf dem neuesten Stand der Technik zu etablieren, das auf einem Fabry-Pérot-Drucksensor basiert und in den Biowissenschaften für bildgebende Anwendungen an Mäusen eingesetzt werden kann. Insbesondere untersuchte ich mögliche Verbesserungen der Geschwindigkeit und Empfindlichkeit mit dem langfristigen Ziel, eine auf Kalzium basierende Bildgebung des gesamten Gehirns bei Mäusen zu ermöglichen. In dieser Arbeit beschreibe ich meine Arbeit zur Realisierung dieses Systems einschließlich einer detaillierten Diskussion des Systemdesigns und der Funktionsprinzipien. Ich zeige vorläufige Bildgebungsexperimente an Fischen und Mäusen, um die Fähigkeiten unseres photoakustischen Tomographie-Setups zur Durchführung einer hochauflösenden *in vivo* Bildgebung zu validieren.

Der Hauptteil der Arbeit befasst sich dann mit der Beschreibung verschiedener Ansätze zur Erhöhung der Empfindlichkeit der photoakustischen Tomographie, einschließlich der Verwendung adaptiver Optiken für eine verbesserte Hohlraumkopplung, passive Photodiodenverstärkung sowie Deep Learning-basiertes Entrauschen. Darüber hinaus wird ein vollständiger theoretischer Rahmen zur Erklärung der Auswirkungen von Wechselwirkungen zwischen optischen Aberrationen und Fabry-Pérot-Hohlraummoden vorgestellt, der dann erweitert wird, um grundlegende optische Prozesse in der adaptiven Optik zu erklären. Darüber hinaus werden zwei Ansätze zur Erhöhung der Volumenrate von Fabry-Pérot-basierten Systemen beschrieben, einschließlich der Optimierung der Abtasttrajektorie sowie der Verwendung von optischem Multiplexing zum parallelen Auslesen vom Sensor. Abschließend werden weitere Arbeitsrichtungen diskutiert, darunter die Untersuchung der Auswirkungen schädelinduzierter akustischer Aberrationen auf die Bildauflösung und die Auswahl möglicher Kandidaten für photoakustische Calciumsensoren.

Acknowledgements

I would like to thank my supervisor, Robert, for believing that a biologist can build a microscope. I learned a ton during my PhD all thanks to the fact that you welcomed me into your group. Thank you for supporting so many of my crazy ideas and side projects, I am very happy that at least some of them worked... It has been a great pleasure to do a PhD in the Prevedel lab!

Many thanks to my Thesis Advisory Committee, Prof. Dr. Paul Heppenstall, Dr. Martin Jechlinger, Prof. Dr. Ana Martin-Villalba, Dr. Robert Prevedel who helped me gain a more biological perspective on my very technical project.

I had a opportunity to be a part of a great lab and I am thankful to all my lab members for creating an environment that made my PhD not just bearable but fun, enjoyable and motivating. I learned a lot during our whiteboard discussions and hope to keep in touch with you after I leave!

I received a lot of support from the EMBL community and would like to thank the EMBL Heidelberg mechanical and electronic workshops as well as the animal facilities for help and support. I would like especially thank Christian Kieser for his work on the development of multichannel pre-amplifier boards used in the multibeam photoacoustic tomography system and Marta Garcia Montero for her help with cell lines and tumour injections without which my thesis would lack a solid chunk of data.

I would like to further thank Florian Mathies, Johannes Zimmermann, and Gerardo Hernandez-Sosa from InnovationLab Heidelberg as well as Karl-Phillip Strunk and Jana Zaumseil from the Centre for Advanced Materials, Heidelberg University, for help with manufacturing of the Fabry-Pérot interferometers used in this thesis.

I want to express my gratitude to my friends for all the time we spend together, playing games but not only!

It is difficult for me to express how grateful I am to my Parents and Family for their support throughout my academic path, I would not be a scientist if it weren't for them. I am happy to tell them that my work here is done as I know they felt the struggles of my PhD almost as much as I did.

I hope everyone has in their life something that makes them want to wake up in the morning, for me this something is Ewa. All in all, a PhD is a pretty hardcore experience of endless work, anticipation and disappointments, but throughout all of that never did I have a day when I felt completely hopeless or crushed and it was all thanks to you. The feeling of not being alone in all of this is more than words can describe.

Contents

Abstract	iii
Zusammenfassung	v
Acknowledgements	vii
1 Introduction	1
1.1 Motivation	1
1.1.1 Importance of imaging	1
1.1.2 Problem of scattering	1
1.1.3 Photoacoustic imaging	2
1.1.4 Photoacoustic computed tomography	3
1.1.5 Interferometry based acoustic wave detection for fast photoacoustic imaging	4
1.2 Aims and Objectives	5
1.3 Thesis structure	5
2 Introduction to photoacoustic imaging	7
2.1 Photoacoustic effect	7
2.2 Photoacoustic imaging	7
2.3 Types of photoacoustic imaging techniques	9
2.3.1 Photoacoustic microscopy	9
Optically-resolved photoacoustic microscopy (OR-PAM)	10
Acoustically-resolved photoacoustic microscopy (AR-PAM)	10
2.3.2 Photoacoustic tomography	10
2.4 Sound wave detection in photoacoustic imaging	11
2.4.1 Ultrasound transducers	11
2.4.2 Optical detection of ultrasound	11
2.5 Sound wave detection using Fabry-Pérot interferometers	11
2.5.1 Interferometer Transfer Function	12
The coefficient of finesse and the sensitivity of the FPI	12
2.6 Image reconstruction in Photoacoustic Tomography	14
2.6.1 Image reconstruction in FPI-PAT	14
3 Photoacoustic tomography system design	15
3.1 Fabry-Pérot interferometer fabrication	15
3.1.1 Cavity inhomogeneities	16
3.2 Interrogation light path	16
3.2.1 Multi-beam PAT system (M-PAT)	17
3.2.2 Single-beam PAT system (S-PAT)	18
3.2.3 Upright PAT (uPAT) versus inverted PAT (iPAT)	19
3.3 Excitation laser	19
3.4 Interrogation laser	20

3.5	Photodetectors and data acquisition	21
4	Photoacoustic system validation	23
4.1	Characterisation of Fabry-Pérot Interferometers	23
4.1.1	Sensitivity of FPI based PAT systems	23
4.1.2	Optical sensitivity	24
	Quantification of sensitivity from experimental data	24
4.1.3	Optimal wavelength	25
4.1.4	Optimal working point of the photodetector	25
	Loss of effective SNR due to working point distribution	26
4.2	Effects of temperature on system performance	27
4.2.1	Effects of cavity expansion on an ideal FPI	27
4.2.2	Consequences for PAT	28
	Fast re-characterisation	28
	Validation of the re-characterisation scheme	29
4.3	First acoustic measurements	30
4.4	Preliminary imaging of small organisms	30
4.5	Preliminary imaging of mice	31
4.5.1	Photoacoustic imaging and image reconstruction	33
4.6	Longitudinal tracking of tumour progression in mice using multispectral photoacoustic tomography	34
4.6.1	Multispectral photoacoustic tomography	34
	Linear unmixing	34
4.6.2	Tracking melanoma growth in nude mice	36
5	Improving sensitivity of Fabry-Pérot based photoacoustic systems	39
5.1	Understanding the effects of aberrations on the FPI sensitivity	39
5.1.1	Theoretical approach	40
5.1.2	Effects of beam aberrations on FPI sensitivity	43
	Limit case for ideal FP cavity illuminated with a non-diverging beam	43
	Case of an ideal FP cavity illuminated with a diverging beam	46
5.1.3	Effects of cavity aberrations on FPI sensitivity	47
5.1.4	Active and passive aberration correction in FPI systems	53
	Beam aberrations	53
	Cavity aberrations	53
	Experimental validation	54
5.1.5	Discussion	55
5.2	Applying Adaptive optics enhancement in photoacoustic tomography	56
5.2.1	Correction of DM induced focal shifts	56
	Predicting the spot drift	57
5.2.2	Indirect wavefront sensing with iterative refinement	60
5.2.3	Adaptive-optics enhanced photoacoustic imaging	62
5.2.4	Discussion	63
5.3	Comparison of free-space and fibre-coupled detectors for FPI-PAT	65
5.3.1	Correlative characterisation of the FPI	66
5.4	Reducing noise in FP-PAT	67
5.4.1	Reducing electronic noise in photodiode detectors by passive signal amplification	67
5.4.2	Deep learning for signal denoising	69
5.4.3	Outlook	70

6	Improving speed of Fabry-Pérot based photoacoustic systems	71
6.1	Tuning dependent dead-time	71
6.1.1	λ_{opt} binning	72
6.1.2	Optimising scan path length with the use of a modified 2opt algorithm	73
6.1.3	Validation of fast imaging	74
6.2	Optical multiplexing	74
6.2.1	Limitations of multiplexing	75
6.2.2	Multibeam generation using a microlens array	75
	Multichannel readout using a laser line	76
6.2.3	Characterisation of the FPI using M-PACT	76
6.2.4	Measuring ultrasound signals using M-PACT	77
6.2.5	Discussion	78
7	Outlook	79
7.1	Improving resolution of Fabry-Pérot based photoacoustic systems	79
7.1.1	Factors limiting resolution of FP-PAT	79
	Acoustic aberrations	80
7.1.2	Modelling the effects of acoustic aberrations on the PAT PSF	80
7.1.3	Tackling aberration induced loss of resolution	81
	Prior based reconstruction	81
	Experimental acquisition of the prior using a dual-modality approach	81
7.2	Photoacoustic imaging of genetically encoded calcium indicators	82
7.2.1	Inferring PA signal quality from photo-physical properties of GECIs	82
8	Conclusions	85
A	Fundamental cross-compensation of Zernike aberrations	87
A.1	Coupling between Zernike aberrations and Laguerre-Gauss modes in the low aberration regime	87
A.1.1	Generalised Adaptive-Optics task	88
A.1.2	Correcting multiple cross-compensating aberrations	90
A.2	Cascading aberrations and the high aberrations regime	92
A.2.1	Translation to experimental quality metrics	92
B	Alternative fast all-optical methods	95
B.1	Space-to-time mapping (S2T)	95
B.1.1	Advantages	96
B.1.2	Challenges	96
B.1.3	Conclusions	97
B.2	Time-to-space mapping (T2S)	97
B.2.1	Advantages	97
B.2.2	Challenges	98
B.2.3	Conclusions	98
	Bibliography	99

List of Figures

1.1	The mechanism for measuring acoustic waves using the FPI interferometer	4
2.1	Scheme comparing different photoacoustic imaging modalities to fluorescent microscopy	9
2.2	The reflection interferometer transfer function modeling the behaviour of an ideal FPI	12
2.3	Dependence of the reflectivity on the change in cavity thickness for a fixed laser wavelength	13
2.4	Dependence of the shape of ITF on the interferometer finesse	13
2.5	Dependence of the shape of ITF derivative on the interferometer finesse	14
3.1	Optical quality measurements of the FPI	16
3.2	Design of the multi-beam PAT system	17
3.3	Optical and optomechanical design of the M-PAT system	17
3.4	Comparison of design performance with experimentally measured PSF	18
3.5	Validation of system resolution across the scan grid	18
3.6	Optical design of the S-PAT system	19
4.1	Optimal working point of the photodiode	26
4.2	λ_{min} dependence on temperature	28
4.3	λ_{opt} dependence on sample presence and excitation light	29
4.4	Validation of the re-characterisation scheme	30
4.5	Acquired pressure signals	31
4.6	Acquired PA pressure signal	31
4.7	Zebrafish embryo imaging	32
4.8	Label free mouse imaging	33
4.9	Absorption spectra of melanin and haemoglobin	34
4.10	Validation of the linear unmixing scheme	35
4.11	Tracking melanoma growth in nude mice	36
4.12	Comparing linear and PCA based spectral unmixing methods	37
5.1	Interaction between optical aberrations and cavity modes	41
5.2	Volume under the absolute value of the Zernike polynomial (VuP) . . .	46
5.3	Effects of beam aberrations	48
5.4	Effects of cavity aberrations	49
5.5	Validation of the non-divergence approximation	50
5.6	Characterization of FPI sensitivity improvement using active and passive aberration correction	52
5.7	Experimental validation scheme	54
5.8	Effects of Zernike modes on focal spot shift	57
5.9	Correcting the focal spot shift	58
5.10	Comparison of focal shift corrections	59

5.11	Characterisation of the AO improvement	61
5.12	Modeling the adaptive optic refinement with a saturating function . .	62
5.13	Optimal working point characterisation for the AO system	63
5.14	Effects of AO correction on PA signals and images	64
5.15	Correlative free-space fiber-coupled setup	65
5.16	Comparison of the sensitivity across a FPI sensor between a fibre-coupled and free-space photodiode.	66
5.17	Shift of the optimal wavelength (λ_{opt}) between a fibre-coupled and a free-space photodiode	66
5.18	Optimal working point comparison between a fibre-coupled and a free-space photodiode	67
5.19	Noise reduction using passive signal amplification	68
5.20	PA signal denoising using N2V	69
6.1	Dependence of sensitivity on spectral distance from λ_{opt}	71
6.2	Wavelength sorting drastically reduces required number of tunings . .	72
6.3	Optimisation of scan path	72
6.4	Validation of the trajectory optimisation scheme	75
6.5	Multibeam setup using a microlens array multibeam generator	76
6.6	Multibeam setup using a laser line generator	77
6.7	12-beam characterisation of the FPI	77
6.8	Parallel 4-beam recording of US waves using M-PACT	78
7.1	Comparison of PA image reconstruction schemes for trans-cranial PAT	80
7.2	Scheme of the dual-modality Optical Coherence - Photoacoustic Tomography system	81
7.3	Absolute brightness change for various GECIs	83
A.1	Description of Zernike cross-compensation in the weak aberration regime	89
A.2	Description of Zernike cross-compensation in the strong aberration regime	91
B.1	Space-to-time mapping	95
B.2	The principle of Time Encoded Interferometry	96
B.3	Time-to-space mapping	97

List of Tables

1.1	Advantages and disadvantages of various deep imaging strategies . . .	2
2.1	Similarities and differences between fluorescence imaging and photoacoustic imaging	8
2.2	Comparison of main types of photoacoustic imaging	9
3.1	Dependence of the volumetric imaging rate on the excitation laser PRR	20
7.1	Speed of sound in biological tissues	79
7.2	Comparison of abstract model calcium indicators	82
7.3	Comparison of real GECI	83

List of Abbreviations

AO	Adaptive Optics
aPDs	amplified PhotoDiodes
AR-PAM	Acoustically-Resolved PhotoAcoustic Microscopy
BF	Bright Field
bPDs	biased PhotoDiodes
CV	Continuous Wave
DM	Deformable Mirror
dps	days post fertilization
DSP	Desired Scan Position
FCI	Fluorescent Calcium Indicator
FCNN	Fully Connected Neural Network
FLM	Fluorescent Light Microscopy
FPGA	Field Programmable Gate Array
FPI	Fabry-Pérot Interferometer
FP-PAT	Fabry-Pérot (based) PhotoAcoustic Tomography
FWHM	Full-Width (at) Half-Max
iPAT	inverted PhotoAcoustic Tomography
G	Gaussian beam
GBMA	Gaussian Beam Mode Analysis
ITF	Interferometer Transfer Function
LIN	Linear Model
MFP	Mean Free Path
MLA	MicroLenses Array
M-PAT	Multi-beam PhotoAcoustic Tomography
NIR	Near-InfraRed light
NN	Neural Network
OCT	Optical Coherence Tomography
OR-PAM	Optically-Resolved PhotoAcoustic Microscopy
PA	PhotoAcoustic
PAI	PhotoAcoustic Imaging
PAM	PhotoAcoustic Microscopy
PAT	PhotoAcoustic Tomography
PSF	Point Spread Function
PRR	Pulse Repetition Rate
SLM	Spatial Light Modulator
SNR	Signal-to-Noise-Ratio
SoS	Speed-of-Sound
S-PAT	Single-beam PhotoAcoustic Tomography
TMFP	Transport Mean Free Path
uPAT	upright PhotoAcoustic Tomography
US	UltraSound
USI	UltraSound Imaging
UST	UltraSound Transducer

VIS	VISible
vps	volume per second
VuP	Volume under Polynomial

For my parents

Chapter 1

Introduction

1.1 Motivation

1.1.1 Importance of imaging

'Seeing is believing' is probably the most widely used phrase to highlight the importance of imaging in science. While 'believing' is not yet 'understanding', it is undeniable that countless biologists were inspired by the insights enabled by microscopes ever since Antonie van Leeuwenhoek introduced their use in biology in the 17th century. Since then the developments of fluorescence microscopy and digital storage and post-processing of images revolutionised the field of biological imaging and opened new possibilities. 'Seeing' transformed into 'storing and analysing' changed microscopy from a qualitative tool into a source of complex, multi-dimensional quantitative data (Kherlopian et al., 2008). As the achievable spatial and temporal resolution increase, imaging dynamic processes with molecular sensitivity may be more readily achieved (Gwosch et al., 2020). Additionally, imaging data can even become the basis for quantitative modeling of protein kinetics or biochemical signaling networks (Eils and Athale, 2003). However, there is a caveat to all this.

1.1.2 Problem of scattering

Classical wide-field microscopy is useful only in case of thin and transparent samples ($\leq 10 \mu\text{m}$). This physical limit can be derived from a parameter called the mean free path (MFP) of a photon, which describes the average distance a photon can travel in a particular material without being scattered (Ntziachristos, 2010). Unfortunately, in biological tissues light is strongly scattered in several important spectral regions (the UV [$<450 \text{ nm}$], the VIS [$450\text{-}650 \text{ nm}$] and the NIR [$650\text{-}1000 \text{ nm}$]) which poses severe problems for imaging at depth. Typically the MFP for those wavelengths is $\approx 100 \mu\text{m}$, although it may vary dependent on the tissue type. As a result of this, imaging needed to be constrained to $10 - 20 \mu\text{m}$ thick samples to ensure low scattering and high image quality.

The developments of both confocal and multiphoton microscopy have pushed deep imaging much beyond the $20 \mu\text{m}$ limits of wide-field microscopy. The penetration limit for these advanced modalities can be described by another physical parameter, namely the transport mean free path (TMFP) which describes the average propagation distance after which the photon loses relation to the propagation direction it had before entering the tissue (Ntziachristos, 2010). The TMFP (usually ≈ 10 MFP) marks the threshold after which light is completely diffuse and therefore single photons no longer carry any significant information that could be exploited for image formation.

	Approaches	Advantages	Disadvantages	Source
(1)	MR and X-ray imaging	Extreme depths ($> 10\text{ cm}$)	Small variety of reporters and labels	Lustig, Donoho, and Pauly, 2007; Fred, 2004
(2)	Ultrasound imaging	Large depths ($\geq 1\text{ cm}$); High mesoscopic spatial resolution ($< 100\ \mu\text{m}$)	Contrast is non-optical; Small variety of reporters and labels	Wells, 2006; Fenster, Downey, and Cardinal, 2001
(3)	Optical clearing	Compatible with a variety of optical systems and samples	Depending on the sample the improvement might be moderate; Chemically alters the sample	Costantini et al., 2019; Wen et al., 2010
(4)	Adaptive optics	Compatible with a variety of optical systems and samples	Challenging to setup and operate; Requires complex hardware and software	Booth, 2007; Booth, 2014
(5)	Fluorescence tomography	Compatible with standard fluorescent molecules	Relatively poor image quality; Strong assumptions on the tissue optical properties	Ozturk et al., 2013; Deliolanis et al., 2007

TABLE 1.1: Advantages and disadvantages of various deep imaging strategies

Imaging beyond the optical TMFP remains challenging, but can be achieved in a multitude of ways: **(1)** the wavelength of light used for imaging can be changed to achieve deep penetration (e.i. radio waves, X-rays); **(2)** the nature of the carrier of information can be changed altogether (e.i. ultrasound); **(3)** tissue properties might be altered to reduce scattering (i.e. in vivo clearing); **(4)** effects of scattering might be counteracted by adaptive optics; **(5)** statistical information might be extracted from large populations of photons that allows for modelling optical properties of the tissue (i.e. fluorescence tomography). All of these approaches have distinct advantages and disadvantages that will determine which will be the solution of choice in a particular application (**Table 1.1**). Unfortunately, no ideal technique exists, however, it always possible to select the best possible approach by carefully considering the requirements of each individual imaging task. For applications in life sciences a technique is required which combines molecular specificity than can be achieved with optical excitation with deep penetration capabilities which are incompatible with standard fluorescence. Ultrasound, on the other hand, provides very deep imaging capabilities and high resolution, but lacks the specificity of fluorescent imaging. Thus, a hybrid approach is beneficial which combines optical excitation which ultrasound emission allowing for deep high-resolution imaging with molecular specificity. This approach, dubbed photoacoustic imaging, will be the main focus of this thesis.

1.1.3 Photoacoustic imaging

Photoacoustic imaging is based on the namesake effect, first described by Alexander Graham Bell in the 1880. When a short pulse of light is absorbed by molecules within a tissue it causes a rapid local rise in temperature, which in turn is converted into a sound or pressure wave via a thermoelastic expansion of the absorbing volume. These sound waves typically have a very broad range of frequencies (between 1-100 MHz) which encode information regarding the size and concentration of the

absorber. These sound-waves can be then detected using approaches similar as in ultrasound imaging (USI) or by other methods developed specifically for photoacoustic imaging (PAI). The advantages of PAI are numerous - by using absorption-based contrast in the visible and infrared range, PAI can make use of the wide range of already available fluorescent probes including genetically encoded fluorescent proteins. Additionally, because fluorescence is not required for PAI, also chromophoric molecules can be used. This allows imaging of a number of endogenously present contrast agents such as lipids (allowing e.g. differentiation of myelin rich axons of neurons from other tissue), melanin (allowing label free detection of melanomas) and probably the most widely used one, hemoglobin (allowing label-free visualization of vasculature). Furthermore, imaging at different excitation wavelengths enables multicolor imaging similar to fluorescence microscopy and enables differentiation of molecular content. Also, absorbance differences between oxy- and deoxy-hemoglobin allows hemodynamic measurements of brain activity.

1.1.4 Photoacoustic computed tomography

One of the most useful modalities of PAI is called photoacoustic computed tomography (PACT). It can achieve 50-100 μm resolution while imaging up to 1 cm in depth, and provides big fields of view that enable whole body imaging of mice and other small animals. This, combined with specific contrast agents makes possible dynamic longitudinal studies of tumor growth, blood flow and brain oxygenation. Despite the wide horizon of applications there are still many technical difficulties which need to be overcome in order to fully realize the potential of this technique.

To achieve high imaging speeds PACT requires a large number of acoustic detectors for measuring the sound waves emitted by the sample. The current solution to this problem is the use of an ultrasound transducer array (USTA) adopted from the field of USI. However, this solution is impractical for a number of reasons. Firstly, to ensure an omnidirectional response of the detectors their size must be smaller than the wavelength of the measured sound waves ($< 100 \mu\text{m}$). However, such small USTs suffer from very low sensitivity. Secondly, USTA are bulky and non-transparent, thus obstructing direct optical access required for the delivery of excitation light. Finally, densely packed arrays suffer from electronic crosstalk between channels, effectively degrading image quality. The limitations of the USTA can be overcome by optical methods for sound wave detection. In these approaches, it is possible to retrieve the optical access either by contact-free detection or by using optically transparent materials for detector manufacturing. As the size of the detecting elements is further limited only by diffraction (theoretically to below $1 \mu\text{m}$), also the electronics can be spatially decoupled from the detection surface preventing electronic crosstalk. Current implementations of optical based detection methods are used with single recording channel approaches, which result in low imaging speeds. This represents the most limiting drawback of this technique. Therefore, in our project we decided to develop a high-speed version of such an optical detection PACT. Our technical approach to scale up imaging speed is based on simultaneous, multichannel detection system realized by optical multiplexing. In the following, I will elaborate on our approach and strategy to realize such an imaging system and demonstrate its potential in cutting-edge biomedical research.

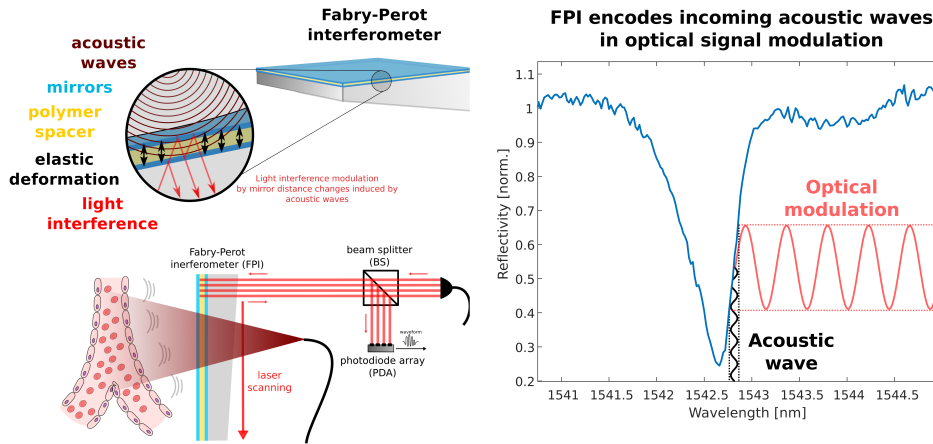


FIGURE 1.1: **The mechanism for measuring acoustic waves using the FPI interferometer.** As the spacer is elastically deformed by the incident acoustic wave, this effectively translates the acoustic wave into an optical interference signal. Based on the knowledge of the elastic properties of the spacer, the light intensity change can be used to calculate the sound-wave induced pressure changes on the detector. Then, by scanning the laser beam across the surface of the interferometer a time-resolved pressure map is acquired. This map encodes all the information necessary for the localization of the acoustic sources within a sample.

1.1.5 Interferometry based acoustic wave detection for fast photoacoustic imaging

We decided to adopt and further develop an optical acoustic wave detection scheme, originally pioneered by Paul Beard and colleagues at UC London (Zhang, Laufer, and Beard, 2008). It uses a specially manufactured planar Fabry-Pérot interferometer as the active element of the detector. This detector is composed of two dielectric mirrors separated by a polymer spacer. When a laser beam probes this interferometer, it undergoes interference – this optical signal can be easily measured using a photodiode. The interference and thus signal strength is dependent on the thickness of the polymer spacer separating the mirrors. As the spacer is elastically deformed by the incident acoustic wave, this effectively translates the acoustic wave into an optical interference signal (**Figure 1.1**). Based on the knowledge of the elastic properties of the spacer the light intensity change can be used to calculate the sound-wave induced pressure changes on the detector. Then, by scanning the laser beam across the surface of the interferometer a time-resolved pressure map is acquired which encodes all the information necessary for the localization of the acoustic sources within a sample.

As described earlier, the PACT optical detection method offers multiple advantages over alternative solutions. This allows for a much denser sampling of the acoustic field than would be possible with USTA, therefore yielding increased image resolution. Also, as the sampling density can be changed easily by the experimenter, and can be adjusted to optimize the imaging performance of a given experiment. The limitation of this approach is the fact that in current implementations only a single interrogation beam is used, which limits the data acquisition speed. To be more quantitative: In order for the pressure field to be sampled with sufficient density, the detection points need to be separated by $\approx 100 \mu\text{m}$ which corresponds to 10,000 points for a field-of-view of 1 cm^2 . As the lasers used for excitation can currently produce only up to 50 pulses per second only 50 points can be scanned within

a second corresponding to a total acquisition time of approximately 200 s. To overcome this significant limitation, we proposed to use optical multiplexing to increase the number of interrogation beams to 46 which combined with a recently available 200 Hz excitation laser would allow us to scan 1 cm² in 1 s. If this can be achieved, dynamic biological processes such as Calcium-mediated brain activity or other dynamic biological processes could be temporally resolved. Similarly, decreasing the image acquisition time to ≈ 1 s greatly reduces imaging artefacts due to breathing motion as it allows the acquisition of the whole 3D volume in between the breaths of a mouse. This will be helpful especially for imaging the body cavity e.g. *in utero* imaging, where substantial tissue movement during breathing is observed.

1.2 Aims and Objectives

The main objective of this thesis was to establish a high-sensitivity all-optical photoacoustic tomography system for life science applications. Secondary objectives were connected to further developing this system in directions of higher imaging speed and further increased sensitivity with the overarching aim of performing photoacoustic-based calcium activity measurements in the mouse brain.

1.3 Thesis structure

The thesis is organised as follows. **Chapter 2** provides a general introduction to photoacoustic imaging with the focus on all-optical photoacoustic tomography and especially the use of Fabry-Pérot interferometers as acoustic detectors. **Chapter 3** describes the system design process outlining the key components (the Fabry-Pérot interferometer itself as well as the interrogation and excitation lasers) and their importance to the overall performance. **Chapter 4** focuses on the validation of said performance first by characterising the properties of the Fabry-Pérot interferometers followed by acoustic measurements and photo-acoustic imaging experiments on live animals. **Chapter 5** describes the efforts to further increase the sensitivity of all-optical photoacoustic measurements by tackling the effects of optical aberrations as well as modifications on the photodetector design and digital denoising methods. **Chapter 6** on the other hand focuses on the parallel efforts to increase imaging speed by optimising the interferometer readout scheme as well using optical multiplexing to parallelise the readout from the sensor. Finally, **Chapter 7** provides an outlook on other possible improvements for mouse brain imaging, namely tackling skull induced acoustic aberrations and the proper choice of genetically encoded calcium indicators. The overall achievements and progress of this thesis are summarised in **Chapter 8**. Additionally, more lateral directions of work that were beyond the main aims of this thesis and concerned with extensions of the theory developed in **Chapter 5** into the field of fundamental optics as well as ideas on alternative ultra-fast all-optical photoacoustic sensing schemes are presented in **Appendix A** and **Appendix B**, respectively.

Chapter 2

Introduction to photoacoustic imaging

2.1 Photoacoustic effect

The photoacoustic effect is a phenomenon that arises when electromagnetic radiation interacts with a medium (water, tissue, etc.). There is a variety of mechanisms by which acoustic waves can arise in the photoacoustic effect, out of which the most important one for imaging applications is the thermal effect (Gusev and Karabutov, 1991). Under the thermal effect mechanism the signal level (so called initial pressure distribution) p_0 can be described as follows (Lin et al., 2015):

$$p_0 = \Gamma \eta_{th} I \mu_a \quad (2.1)$$

where, η_{th} is the percentage of the specific optical absorption that is converted into heat, I is the local light intensity (optical fluence), μ_a is the optical absorption coefficient and Γ is the Grüneisen coefficient, which describes the efficiency at which the samples converts heat into sound waves. **Equation 2.1** shows great similarity to the expression describing the signal level in fluorescence microscopy:

$$F_0 = \phi_{th} I \mu_a \quad (2.2)$$

where ϕ_{th} (quantum efficiency) is the percentage of the specific optical absorption that is converted into fluorescent emission.

2.2 Photoacoustic imaging

In a photoacoustic imaging application we are interested in reconstructing the spatial distribution of the concentration of the molecules of interest ($c_M(x, y, z)$). In a simple case of only one species of absorbers present in the sample:

$$c_M(x, y, z) = \frac{\mu_a(x, y, z)}{\epsilon_m} \quad (2.3)$$

The distribution of optical absorption $\mu_a(x, y, z)$ can be straightforwardly calculated from the initial pressure distribution reconstructed from a PA experiment under the assumption that the other terms in **Equation 2.1** (Γ , η_{th} and F) are either spatially invariant or their distribution is known. While this assumption holds true in most cases for Γ and η_{th} , in deep tissue imaging estimating $I(x, y, z)$ poses a considerable challenge for quantitative PAI and thus in reality:

$$\mu_a(x, y, z) \sim \frac{p_0(x, y, z)}{I(x, y, z)} \quad (2.4)$$

It is important to note that for qualitative purposes the assumption of $I(x, y, z) = \text{const}$ or $I(x, y, z) = I_0 \exp -\frac{z}{l_a}$ (where z is the depth and l_a is the absorption length characteristic for the tissue type and excitation wavelength) is often sufficient which simplifies data analysis.

As mentioned before, photoacoustic contrast has several similarities to fluorescence. The main similarities and differences of both modalities are collected in **Table 2.1**.

Fluorescence	Photoacoustics
$F_0 \sim I\mu_a$	$p_0 \sim I\mu_a$
optical absorption contrast	optical absorption contrast
photon emission	phonon (sound) emission
only amplitude information	amplitude and phase information
single-molecule sensitivity	multiple-molecule sensitivity
speed of light	speed of sound
ns fluorescence lifetime	ps photoacoustic lifetime

TABLE 2.1: Similarities and differences between fluorescence imaging and photoacoustic imaging

The major similarity lies in the fact that the source of contrast is virtually the same (excluding minor differences between the effective excitation dipole of fluorescence versus photoacoustics, Fuenzalida Werner et al., 2020). This is a big advantage of PA imaging over other deep-imaging methods for life sciences as it is a natural extension of widely used fluorescence imaging to the deep tissue regime.

The differences boil down to the emitted signal properties (light vs sound) and these determine the key advantages and disadvantages of photoacoustic imaging. The key disadvantage common for all photoacoustic imaging modalities is lower sensitivity compared to light microscopy. This limitation is a combination of two main factors: **(1)** phonons (which can be defined as quasiparticles carrying sound information, analogous to photons in case of light) are absorbed in the tissue much stronger than photons (light); **(2)** detecting single phonons is an extremely challenging task. In contrast, single photon detectors are routinely used and widely available. These two factors combined limit the sensitivity of PA as compared with fluorescent imaging.

Nevertheless, there are several fundamental advantages of photoacoustic signals. Firstly, because the PA lifetime is almost 3 orders of magnitude shorter than the FL lifetime, the excited state of the molecule does not live sufficiently long to undergo chemical reactions which contribute to photobleaching. Therefore, chromophoric molecules used in photoacoustics are much more resistant to photobleaching than their fluorescent counterparts (Gao et al., 2013). Secondly, the detection of sound enables recording of not only amplitude information but also phase. This enables very powerful computational image reconstruction methods employed in photoacoustic tomography which will be discussed in following sections. Finally, as the scattering coefficient of phonons is several orders of magnitude lower than for photons, sound can travel great depths (measured in centimeters) without being strongly perturbed enabling deep imaging (Ntziachristos, 2010).

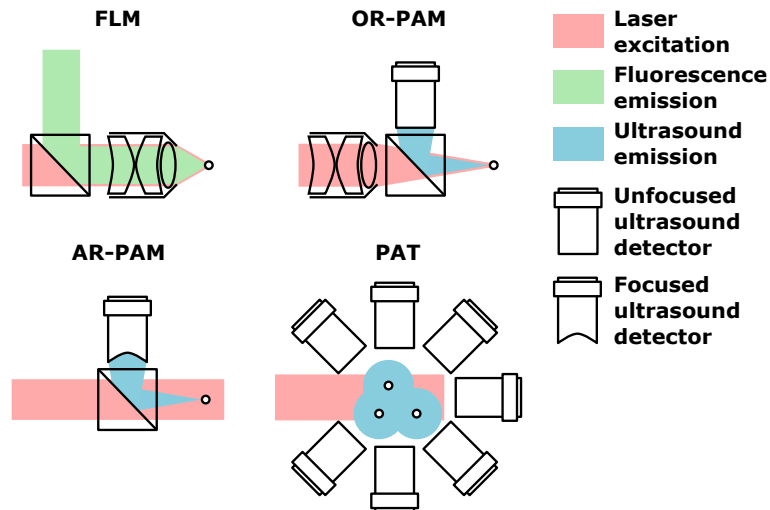


FIGURE 2.1: Scheme comparing different photoacoustic imaging modalities to fluorescent microscopy

2.3 Types of photoacoustic imaging techniques

Similarly to fluorescent imaging, photoacoustic imaging can also be divided into several distinct techniques which vary in their specifications and hardware implementations. The major division is between photoacoustic microscopy (PAM, which has a large similarity to confocal fluorescence microscopy) and photoacoustic tomography (PAT, which utilises the fact that PA signals contain both amplitude as well as phase information and in this regard shows some similarities to optical holography). Secondly, PAM can be further subdivided into optically-resolved PAM (OR-PAM) and acoustically-resolved PAM (AR-PAM) which differ in using the excitation PSF or the detection PSF respectively. **Figure 2.1** conceptualises the various excitation-detection schemes present in both basic fluorescent light microscopy (FLM) as well as in all the photoacoustic imaging modalities

	FLM	OR-PAM	AR-PAM	PAT
excitation	focused	focused	unfocused	unfocused
detection	focused	unfocused	focused	unfocused
resolution	optical	optical	acoustic	acoustic
penetration	optical	optical	acoustic	acoustic
mode	direct	direct	direct	indirect
imaging	all	point scanning	point scanning	volumetric

TABLE 2.2: Comparison of main types of photoacoustic imaging

2.3.1 Photoacoustic microscopy

Photoacoustic microscopy (PAM) is a direct imaging approach that is most similar to fluorescence microscopy, with the difference being that the contrast is switched from fluorescence to PA. Two main sub-fields of photoacoustic microscopy can be distinguished: OR-PAM and AR-PAM.

Optically-resolved photoacoustic microscopy (OR-PAM)

This modality is most closely related to fluorescence microscopy because the effective resolution of the technique is characterised by the optical focus which can be in the ~ 200 nm regime. Additionally, super-resolution techniques based on localisation microscopy (Kim et al., 2019) can be applied also in OR-PAM to further increase the resolution. Unfortunately, OR-PAM inherits not only the high spatial resolution of optical microscopy, but also the inherent penetration limit due to optical scattering. Because of this, it has limited use as a deep-tissue imaging modality and is not of particular interest for the purpose of this thesis.

Acoustically-resolved photoacoustic microscopy (AR-PAM)

In contrast to OR-PAM, in AR-PAM the effective resolution is characterised by the acoustic PSF of the detection (usually a focused ultrasound transducer). This solution sacrifices spatial resolution (which is now determined by the acoustic PSF of the transducer) in order to increase penetration depth. As the resolution comes from the detected sound waves the practical limitations in highest achievable resolution differ slightly from those present in optical microscopy (for detailed explanation see Tian et al., 2021). Here, it suffices to say that the achievable resolution deteriorates with depth, however, not due to scattering, but attenuation of high-frequency sound waves in the tissue. High-resolution AR-PAM ($\approx 1 \mu\text{m}$) is technically achievable, although only at very shallow depths due to strong attenuation of the used high-frequency acoustic waves (1 GHz). More commonly, AR-PAM is used for mesoscale imaging at the depth of several millimeters and achieves $\approx 200 \mu\text{m}$ spatial resolution. As such, it is potentially interesting for deep tissue imaging. However, due to several factors, we believe it is outperformed in our particular application by another photoacoustic imaging modality, namely Photoacoustic Tomography.

2.3.2 Photoacoustic tomography

Contrary to PAM, Photoacoustic Tomography (PAT) is an indirect imaging approach, meaning that the recorded raw data does not constitute an intelligible image but need to be computationally reconstructed first. This is both a strength and a weakness, as an additional step is required to form the images which poses an added challenge and might lead to generation of imaging artifacts. Fortunately, with constant development of image reconstruction methods for PAT (Treeby et al., 2011) and a good understanding of the image formation process, these risks are minimised. However, in the case of samples with highly heterogeneous mechanical properties (e.g. bone, such as present when imaging through the skull) AR-PAM still outperforms PAT in terms of the spatial resolution, because it is more resistant to skull induced acoustic aberrations.

The advantages of PAT come from the fact that both ultrasound speed ($\sim 10^3$ m/s) and ultrasound frequency ($< 10^9$ Hz) are low enough so that complete wave information (both amplitude and phase) can be captured with routinely used electronics. This complete information, in turn, allows for computational image reconstruction analogous to that used in optical holography. This gives immense possibilities for PAT as signals from the whole imaged volume can be acquired at the same time and then reconstructed in post-processing providing very powerful large volume imaging capabilities. Unfortunately, as with AR-PAM the achievable resolution is fundamentally limited by the acoustic frequencies present in the PA signals, which

for deep tissue applications practically restricts the technique to 50-100 μm in practice (Jathoul et al., 2015; Tian et al., 2021).

2.4 Sound wave detection in photoacoustic imaging

The performance of a photoacoustic imaging system heavily relies on the type of acoustic detector employed. The performance of the detector determines key imaging parameters of the setup and because of that, much emphasis is put on developing new detectors. Most current systems use classical ultrasound detectors adapted from ultrasound imaging (discussed in Section 2.4.1), these detector however are not optimal for photoacoustic tomography. Because of that a number of alternative detector designs were developed which will be discussed in Section 2.4.2.

2.4.1 Ultrasound transducers

Ultrasound transducers are widely used ultrasound detectors based on piezoelectric crystals. Piezoelectric crystals generate electric potential differences when undergoing mechanical deformations. Because of this they can be used as pressure sensors if combined with appropriate voltage amplifiers and data acquisition units.

Piezoelectric transducers are extensively exploited in photoacoustic imaging (Manwar, Kratkiewicz, and Avanaki, 2020). However, they have several disadvantages including complex light delivery, electronic cross-talk and the need for elaborate and unpleasant animal handling (Xia and Wang, 2013). Because of these there is a growing interest in developing alternative ultrasound detectors based on light (Dong, Sun, and Zhang, 2016; Wissmeyer et al., 2018) which will also be employed in this thesis.

2.4.2 Optical detection of ultrasound

There are several optical techniques for detection of acoustic waves, most of which use a particular type of the interferometry approach (Dong, Sun, and Zhang, 2016; Wissmeyer et al., 2018). Out of these, the technique which proved to be most successful in providing high-resolution photoacoustic images is the approach based on the use of Fabry-Pérot interferometers (FPIs) (Beard, Perennes, and Mills, 1999; Zhang, Laufer, and Beard, 2008). A Fabry-Pérot interferometer (FPI) is an optical device formed by two mirrors placed parallel to each other. This geometry forms an optical cavity that has very interesting properties when illuminated with highly coherent laser light (Vaughan, 2017). FPI of various constructions are widely used in the field of optics, from gravitational wave detectors to laser cavities themselves. In the following Section we will discuss their very particular use as ultrasound pressure sensors.

2.5 Sound wave detection using Fabry-Pérot interferometers

The principle of sound wave detection using FPI based systems has been extensively discussed elsewhere (Beard, Perennes, and Mills, 1999). Here, I will just limit myself to a very rudimentary introduction into the subject. To understand the concept of FPI sound detection it is key to introduce the concept of the interferometer transfer function (ITF).

2.5.1 Interferometer Transfer Function

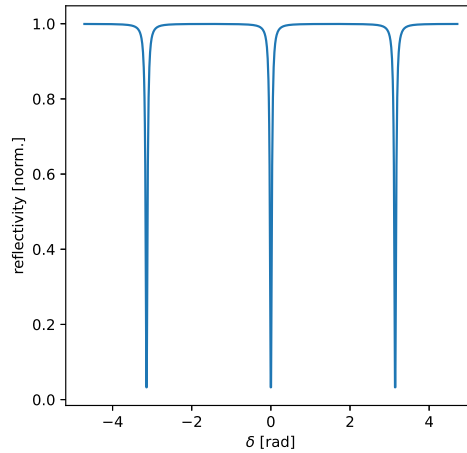


FIGURE 2.2: The reflection interferometer transfer function modeling the behaviour of an ideal FPI

The ITF describes the behaviour of an ideal FPI when illuminated with coherent light. Specifically, it describes how much light will be transmitted (or by inversion reflected) from the surface of the FPI depending on the wavelength of the light (λ), thickness of the cavity (l), angle of incidence of the light (θ) and other cavity parameters. The functional form of the ITF for an ideal FPI is as follows:

$$T(\delta) = \frac{1}{1 + F \sin^2(\frac{\delta}{2})} \quad (2.5)$$

where,

$$F = \frac{4R}{(1 - R)^2} \quad (2.6)$$

is the coefficient of finesse, R denotes the mirror reflectivity and

$$\delta = 2nlk \cos \theta \quad (2.7)$$

is the interferometer phase, where n is the refractive index of the material inside the cavity and $k = 2\pi/\lambda$ is the wavenumber. As for PA imaging the FPI is used in a reflecting configuration, the reflection ITF is more important practically (**Figure 2.2**):

$$R(\delta) = 1 - \frac{1}{1 + F \sin^2(\frac{\delta}{2})} = \frac{F \sin^2(\frac{\delta}{2})}{1 + F \sin^2(\frac{\delta}{2})} \quad (2.8)$$

Most importantly for our application, we see that the transmission of the FPI depends on the cavity thickness l and thus, the FPI can sense the physical deformation of the cavity caused, i.e. by an acoustic wave. This can be seen by looking on the change of reflectivity in response to a change of thickness of the cavity (**Figure 2.3**).

The coefficient of finesse and the sensitivity of the FPI

The coefficient of finesse F is a key parameter determining the quality of the FPI and consequently, its sensitivity to acoustic waves. For an ideal FPI the finesse is

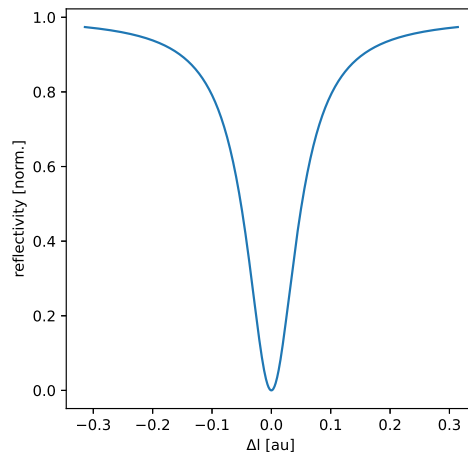


FIGURE 2.3: **Dependence of the reflectivity on the change in cavity thickness for a fixed laser wavelength**

determined only by the reflectivity of the interferometer mirrors as in **Equation 2.6**. The effect of increasing finesse (corresponding to increasing mirror reflectivity) is the narrowing of the linewidth of the spectrum (**Figure 2.4**). As the sensitivity of the FPI to acoustic waves is directly proportional to the slope of the ITF (Beard, Perennes, and Mills, 1999; Zhang, Laufer, and Beard, 2008) the maximal sensitivity of the FPI depends on the maximum of the derivative of the ITF (**Figure 2.5**).

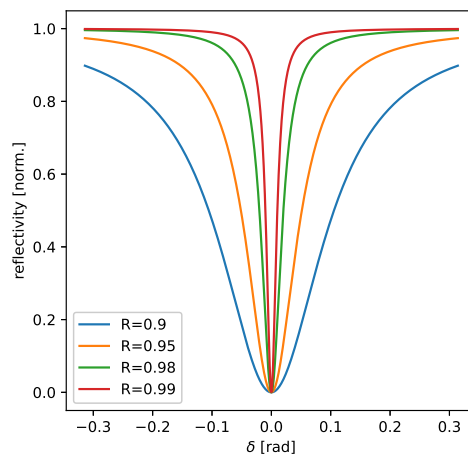


FIGURE 2.4: **Dependence of the shape of ITF on the interferometer finesse**

As there is a very steep increase of sensitivity with increasing mirror reflectivity it is beneficial to use FPIs with high finesse. However, in realistic FPIs the effective finesse is dependent on a number of additional factors, such as cavity imperfections (Varu, 2014) and mirror surface distortions (Czuchnowski and Prevedel, 2020). Some of these effects and possible ways of tackling loss of effective finesse will be further discussed in **Chapter 5**. Additionally as the FPI in PA imaging are interrogated with focused light the beam diameter increases as the beam propagates inside

the cavity slowly deteriorating the interference pattern for higher numbered reflections. Because the coefficient of finesse (F) can be interpreted as the effective number of round-trips inside the cavity the beam divergence effectively limits the achievable finesse. This can be tackled experimentally by changing the FPI geometry from planar to curved (e.g. by using an array of dome shaped micro-mirrors, Guggenheim et al., 2017).

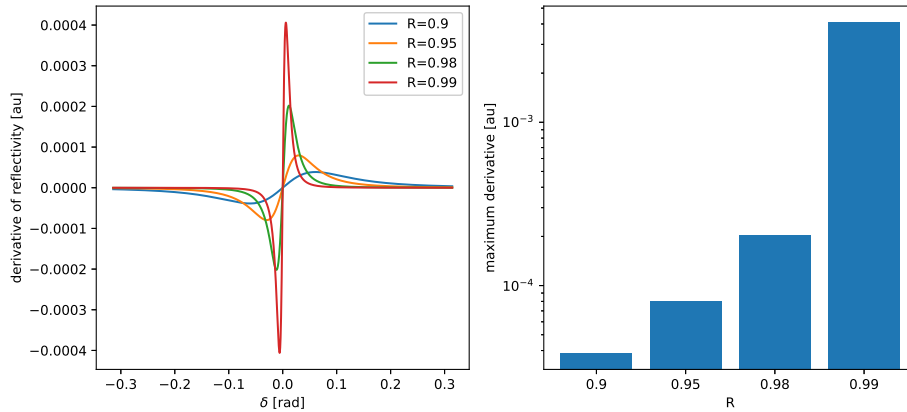


FIGURE 2.5: Dependence of the shape of ITF derivative on the interferometer finesse

2.6 Image reconstruction in Photoacoustic Tomography

As mentioned in **Section 2.3.2** PAT is an indirect imaging method and therefore the raw collected data needs to be reconstructed computationally to yield intelligible images. Several image reconstruction methods for PAT were developed including variations of the classical delay-and-sum, back-projection and more recently time-reversal. Additionally, with recent developments in deep learning several approaches using various sorts of neural networks were also employed for PA image reconstruction (see Yang et al., 2021 for review). Discussing all of the above mentioned methods is beyond the scope of this thesis and therefore, I will limit myself to only briefly introducing the most important method used for image reconstruction in the FPI-PAT systems.

2.6.1 Image reconstruction in FPI-PAT

The exact approach for reconstructing PAT images depends heavily on the detector geometry employed, and thus, distinct methods were developed for linear, spherical and planar detectors. In case of the FPI system, the most extensively used method is called time-reversal and is based on solving the acoustic wave differential equation backward in time (hence the name time-reversal) using the acquired detector data as a boundary condition (Treeby, Zhang, and Cox, 2010).

Chapter 3

Photoacoustic tomography system design

3.1 Fabry-Pérot interferometer fabrication

The Fabry-Pérot interferometer (FPI) is the key detector element of the system around which all of the optics and electronics are built. Great care needs to be put into choosing the right parameters for fabrication of this device. The details of FPI manufacturing for PA sensing as well as the effects of various parameters on its performance were already discussed extensively elsewhere (Beard, Perennes, and Mills, 1999; Varu, 2014).

Here, I will just briefly motivate the choice that was made for preparing the sensors used in this thesis. There are three key parameters that needed to be considered: **(1)** the thickness of the Parylene C layer used as the elastic spacer, **(2)** reflectiveness of the two mirrors, **(3)** the material from which the mirrors are made (**Figure 1.1**).

In case of **(1)** it was shown that there is an inverse relation between between the FPI sensitivity and the FPI acoustic bandwidth determined by the cavity thickness (Beard, Perennes, and Mills, 1999; Zhang, Laufer, and Beard, 2008). A thicker cavity leads to higher sensitivity at the expense of lowering the bandwidth, which ultimately limits the spatial resolution of the reconstructed images. As we were aiming at high-resolution mesoscopic imaging for life science applications we chose a relatively thin cavity (between 20-30 μm) that was shown to enable high-quality imaging in mice (Jathoul et al., 2015).

As for **(2)**, from theoretical considerations in **Section 2.5** we could conclude that higher mirror reflectivity leads to better sensitivity and as such, we should aim at highest possible reflectivities. However, as discussed before, in practice cavity imperfections strongly limit the achievable sensitivity. It was previously described that the optimal reflectivity is placed in range 95-98% (Varu, 2014). For practical reasons we chose the value 98% as the company, we were collaborating with, had previous experience in coating such layers.

Finally, the choice of mirror material was relatively limited due to the lack of a variety in the reported FPI pressure sensor designs **(3)**. Two main approaches were described: the use of soft-dielectric materials (Zhang, Laufer, and Beard, 2008) and more recently the use of hard-dielectric materials (Buchmann et al., 2017). Soft-dielectrics present the strong advantage of being highly deformable and thus, acoustically invisible for the PA waves. This allows for recording of unperturbed high quality signals that are key for high-resolution PA imaging. Their downside comes from the fact that soft-dielectrics are highly hygroscopic and capable of absorbing water even from air. Importantly, absorbing large amounts of water may lead to mirror cracking resulting in the destruction of the FPI. As water or water based gels are commonly used for acoustic coupling in PA imaging the use of soft-dielectrics

strongly limits the lifetime of FPIs employed in PAT. In contrast, hard-dielectrics are water resistant and have much longer lifetimes. The downside is their high stiffness which deforms the PA signals recorded by hard-dielectric FPIs (Buchmann et al., 2017). Because of the high quality of signal we decided to use soft-dielectric FPIs which were coated with an additional layer of Parylene C to protect them from environmental humidity (Zhang, Laufer, and Beard, 2008). This approach lengthens the lifespan of the interferometers allowing for multiple subsequent experiments before the FPI needs to be exchanged.

3.1.1 Cavity inhomogeneities

Cavity inhomogeneities can lead to multiple detrimental effects for PAT and need to be addressed in an experimental PAT system. On a local level cavity inhomogeneities can lead to deformations of the ITF and degrade the optical sensitivity of the FPI (**Figure 3.1, left**). This can be either due to a wedged cavity (Varu, 2014) or due to optical aberrations induced by the irregular cavity shape (**Chapter 5**, Czuchnowski and Prevedel, 2020). **Chapter 5** discusses possible ways of tackling this problem with the use of Adaptive Optics in more detail.

On a more global level, long range changes in cavity thickness generate shifts of the optimal wavelength (λ_{opt}) needed to interrogate the FPI (**Figure 3.1, right**) and forces the use of tunable lasers for FPI interrogation in PAT. The choice of the laser will be further discussed in **Section 3.4** after the description of the interrogation light path in **Section 3.2**.

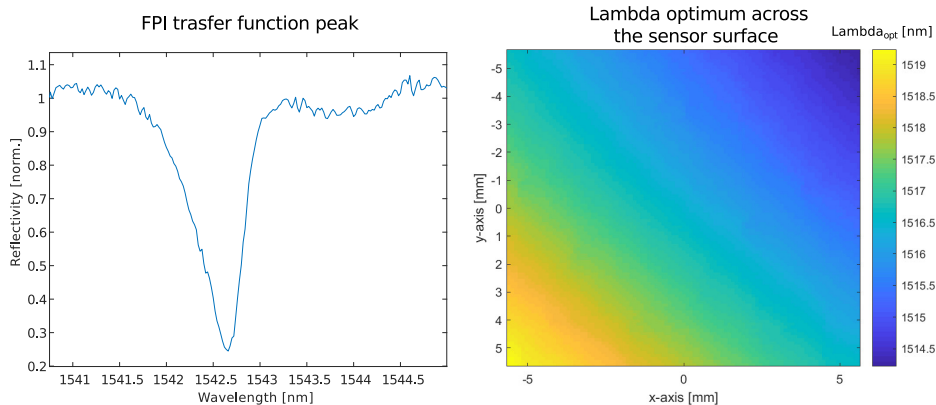


FIGURE 3.1: **Optical quality measurements of the FPI (left)** The transfer function shows a dip in reflectivity reaching almost 0.2 which shows high quality in terms of local surface roughness. **(right)** Lambda optimum is a parameter describing the optimal interrogation wavelength at each point on the FPI, the measured variability on the whole surface is comparable to published data on similar sensors.

3.2 Interrogation light path

As the ultimate goal of the project was to develop PAT into a functional neuroimaging modality, the system was designed with this goal in mind. As the final implementation was supposed to incorporate multiple scanning beams arranged in a line and relayed from the surface of the FPI onto the photo-diode array (PDA), the system required a robust optical design that would introduce minimal optical aberrations even for the edge beams.

3.2.1 Multi-beam PAT system (M-PAT)

The initial idea was to use a linearly aligned fibre array at the input of the optical system (**Figure 3.2**) which would significantly simplify the issue of generating multiple beams. This, however, requires the system to operate in an imaging mode where the fibre array plane the FPI-plane and the PDA-plane are conjugated by 4f-relays to provide best performance. This is realised practically by a set of lens relays, first, R1-R2 together with GL(Galvo Lens)-Scan Lens relay the output of the fibre array onto the surface of the FPI and enable the optical readout of acoustic waves from the FPI. Next, the light back-reflected from the FPI is relayed onto the PDA by the GL-Scan Lens together with R2-R3 by using a polarising beam-splitter (PBS) coupled with a quarter-waveplate ($\lambda/4$).

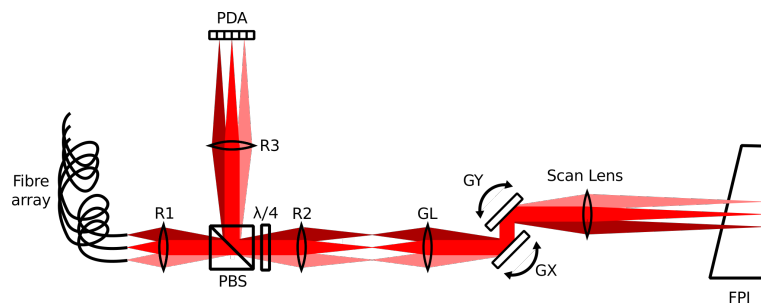


FIGURE 3.2: Design of the multi-beam PAT system

The overall design of the system seems straightforward, however, the challenges come from the physical size of the fibre array to be used (the minimal achievable spacing between the fibres is $125 \mu\text{m}$ which would translate to 5.625 mm for the whole 46-fibre array). At this size the edge beams are already considerably off-center from the optical axis where realistic lenses no longer work optimally and introduce strong aberrations. Because of this, large effort was put into simulating the performance of system dependent on the choice of particular lenses using the Zemax software (**Figure 3.3a**).

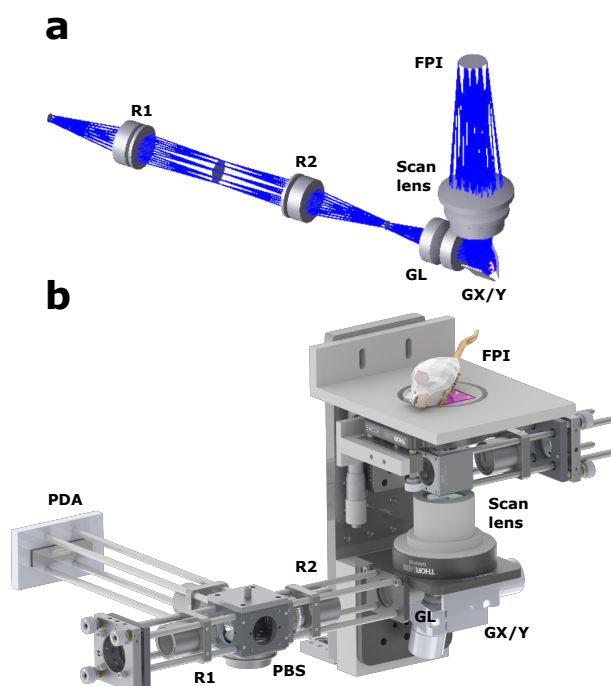


FIGURE 3.3: Optical and optomechanical design of the M-PAT system
 a) Optical design of the M-PAT system using Zemax
 b) Optomechanical design of the M-PAT system using Solidworks.

In the end two particular solutions were employed: **(1)** Lenses R1-R3 were substituted from singlet lenses to compound lenses being a combination of an achromatic doublet and a positive meniscus lens (this solution was inspired by a similar design employed in scanning microscopy to increase beam stability and minimise optical aberrations); **(2)** GL was substituted by a PLOSSL (a combination of two achromatic doublets) that allows for a short focal length while also minimising aberrations.

Next, the employed solutions were tested experimentally by measuring the point spread function (PSF) of the built system and comparing it with the design value from Zemax simulations (**Figure 3.4**). To perform this test, a single fibre was mounted on a translational stage that allowed the measurement of the effect of the vertical displacement from the optical axis on the PSF (which simulates the difference between a center and edge beam for a fibre array). In general, the experimental results match closely the designed PSFs with a small degradation of quality arising from manufacturing imperfections of the lenses that could not be captured by Zemax.

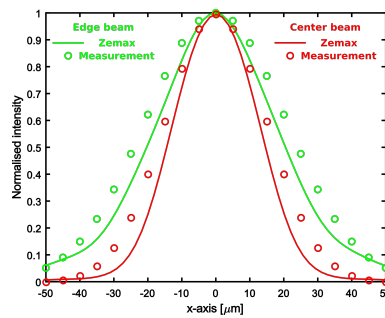


FIGURE 3.4: Comparison of design performance with experimentally measured PSF

Further, the PSF dependence on the scan position on the FPI surface was assessed by placing a camera in the FPI plane and experimentally measuring the PSF at various scan positions (**Figure 3.5a**). By fitting a Gaussian curve to the x- and y-crosssections we observe that the PSFs are rotationally symmetric with no large aberrations noticeable in the lateral dimensions.

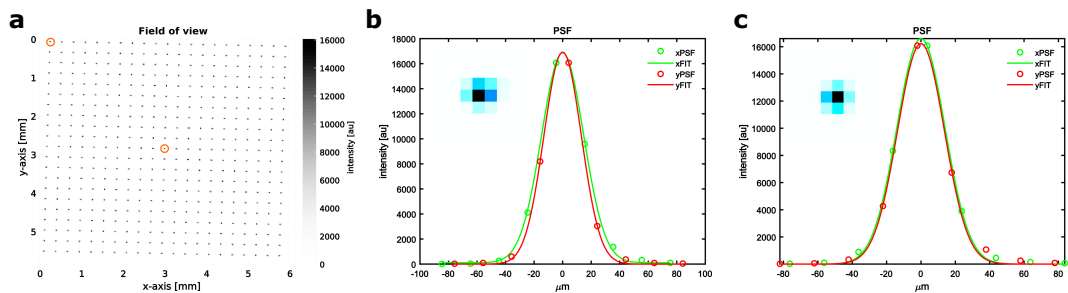


FIGURE 3.5: Validation of system resolution across the scan grid **a)** Image of the scan grid taken with an InGaS camera showing uniform spacing of points with no visible field of view aberrations. **(b,c)** Estimation of the PSF for the center **(b)** and edge **(c)** scan positions showing no significant deterioration of the FWHM.

3.2.2 Single-beam PAT system (S-PAT)

The M-PAT system is also capable of supporting single beam imaging (S-PAT) in a straightforward manner, where the fibre array and PDA are substituted with a single fibre and a single channel photodiode (**Figure 3.6**). As the S-PAT system is much

easier to implement, most of the validation work described in **Chapter 4** was done using the S-PAT, however, extensions toward M-PAT are also extensively discussed.

One additional feature of our design is that using an imaging setup employing 4f-relays instead of infinity-optics allows the use of non-Gaussian beams. This fact is capitalised with the use of Adaptive Optics in our system which allows for enhanced detection sensitivity (as described in **Chapter 5**).

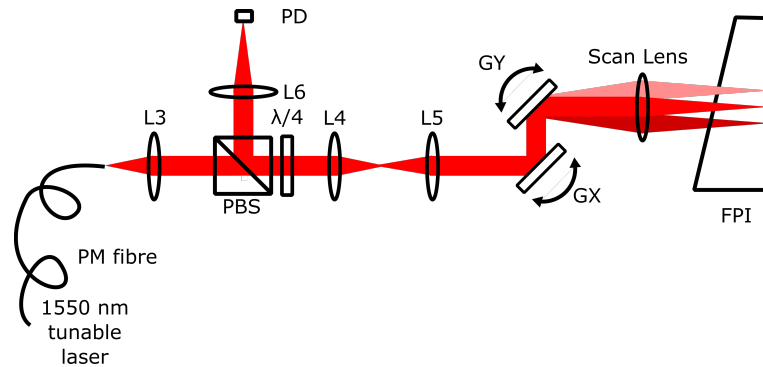


FIGURE 3.6: Optical design of the S-PAT system

3.2.3 Upright PAT (uPAT) versus inverted PAT (iPAT)

The last point important to discuss considering the design of our PAT system light path is the choice of imaging geometry. Due to the use of the FPI our system can be designed in two distinct geometries reminiscent of the situation in classical light microscopy: **(1)** upright (where the FPI is placed above the sample) or **(2)** inverted (where the FPI is placed below the sample). Similarly to the light microscopy, the choice of the particular geometry depends heavily on the choice of sample. As in the first stages of the development of the system we were mainly interested in imaging the abdominal area of mice, the system was developed with a inverted geometry to simplify animal handling and its placement on the FPI. The majority of the thesis will therefore be concerned with the iPAT geometry.

However, it is important to note that iPAT is not optimal for some particular applications such as brain imaging where the animal would need to be placed upside down. For these applications we have developed an alternative uPAT system which will be described in detail in **Chapter 7**.

3.3 Excitation laser

Before discussing the requirements for the interrogation laser it is important to consider the excitation laser first, as key features of the interrogation laser are determined by choice of excitation. As mentioned in **Section 2.1** the dominant mechanism of evoking the photoacoustic effect for PAI is the use of the thermal effect. The thermal effect requires a rapid heating process which in turn requires modulation of the excitation light over time. This can be practically realised in two ways: **(1)** a modulated CW laser can be used where the sample is probed one acoustic frequency at a time (Lashkari and Mandelis, 2010); **(2)** a pulsed laser source can be used which generates broadband PA emission (Zhang, Laufer, and Beard, 2008). Pulsed laser sources are used much more often as they allow for faster imaging (the whole frequency spectrum of the source can be recorded in a single excitation), and because of that we also employed a pulsed laser source in this thesis.

Further, there are two main subcategories of pulsed sources: **(2.1)** high-power low-repetition-rate Nd:YAG lasers; **(2.2)** high-repetition-rate low-power laser diodes. Both solutions have advantages and disadvantages. **(2.1)** are used more often in scientific systems as they offer high signal-to-noise ratio (SNR) and versatility (they can be tuned to various wavelengths by combining them with, so-called, optical parametric oscillators or OPOs). Their downside is a very low pulse repetition rate (PRR, typically < 100 Hz) and high price. On the other hand **(2.2)** are very often used in clinical systems due to their low cost and ease of implementation on commercially available medical ultrasound detectors. Their main downside lies in low power (and consequently low SNR) which needs to be mitigated via averaging over multiple excitations. Fortunately the PRR of laser diodes is orders of magnitude faster than **(2.1)**. As our system requires both high SNR and versatility to be used in life science applications we chose solution **(2.1)**.

As discussed in **Section 2.6** a high quality PA image with a FOV on the order of $1\text{ cm} \times 1\text{ cm}$ requires 10^4 PA waveforms. Consequently, this requires 10^4 excitation pulses (for S-PAT) as only a single waveform can be acquired during each excitation. This means that for a fixed number of detection channels the temporal resolution of PAT is limited by the PRR of the excitation laser.

FOV	# of waveforms	# of detectors	PRR	volumetric rate
1 cm x 1 cm	10^4	1	50 Hz	0.005 vps
1 cm x 1 cm	10^4	1	100 Hz	0.01 vps
1 cm x 1 cm	10^4	50	100 Hz	0.5 vps
1 cm x 1 cm	10^4	50	200 Hz	1 vps

TABLE 3.1: Dependence of the volumetric imaging rate on the excitation laser PRR

Table 3.1 shows the relation between the PRR of the laser and the achievable volume rate in vps (volumes per second). It can be seen that for a typical value of the PRR (50 Hz) for a PAT excitation laser one can expect at most one volume per ≈ 3.3 min, which is sufficient for the purposes of imaging static structures but much too slow to capture dynamical processes (i.e. brain activity). For purposes of neuroimaging even upscaling the number of detectors to a substantial number of 50 (which the current size limit on commercially available PDAs) will not yield the required 1 vps imaging rate. This motivated us to choose the fastest excitation laser available at the time (SpitLight DPSS EVO I OPO 200 Hz, InnoLas Laser GmbH), boasting a 200 Hz PRR which would fundamentally enable us to perform neuroimaging experiments provided the upscaling of detector beams to 50.

3.4 Interrogation laser

As mentioned in **Section 3.1.1** cavity inhomogeneities require the use of tunable lasers for efficient interrogation of the FPI (Zhang, Laufer, and Beard, 2008). This creates a strong limitation on the wavelengths that can be used as the required tunable lasers were developed extensively only in selected spectral bands. The most useful is the, so-called, C-band (1530-1565 nm) used extensively in telecommunications where several high performance lasers were developed. This motivates the design of FPIs around this spectral window despite the fact that the sensitivity of a FPIs drops with increasing interrogation wavelength.

There are two key parameters that govern the choice of the interrogation laser: power and tuning speed. High power enables high SNR measurements of the PA waves and directly translates to high sensitivity of the PAT system. Tuning speed is a

more subtle aspect as it works in tandem with the PRR of the excitation to determine the effective imaging rate. As often there is a need to change the interrogation wavelength almost between each pair of scan positions, it is crucial that this tuning step takes less time than the delay between two excitation pulses. This poses less of a problem for 50 Hz excitation lasers where this time window equals 20 ms, but starts to become challenging for 200 Hz lasers where it shrinks to 5 ms (possible strategies to tackle the tuning speed problem are presented in **Chapter 6**). For these reasons we choose the NewFocus, VenturiTM TLB-8800-H-CL tunable laser as it boasts both high power (10 mW) as well as fast tuning capabilities.

3.5 Photodetectors and data acquisition

The use of 1550 nm interrogation light determines the type of photodiodes employed in the system (InGaS). In case of S-PAT a commercially available amplified photodetector is sufficient for our application (PDA05CF2, Thorlabs). However, alternative approaches using passive signal amplification can significantly reduce the detector noise (see **Chapter 5** for details). Data acquisition can either be performed by a digitising storage oscilloscope (DSO) or by commercially available high frequency DAQ cards which have the advantage of directly writing the data onto the hard drive of the workstation.

For the M-PAT application there exist no fully commercial solution. The multi-channel photodetector is composed out of a commercially available PDA (G12430-046D, Hamamatsu) coupled with a custom made multichannel pre-amplifier. The data acquisition is performed by a custom made multichannel FPGA (field programmable gate array) system, courtesy of the Max Plank Institute for nuclear physics (Heidelberg, Germany).

Chapter 4

Photoacoustic system validation

4.1 Characterisation of Fabry-Pérot Interferometers

As the key sensing element in our PA imaging system is the Fabry-Pérot interferometer, the validation requires a detailed understanding of the intricacies of FPI based pressure measurements. This section discusses the key concepts for optimal performance of FPI system. Firstly, **Sections 4.1.1 and 4.1.2** will define the concept of optical sensitivity of the FPI which was eluded to in **Section 2.5** as well as describe experimental method for measuring the value of sensitivity. Secondly, **Section 4.1.3** uses the introduced concept of optimal wavelength and puts it into the context of imperfect and spatially heterogeneous FPI cavities. Finally, **Section 4.1.4** will use the definition of optical sensitivity and describe a concept of crucial practical importance, namely, the optimal working point for a photodetector used in an FPI based PA measurement. The text of **Section 4.1.2**, **Section 4.1.4** and **Section 4.5.1** has been taken from Czuchnowski and Prevedel, 2021 and has been originally written by myself.

4.1.1 Sensitivity of FPI based PAT systems

The overall sensitivity of an FPI pressure sensor can be defined as follows (Beard, Perennes, and Mills, 1999; Zhang, Laufer, and Beard, 2008):

$$S = \frac{dI}{dp} \quad (4.1)$$

where I is the light intensity on the photodiode and p is the local pressure interacting with the cavity. This expression can be further expanded:

$$S = \frac{dI}{dp} = \frac{dI}{d\delta} \frac{d\delta}{dp} \quad (4.2)$$

where δ is the phase variable of the ITF (**Equation 2.5**) of the FPI defined in **Equation 2.7**. Consequently $\frac{dI}{d\delta}$ is dubbed the optical sensitivity of the FPI (S_o) and $\frac{d\delta}{dp}$ is the acoustic sensitivity of the FPI (S_a). The acoustic sensitivity (S_a) is not a topic of interest of this thesis due to several reasons: **(1)** it is discussed extensively elsewhere (Beard, Perennes, and Mills, 1999); **(2)** it depends mainly on the mechanical properties of the FPI which are not extensively studied or modified in this thesis. On the other hand the optical sensitivity (S_o) will be discussed in detail in the following sections as well as be the primary topic of **Chapter 5** as several approaches can be developed for improving S_o .

Additionally, it is important to note that the effective sensitivity of the measurement is dependent not only on S , but also on the noise present in the system (N) and generally expressed as the signal-to-noise ratio (SNR):

$$SNR = \frac{S}{N} \quad (4.3)$$

The noise present in the FPI system is a combination of several terms:

$$N = \sqrt{N_{shot}^2 + N_{RIN}^2 + N_{phase}^2 + N_{electronic}^2 + \dots} \quad (4.4)$$

The contribution of the individual terms was discussed in detail in Varu, 2014 and for the purpose of this thesis it suffices to say that in our system the dominant sources of noise are the shot noise (N_{shot}) as well as the electronic noise of the detector ($N_{electronic}$). Potential ways to tackle the effects of these noise sources on the effective SNR will also be described in **Chapter 5**.

4.1.2 Optical sensitivity

The sensitivity of the Fabry-Pérot Interferometer varies locally depending on a number of factors. Thus, it needs to be measured independently for each scan position on the FPI. Optical sensitivity for an FPI can be defined in multiple ways, in the context of this thesis the following definition will be used:

$$S_o(I_{FPI}(\lambda)) = \frac{\frac{d}{d\lambda} I_{FPI}(\lambda)|_{\lambda=\lambda_{opt}}}{I_{FPI}(\lambda_{opt})} \quad (4.5)$$

where:

$$\lambda_{opt} = \operatorname{argmax}\left\{\left|\frac{d}{d\lambda} I_{FPI}(\lambda)\right|\right\} \quad (4.6)$$

and $I_{FPI}(\lambda)$ is the transfer function of the interferometer. This definition is different from the general definition described in the previous section ($S_o = \frac{dI}{d\delta}$), but it has very similar properties and one main advantage, being, that it is easy to quantify and compare experimentally as it does not require the knowledge of the local cavity thickness which is difficult to acquire.

Quantification of sensitivity from experimental data

Even if we assume a definition of sensitivity, there still exist multiple ways of quantifying it based on experimental data. The key question is the choice of approach for calculating $\frac{d}{d\lambda} I_{FPI}(\lambda)$.

The simplest approach is to calculate $\frac{d}{d\lambda} I_{FPI}(\lambda)$ directly from the raw data.

$$S_o^{raw} = S_o(I_{FPI}^{raw}(\lambda)) \quad (4.7)$$

Unfortunately, S_o^{raw} suffers from high noise due to a use of a numerical derivative. An alternative approach is to calculate S_o after some pre-processing of the data (eg. smoothing, denoising):

$$S_o^{fit} = S_o(I_{FPI}^{fit}(\lambda)) \quad (4.8)$$

Multiple fitting approaches are described in the literature (Varu, 2014; Buchmann et al., 2017; Zhang, Laufer, and Beard, 2008). We chose the method based on fitting

of the Psuedo-Voigt function (Buchmann et al., 2017) as this allows for robust and real-time fitting of the FPI transfer function:

$$V_p(x) = \eta \cdot L(x, f_L) + (1 - \eta) \cdot G(x, f_G) \quad (4.9)$$

with $L(x, f_L)$ being the Lorentz function and f_L its FWHM parameter, $G(x, f_G)$ being a Gaussian function with f_G its FWHM parameter, and η is chosen according to Ida, Ando, and Toraya, 2000 as:

$$\eta = 1.36603(f_L/f) - 0.47719(f_L/f)^2 + 0.11116(f_L/f)^3, \quad (4.10)$$

where

$$f = [f_G^5 + 2.69269f_G^4f_L + 2.42843f_G^3f_L^2 + 4.47163f_G^2f_L^3 + 0.07842f_Gf_L^4 + f_L^5]^{1/5}. \quad (4.11)$$

4.1.3 Optimal wavelength

The concept of optimal wavelength (λ_{opt}) is crucial from the perspective of defining FPI sensitivity (S_o), but has also other important implications for FPI-based PA measurement. As discussed in **Section 2.5** the sensitivity of the actual PA measurement strictly depends on the use of the proper interrogation wavelength (λ_{opt}). λ_{opt} , in turn, depends on the local cavity thickness. As due to the manufacturing process FPI pressure sensors display inhomogenities in cavity thickness, λ_{opt} varies across the surface of the sensor (**Section 3.1.1**) which motivates the use of tunable interrogation lasers (see **Section 3.4**).

There are two limitations that follow from the variability of λ_{opt} across the FPI sensor: **(1)** The interrogation laser wavelength needs to be adjusted frequently, which generates dead time in the setup performance and limits the acquisition speed (and, hence, volume rate), which is crucial for visualising dynamic processes. This can be partially alleviated by the choice of a fast interrogation laser (see **Section 3.4**), but also requires additional efforts in optimising the data acquisition procedure (as discussed in **Section 6.1**); **(2)** A more fundamental limitation is connected to optical multiplexing. As the multiplexed beams are generated from a single tunable laser they have the same wavelength, which means optical multiplexing can only be employed if the FPI has high enough spatial homogeneity of cavity thickness to allow the interrogation of multiple spots on the FPI with the same wavelength (this will be discussed in greater detail in Section 6.2).

4.1.4 Optimal working point of the photodetector

The effective sensitivity at each point is linearly dependent on the incident power provided that the power level does not exceed the saturation limit of the detector ($P_{saturation}$). As this is crucial for optimal system performance, we develop a simple model to account for the changes in the photodiode working point. Due to spatial heterogeneity of the FPI cavity the intereferometer will display a distribution of normalised sensitivities (S_i) and a corresponding distribution of working points (p_i). By the distribution of working points we understand the fact that different points on the FPI will display different degrees of reflectivity at the bias wavelength leading to varying levels of DC power on the photodetector. The DC power level at each point can be defined as $P_i = Pp_i$ where P is the output power of the interrogation laser and p_i is the working point defined as the fraction of the laser power incident

onto the photodetector for a particular position on the FPI when tuned to the bias wavelength. Because of this the effective normalised sensitivity at each point will depend on the saturation of the photodetector:

$$S(P_i) = \begin{cases} 0 & \text{if } P_i \geq P_{saturation} \\ S_i & \text{if } P_i < P_{saturation} \end{cases} \quad (4.12)$$

Taking this into consideration we can write the expression for the effective signal-to-noise ratio (SNR) in the reconstructed image. To simplify the problem, we assume that each point on the surface of the FPI detects signals from the whole imaged volume and in the reconstruction process these signals are coherently summed, therefore, the sensitivity at each point of the reconstructed volume equals:

$$S \sim \sum_{i=1}^n S(P_i)P_i \quad (4.13)$$

Similarly, we assume that the system is shot noise limited and the noise at each point adds incoherently:

$$N \sim \sqrt{\sum_{i=1}^n P_i} \quad (4.14)$$

therefore, the expression for the effective SNR becomes:

$$SNR_{eff} = \frac{S}{N} \sim \frac{\sum_{i=1}^n S(P_i)P_i}{\sqrt{\sum_{i=1}^n P_i}} \quad (4.15)$$

The output power of the interrogation laser (P) is a free parameter which allows us to optimise the performance of the setup for a give p_i and S_i distribution which can be measured experimentally.

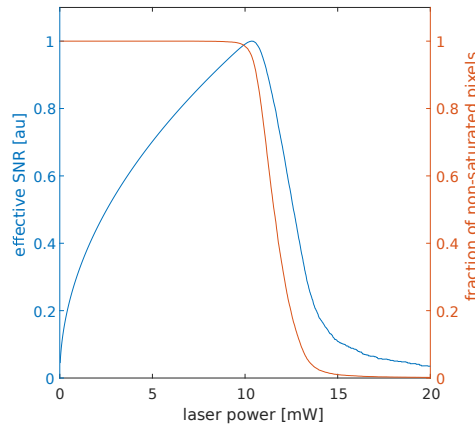


FIGURE 4.1: Optimal working point of the photodiode

Loss of effective SNR due to working point distribution

Effectively, the distribution of working points (P_i) limits the effective SNR of the system, because some of the points on the FPI do not operate in their optimal working regime. If this could be corrected (e.g. by adapting the laser power individually at

each scan position), then the system could perform at each scan position optimally effectively increasing the SNR:

$$S_{opt} \sim P_{opt} \sum_{i=1}^n S_i \quad (4.16)$$

and:

$$N_{opt} \sim \sqrt{\sum_{i=1}^n P_{opt}} = \sqrt{nP_{opt}} \quad (4.17)$$

thus:

$$SNR_{opt} \sim \frac{S_{opt}}{N_{opt}} = \frac{P_{opt} \sum_{i=1}^n S_i}{\sqrt{nP_{opt}}} = \sqrt{\frac{P_{opt}}{n}} \sum_{i=1}^n S_i \quad (4.18)$$

The difference between the optimal SNR (SNR_{opt}) and the effective SNR (SNR_{eff}) for an experimentally relevant FPI is on the order of 8% which does not constitute a large effect. However, if other detector configurations are used (such as fibre-coupled photodiodes) this effect can be significantly larger, which will be discussed in more detail in **Section 5.3**.

4.2 Effects of temperature on system performance

The FPI shows high sensitivity to cavity deformations which enables very sensitive photacoustic measurements, but at the same time may introduce complications to the measurement procedure. FP cavities are known to have mechanical drift due to vibrations of the mirrors, however, in our case thanks to the use of a solid cavity these are negligible. Unfortunately, due to the use of solid cavities there exists the possibility of thermal drift connected to the thermal expandibility of the medium filling the cavity (Parylene C). This has its advantages in some applications, as the FP cavity can be used for thermal sensing in addition to pressure sensing (Morris et al., 2009), but for pure PA imaging it is an issue that needs to be addressed.

4.2.1 Effects of cavity expansion on an ideal FPI

To gain an intuitive understanding of the effects of temperature on the FPI it is best to start by analysing the response of an ideal FPI to cavity expansion. We begin by analysing the effects on the position of the reflectivity minima (λ_{min}).

The position of the reflectivity minimum is defined from **Equation 2.5** by putting:

$$\sin\left(\frac{\delta}{2}\right) = 0 \quad (4.19)$$

which means that,

$$\left(\frac{2\pi}{\lambda_{min}}\right)nl \cos\theta = m\pi \quad (4.20)$$

because our systems works in back-reflection mode $\cos\theta = 1$ so the equation simplifies to:

$$\lambda_{min} = \frac{2nl}{m} \quad (4.21)$$

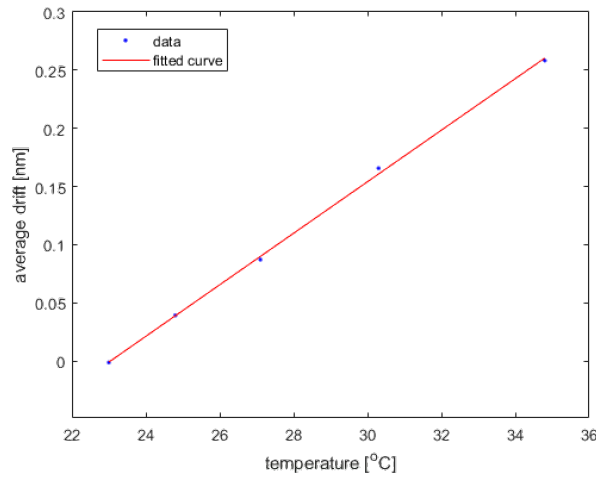


FIGURE 4.2: λ_{min} **dependence on temperature** The points represent averages across the FPI field-of-view (10^4 points).

This means that λ_{min} is linearly dependent on cavity length l ($\lambda_{min} \sim l$), and because thermal expansion in 1D also follows a linear law:

$$\frac{\Delta L}{L} = \alpha_L \Delta T \quad (4.22)$$

Therefore, we conclude that $\lambda_{min} \sim \Delta T$, which can be verified experimentally (Figure 4.2).

4.2.2 Consequences for PAT

As mentioned in previous sections, a FP-PAT system requires a characterisation of the FPI before a photoacoustic measurement can take place. However, as concluded in **Section 4.2.1** the characterisation itself depends on the temperature of the FPI (and consequently on the contact with the sample as well as the presence of excitation light which causes slight tissue heating (**Figure 4.3**). This problem can be solved in three ways: **(1)** one can ascertain that the characterisation is done at the same temperature as the measurement, **(2)** one can control the temperature of the FPI during the measurement to adjust it to the temperature of the characterisation, **(3)** one can re-characterise the FPI just before the measurement to adjust for the temperature difference.

Option **(1)** is unfeasible because both the presence of the sample and the excitation light will change the local temperature of the FPI. Option **(2)**, although feasible, is challenging on the hardware implementation side. Because of this, we chose option **(3)** which requires no additional hardware.

Fast re-characterisation

Due to the fast wavelength sweeping characteristics of the interrogation laser it is possible to acquire the ITF at ~ 12 scan positions within one second. This translates into ~ 14 min for characterisation of the whole FOV which is impractically long for the purpose of re-characterising the FPI before the measurement. To shorten this, I employed a sub-sampling approach where one point in a 3×3 patch is characterised and the shift in λ_{opt} is quantified, subsequently, this shift is applied to the whole 3×3 patch effectively reducing the time required for re-characterisation by 9-fold (~ 90

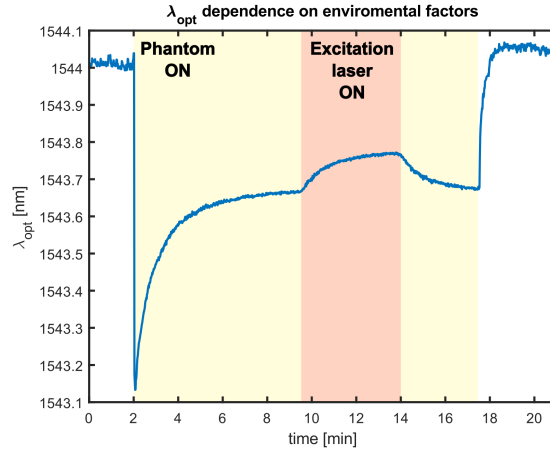


FIGURE 4.3: λ_{opt} dependence on sample presence and excitation light Phantom ON - time period when the sample (agarose phantom) is present on the FPI; Excitation laser ON - time period when the excitation light is on and illuminating the sample.

s). There is no need to further reduce this time as thermal equilibration happens on a timescale of a few minutes.

Characterising the ITF on the wavelength sweep of the laser is challenging as the sweep speed (measured in nm/s) is only approximately linear and may distort the shape of the ITF. To tackle this, the acquisition is synchronised to a calibrated trigger output of the laser that triggers after each 100 pm. The downside of this approach lies in the fact that the ITF is then acquired with a 100 pm resolution which is not sufficient to determine λ_{opt} directly from the raw data. This problem is alleviated by using the ITF fitting approach described in **Section 4.1.2**.

Validation of the re-characterisation scheme

Validation of the re-characterisation scheme is crucial to ascertain the optimal performance of the system during measurement. It is difficult to perform directly, but can be simplified with a clever design of the measurement. As mentioned previously, the FPI needs to be characterised prior to the measurement to determine the optimal wavelength (λ_{opt}) at each scan position, this characterisation simply means acquiring the shape of the ITF for each scan position and then calculating λ_{opt} using **Equation 4.6**. However, as mentioned in **Section 4.2.1** the value of λ_{opt} might change due to the thermal drift of the cavity and additionally the laser can also experience a drift of the output wavelength compared to the expected value.

A simple re-characterisation does not solve this problem as the system operates differently under characterisation and actual measurement conditions. In particular, during characterisation the whole ITF is acquired by sweeping the laser wavelength and during measurement the laser wavelength is stably positioned at a single value for each scan position. Because only a single wavelength is used during measurement determining whether the ITF or the laser wavelength drifted becomes challenging. **Figure 4.4a** describes the validation procedure in a schematic way. The ITF (blue line) is known for each point from the characterisation, from this the value of λ_{opt} can be inferred as well as the expected signal level (P_{opt}) when illuminating the stationary interferometer (when no acoustic waves are present) using λ_{opt} . Subsequently, when the measurement is performed the effective stationary signal level (P_{eff}) can be obtained and if no drift was experienced $P_{eff} = P_{opt}$. Conversely, when

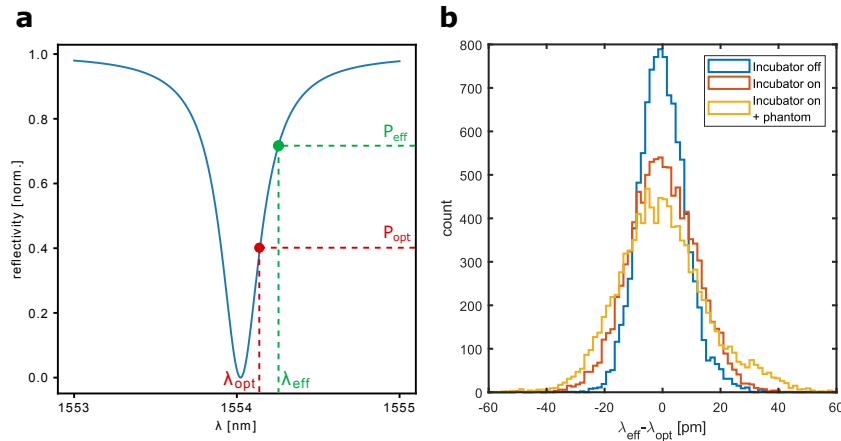


FIGURE 4.4: **Validation of the re-characterisation scheme** **a)** Explanation of the validation procedure. **b)** Histogram showing the effective wavelength (λ_{eff}) variation in respect to the optimal wavelength (λ_{opt}).

$P_{eff} \neq P_{opt}$ the ITF shape can be used to map P_{eff} back into wavelength space and infer the effective wavelength (λ_{eff}) used in the measurement.

The validation showed very good results with the drift being < 20 pm in room temperature conditions (**Figure 4.4b, blue histogram**) which is negligible for the effective sensitivity of the FPI (see **Chapter 7** for details). However, as the experiments are performed under 37°C using an incubator with a sample present on top of the interferometer we wanted to test the variability in λ_{eff} also under these conditions. As expected the variability becomes larger with the incubator turned on (**Figure 4.4b, red histogram**) and still larger when an agarose phantom is placed on top of the FPI (**Figure 4.4b, yellow histogram**), however, this amount of drift is still negligible for the effective sensitivity of the FPI.

4.3 First acoustic measurements

To validate the functionality of the setup, I measured acoustic signals generated by a synthetic ultrasound source (ultrasound transducer). **Figure 4.5** shows both the time domain signal as well as the frequency components of this recorded signal which match well with the source frequency spectrum. This confirms that, in principle, the setup and sensors are capable of recording acoustic waves at ultrasonic frequencies in the MHz regime which are required for PA imaging.

As synthetic US sources generate pressures much higher than expected in photoacoustic imaging, I validated the capability of the setup to sense PA waves by detecting signals from a dye loaded agarose phantom (**Figure 4.6**). Additionally, this measurement shows the large dependence of FPI pressure sensitivity on the optimal wavelength discussed in **Section 4.1.2**.

4.4 Preliminary imaging of small organisms

As a first biological validation target we chose to image zebrafish embryos as they have beneficial characteristics for proof of principle imaging. They are small, optically transparent (**Figure 4.7a**) and survive under water making them perfect samples for PAT validation.

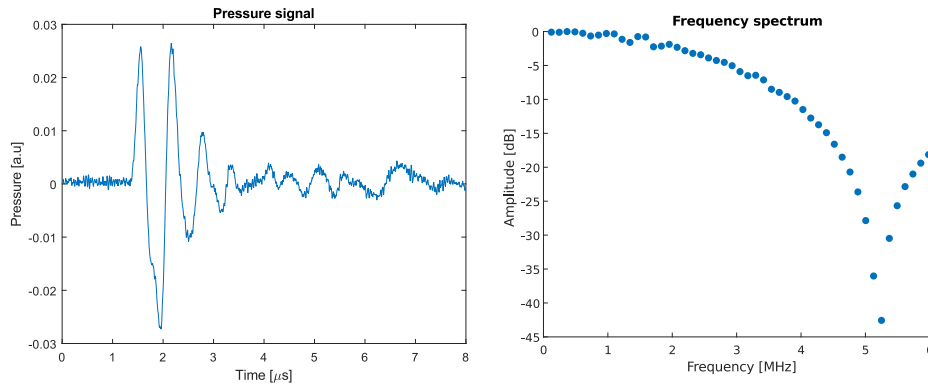


FIGURE 4.5: **Acquired pressure signals (left)** Time domain recording of a synthetic US wave. **(right)** The frequency spectrum of the acquired signal that matches well with the specification of the used ultrasound source ($f_{-6dB} = 3.2$ MHz).

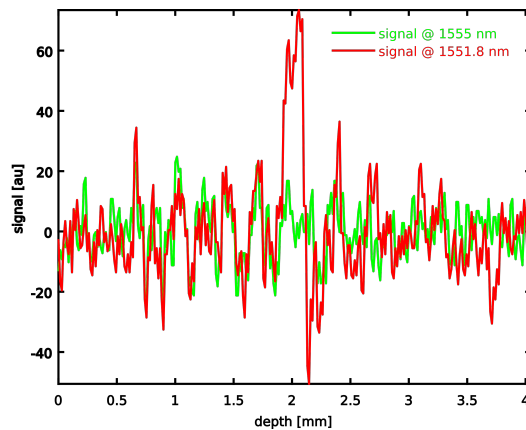


FIGURE 4.6: **Acquired PA pressure signal** By detuning the laser wavelength from the optimal value ($\lambda_{opt} \approx 1551.8$ nm) the signal is lost showing the high dependence of sensitivity on the laser wavelength.

I performed label-free imaging of the endogenously present melanin using 600 nm excitation light (**Figure 4.7b**). Comparing the PA images with the bright-field (BF) can see that PA allows for efficient imaging of highly pigmented cells (e.g melanocytes), in this case the sensitivity can reach single melanocytes due to the high melanin content of these cells.

The recorded images can be used for rough estimation of the achievable resolution *in vivo*. The resolution is slightly better in the axial dimension than in the lateral dimensions (**Figure 4.7c,d**) which is expected based on the literature (Jathoul et al., 2015). Overall we achieve a ~ 50 - 60 μm resolution which is comparable to what was obtained previously in transparent samples (Zhang, Laufer, and Beard, 2008).

4.5 Preliminary imaging of mice

Small transparent animals may be the best validation targets for PAT, but fundamentally they do not constitute very interesting objects to study using this technique as several more powerful light based approaches have been developed for transparent sample imaging (Prevedel et al., 2014; Stelzer, 2015; Wagner et al., 2019). The primary target for PAT are larger strongly scattering samples such as mammalian tissues or even humans for clinical PAT.

These samples pose great challenges for PAT imaging due to a combination of

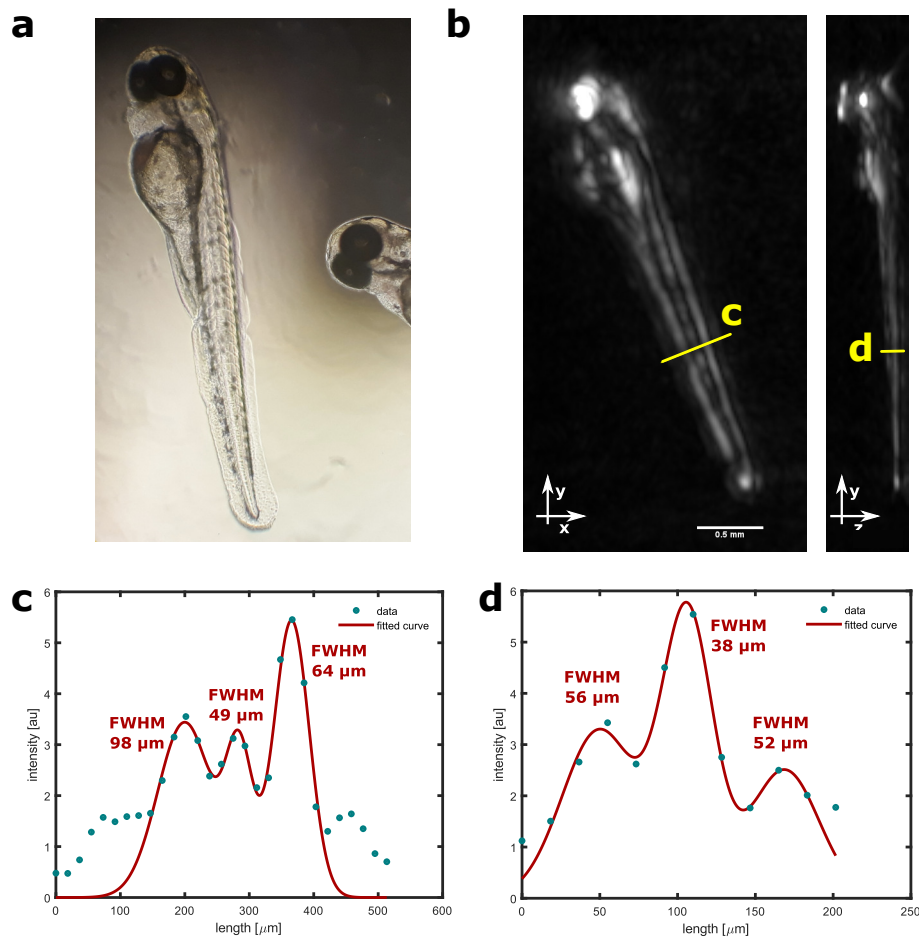


FIGURE 4.7: **Zebrafish embryo imaging** a) Brightfield image of a 3 dpf embryo for visual comparison. b) 3D PA image of a 3 dpf embryo @ 600 nm using endogenous melanin as contrast. c,d) Linescans across the imaged volume with multi-gaussian fits for rough quantification of the resolution.

reasons: (1) due to their large size there might be significant speed-of-sound variation within the sample which is difficult to compensate in the image reconstruction step, leading to acoustic aberrations that deteriorate image quality (more on this topic in **Section 7.1**); (2) similarly, as this large volume is filled with a large variety of chemical entities there might be significant attenuation of excitation light which is also dependent on the excitation wavelength (more on this topic in **Section 4.6.1**); (3) specifically for our application the absorption of excitation light within the imaged tissues might lead to sufficient heating to disrupt the accuracy of the FPI pre-characterisation and require re-characterisation as described in **Section 4.2.2**.

Having the challenges of PAT for larger samples in mind, we performed label-free imaging in the mouse abdominal area (**Figure 4.8a**) to visualise the vasculature using hemoglobin as contrast. This and other mouse imaging experiments were all performed according to a similar protocol which will be described below, should any deviations from this protocol be present in subsequent described experiments they will be discussed directly in the text. Reconstructed images showed very nice quality and amount of detail (**Figure 4.8b left**) together with a few millimeter penetration depth (**Figure 4.8b right**). The resolution was coarsely estimated to be on the order of $\sim 50\text{-}60\ \mu\text{m}$ (**Figure 4.8c**) in the superficial layers which is in accordance with published values for this type of application and setup (Jathoul et al., 2015).

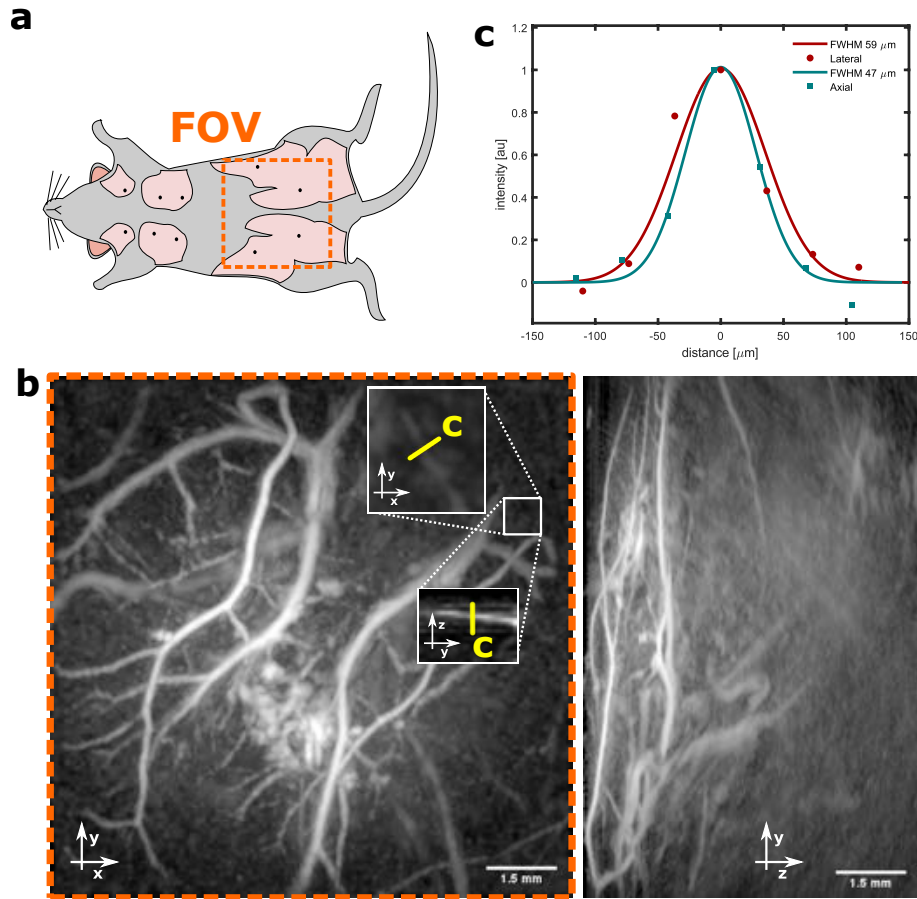


FIGURE 4.8: **Label free mouse imaging** a) Cartoon showing the FOV of the image. b) 3D PA image of a mouse abdominal vasculature at 600 nm using endogenous hemoglobin as contrast. Insets showing zoomins on small vessels in the superficial layers of the skin. c) Linescans across the vessels roughly quantifying the x-y and z resolution.

4.5.1 Photoacoustic imaging and image reconstruction

All *in vivo* mouse experiment procedures were approved by the EMBL Institutional Animal Care and Use Committee (IACUC). A water based gel was placed between the skin and the FPI sensor to provide acoustic coupling. Body temperature of the mice was kept constant during the experiments using an incubation chamber surrounding the FPI. The diameter of the excitation beam (SpitLight DPSS EVO I OPO 100 Hz, InnoLas Laser GmbH) incident on the skin surface was ≈ 1.5 cm with fluence ≈ 1 mJ cm $^{-2}$ which is within the safe maximum permissible exposure range for skin (“IEC 60825–1, Radiation Safety of Laser Products and Systems” 1994).

The field-of-view on the FPI sensor was $\approx 10 \times 10$ mm 2 and scans were acquired from $\approx 10,000$ positions, with each waveform spanning over 1000 time points (sampling rate 125 MHz, ATS9440-128M, AlazarTech). The overall tomographic image acquisition time was ≈ 10 min and was limited by the response time of laser tuning. The effective acoustic detector size was approximately 80 μ m (given by the diameter of the focused interrogation laser beam).

PA images were reconstructed from the raw data using the following steps: The acquired PA signals were interpolated onto a three times denser spatial grid. The speed of sound in the tissue was estimated using a data driven autofocus approach (Treeby et al., 2011). 3D-images were reconstructed from the interpolated signals using a time-reversal algorithm (Treeby, Zhang, and Cox, 2010) using the speed of

sound estimated in the previous step as a parameter. The image reconstruction was done using an open-source Matlab toolbox (k-Wave Treeby and Cox, 2010).

4.6 Longitudinal tracking of tumour progression in mice using multispectral photoacoustic tomography

Examples from **Section 4.4** and **Section 4.5** show that our system is capable of high resolution mesoscopic imaging *in vivo*. However, they are limited only to single color imaging (in the sense that only one chemical entity is being imaged) and they use endogenous contrast. In practice, in life sciences it is often crucial to be able to visualise multiple chemical entities (such as multiple fluorescent proteins in fluorescent microscopy) as well as to selectively label and follow chosen populations of cells. As such approaches were previously reported also for PAT (Jathoul et al., 2015, among others), I validated the capabilities of our system to perform such measurements by performing multispectral photoacoustic tomography (MS-PAT) and tracking the growth of tumours in mouse models.

4.6.1 Multispectral photoacoustic tomography

As discussed in **Chapter 2**, although the excitation of PA signals is highly similar to excitation of fluorescence, the emissions differ drastically. One of the consequences is the fact that conversely to fluorescence in PA chemical entities cannot be distinguished based on solely on the information present in the emitted signal. This disallows multispectral (or multicolour) imaging based on the same approaches as in fluorescence and requires the use of other techniques. Additionally, absorption spectra of endogenously present chromophores (such as hemoglobin or melanin) are extremely broad (**Figure 4.9**) providing a background in most spectral windows used for PA imaging.

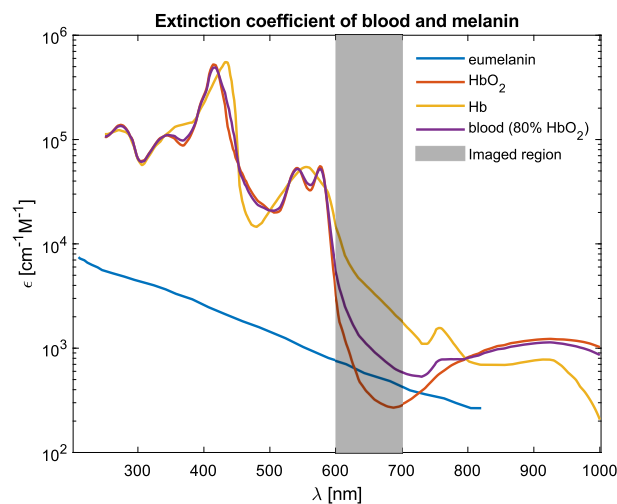


FIGURE 4.9: **Absorption spectra of melanin and haemoglobin** Imaged region corresponds to the range of wavelengths used in our setup for multispectral imaging.

Linear unmixing

The most common solution to the problem of multispectral photoacoustic tomography is the use of linear unmixing methods. Here, the signal is assumed to originate

from a mixture of chemical entities with unknown concentrations, but known absorption spectra. By taking images at distinct wavelengths, where the absorption spectra differ significantly, the concentrations of all the chemical entities can then be unmixed in post-processing via a simple computational approach. This approach enables very useful applications of PAI (Ntziachristos and Razansky, 2010), including functional measurements of blood oxygenation (Zhang et al., 2006).

More elaborate unmixing approaches can also be used to yield better result or require less priors. For example, principal component analysis and independent component analysis were shown to successfully separate chemical entities in images even in the absence of known absorption spectra, moreover these approaches could also be used to reconstruct the experimental absorption spectra directly from the images (Glatz et al., 2011). Additionally, other approaches such as the hyperspectral phasor (Cutrale et al., 2017) used in fluorescent imaging might enable more noise-robust unmixing and reduce the cross-talk between the unmixed channels.

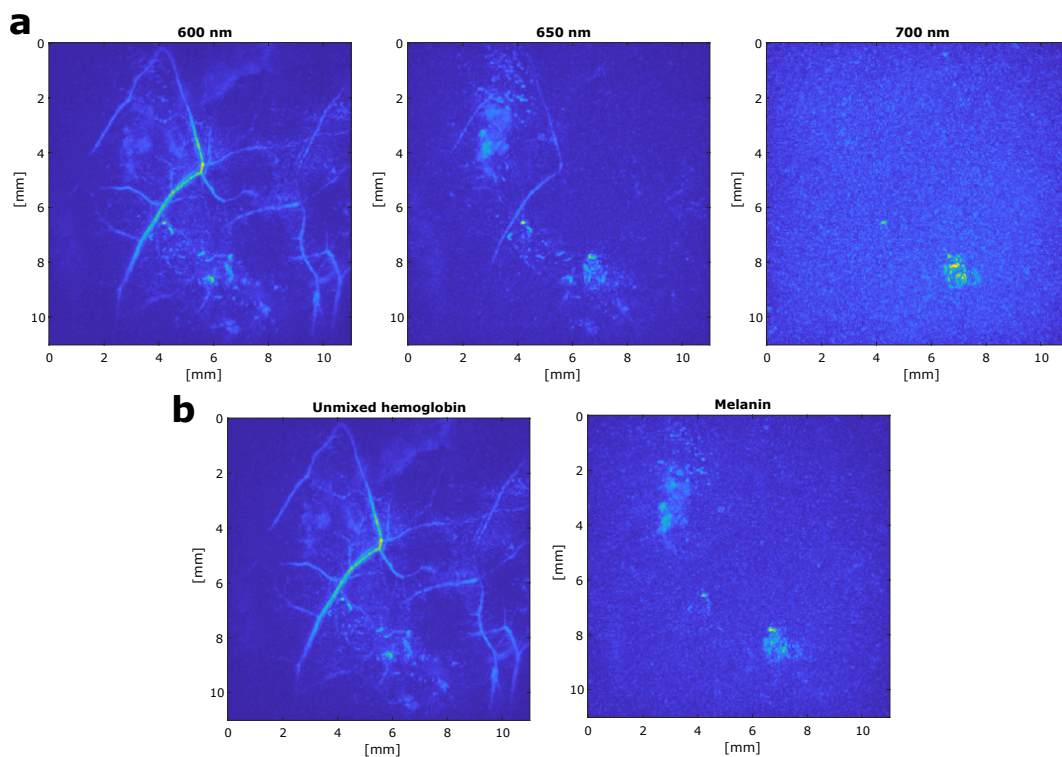


FIGURE 4.10: **Validation of the linear unmixing scheme** **a)** Images of the mouse abdominal area taken at distinct excitation wavelengths. **b)** The unmixed images of melanin and hemoglobin.

It is also important to mention the pitfalls and challenges of linear unmixing. The most important of which is the implicit assumption that the relative excitation light fluence in each voxel is known. As discussed in **Section 2.2**, estimating the excitation light fluence in a biological sample is very challenging. In MS-PAT this challenge is more manageable as we are only interested in the relative differences between the excitation wavelengths used in the experiment. Artifacts can arise from two distinct sources: **(1)** differences in bulk tissue optical properties (scattering and more importantly absorption) between the used wavelengths, and **(2)** local structures that differ in the absorption of the wavelengths used (including the chemical entities we want to image).

Both (1) and (2) can cause an effect called spectral filtering where as the excitation light travels through the tissue the ratio of different wavelengths slowly changes, leading to MS-PAT being less accurate and more prone to artifacts at larger depths. If the excitation wavelengths used are close together, the effects of (1) can be minimised, however, (2) cannot be easily tackled despite large efforts being focused on this problem.

I validated the MS-PACT approach by collecting images of the abdominal region of mice at various excitation wavelengths (spanning from 600 nm to 700 nm, **Figure 4.10a**) and used a standard linear unmixing approach (**Figure 4.10b**). It can be observed that superficially the unmixing seems to work as the melanin image is free of the vessel structures which are properly unmixed into the hemoglobin channel. The presence of signal in the melanin channel might be surprising, however it is important to note that black mice were used in this imaging experiment and the signal can probably be attributed to natural pigmentation of the skin. This raises an important point for using melanin based reporter systems for tracking selected populations of cells *in vivo*. Namely, that the choice of mouse strain can severely affect the background of our images.

4.6.2 Tracking melanoma growth in nude mice

To validate the multispectral imaging capabilities of our setup, we performed longitudinal tumour growth imaging experiments inspired by the previous literature (Jathoul et al., 2015). Animals (Nu/Nu mice) were subcutaneously injected with 10^5 B16F0 melanoma cells (according to Overwijk and Restifo, 2000) and the tumour growth was monitored over the period of ≈ 2 weeks using MS-PAT, after which the mice were sacrificed by cervical dislocation when the tumours grew too large.

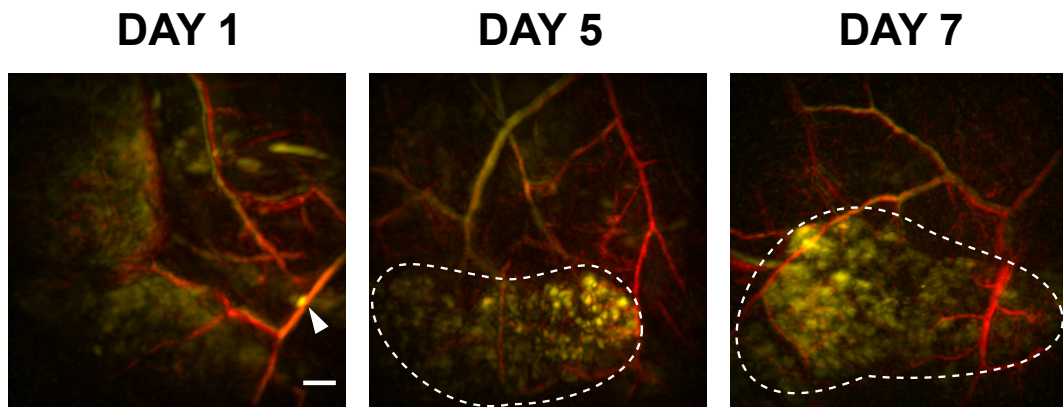


FIGURE 4.11: Tracking melanoma growth in nude mice Maximum intensity projections of images taken 1, 5 and 7 days post injection of the mice with B16F0 melanoma cells. The red and yellow channels show the unmixed blood and melanin, respectively. White arrow denotes a possible tumour cell colony on day 1. Dotted line roughly outlines the tumour mass on days 5 and 7.

We observed very rapid tumour growth which is in accordance with reports in the literature (Overwijk and Restifo, 2000) and after a few days we could easily identify tumours in the reconstructed photoacoustic images (**Figure 4.11**). The images were demixed using the approach described in **Section 4.6.1**, however, some bleed-through can be observed between the channels (as few vessels appear partially yellow) which is not expected.

There are several possible explanations of this problem: (1) the tissue could deform in the time period when the multispectral dataset was taken; (2) there is not sufficient spectral data to efficiently separate the two channels; (3) the absorption spectra of molecules might differ *in vivo* as compared to when they are characterised *in vitro*; (4) the excitation light fluence distribution might vary between the channels (as described in Section 4.6.1).

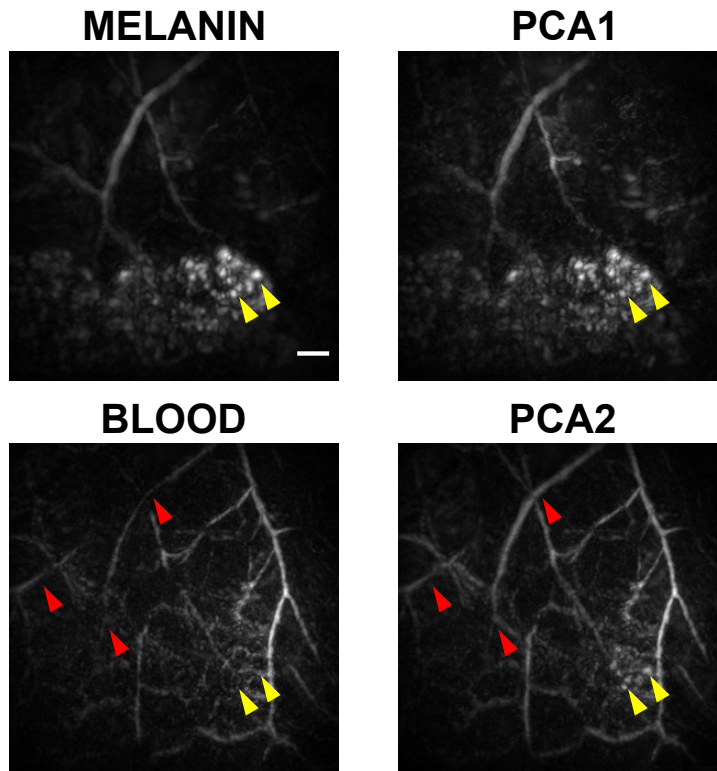


FIGURE 4.12: **Comparing linear and PCA based spectral unmixing methods** Red arrows indicate differences in unmixing performance for blood, while yellow arrow point to regions with melanin signal bleed-through.

These concerns can be addressed in the following way. (1) Although cross-correlation-based alignment was performed on the images before the unmixing algorithm was used this does not correct for local tissue deformations. Because of that, more complex non-rigid body transformation approaches should be used in the future to correct for the possible deformations. (2) Additionally, only three spectral channels (600 nm, 650 nm and 700 nm) were used for image acquisition and the system was assumed to consist of 2 components (blood and melanin) for the purpose of unmixing. This is a simplification as blood is a mixture of oxygenated and deoxygenated hemoglobin which differ in their absorption spectrum. As such, in the future the system should be treated as a 3 component mixture and more spectral channels (5-7) should be used to ascertain sufficient spectral sampling. (3) The concerns about spectral differences can be tackled with the use of blind demixing approaches which find correlated components in the images without prior knowledge of the spectra. To test this, we performed blind demixing using a principal component analysis (PCA) based approach which treats pixels as separate data-points and finds correlated variations in intensity with changing excitation wavelength. It can be observed that this approach results in very similar demixing as the previous linear scheme (Figure 4.12) with minor differences. The PCA approach seems to perform better unmixing blood as it results in a more connected vascular network

(**Figure 4.12 red arrows**), but at the same time is more prone to bleed-through from the melanin channel (**Figure 4.12 yellow arrows**). All in all, the PCA does not solve the unmixing problem completely, although it offers a qualitative improvement over the linear unmixing algorithm. As discussed before, problem **(4)** cannot be easily solved and it's potential effects are difficult to estimate on a complex biological sample.

Chapter 5

Improving sensitivity of Fabry-Pérot based photoacoustic systems

With the PA system implemented and validated, we now turn toward ways to improve the systems performance. Especially important in the context of high-performance imaging is sensitivity. As FPIs are optical devices, it is important to understand the light-cavity interactions that govern their performance on a fundamental level. Optical aberrations are known to be a major problem for multiple types of optical devices and FPIs are not excluded from this list. However, the particular effects of optical aberrations on the sensitivity of FP cavities used in pressure sensing are not well described. The text of **Section 5.1** has been taken from Czuchnowski and Prevedel, 2020 and has been originally written by myself. Additionally, the text of **Section 5.2** has been taken from Czuchnowski and Prevedel, 2021 and has been originally written by myself.

5.1 Understanding the effects of aberrations on the FPI sensitivity

The effects of optical aberrations on FP sensitivity were previously studied for *confocal* FP cavities. However, these cavities differ substantially from *planar* FP cavities as the electro-magnetic field in the former is quasi-stationary, i.e. not changing between subsequent reflections. For gravitational wave detectors, Bond *et al.* (Bond *et al.*, 2011) studied the role of mirror distortions and showed that they redistribute power among higher order laser modes (Laguerre–Gaussian), which was later demonstrated experimentally for several aberrations by Gatto *et al.* (Gatto *et al.*, 2014). Additionally, several studies have explored the potential use of short FP cavities for aberration sensing (Mah and Talghader, 2019; Takeno *et al.*, 2011) or examined the effects of manufacturing imperfections on the performance of tunable micromirror cavities (Liu and Talghader, 2006).

Nevertheless, the effects of optical aberrations on *planar* FP cavities (i.e. composed of flat mirrors) are generally much less studied, and in particular for micro-cavities interrogated by focused laser beams (**Figure 5.1a**). In turn, *planar* FP cavities have recently been shown to be promising candidates for highly sensitive ultrasound sensors for use in photo-acoustic imaging (Zhang, Laufer, and Beard, 2008; Jathoul *et al.*, 2015). Here, large efforts have been devoted to improving their manufacturing techniques (Buchmann *et al.*, 2017; Villringer *et al.*, 2019). However, a general theoretical framework to understand the interactions between arbitrary light

modes and their cavity counterparts is currently lacking. While recent work (Marques et al., 2020) provided an accurate theoretical model for calculating reflectivity spectra for *ideal* FP micro-cavities interrogated with focused beams their model does not allow to draw general conclusions on the effects of optical aberrations on FP sensitivity.

This section introduces a general framework to study arbitrary light-cavity interactions that provides a broader understanding of the mechanisms by which optical aberrations degrade FP sensitivity. The presented framework is based on extending the 'unfolded cavity approach' (Varu, 2014; Abu-Safia et al., 1994) to account for beam aberrations by employing Gaussian Beam Mode Analysis (GBMA) (Tsigaridas et al., 2003). GBMA is based on Laguerre-Gaussian mode decomposition and beam propagation, which enables numerical investigations of the coupling between arbitrarily aberrated Gaussian beams and Laguerre-Gaussian cavity modes (**Figure 5.1b,c**).

5.1.1 Theoretical approach

Since in theory the ITF is symmetrical, photoacoustic pressure measurements can be done on both the falling as well as the rising edge. We thus define two types of normalised optical sensitivity: S_o^+ (rising edge sensitivity) and S_o^- (falling edge sensitivity):

$$S_o^\pm = \frac{\pm \frac{d}{d\lambda} I_{FPI}(\lambda) \Big|_{\lambda=\lambda_{opt}^\pm}}{I_{FPI}(\lambda_{opt}^\pm)} \quad (5.1)$$

where,

$$\lambda_{opt}^\pm = \operatorname{argmax} \left\{ \pm \frac{d}{d\lambda} I_{FPI}(\lambda) \right\} \quad (5.2)$$

is the bias wavelength, and

$$I_{FPI}(\lambda) = \iint_A E_{FPI}(r, \phi, \lambda)^* E_{FPI}(r, \phi, \lambda) dA \quad (5.3)$$

is the Fabry-Pérot interferometer transfer function, where A is the field aperture, E_{FPI} is the interfering electric field given by:

$$E_{FPI}(r, \phi, \lambda) = r_1^L E(r, \phi, 0, \lambda) + \sum_{k=1}^{\infty} \beta_k E(r, \phi, z_k, \lambda'), \quad (5.4)$$

with $z_k = 2l_0k$, $\beta_k = (t_1)^2 (r_1^R)^{k-1} (r_2^L)^k$, $E(r, \phi, z, \lambda)$ denoting the electric field of the beam propagating in the cavity, l_0 the cavity length, λ' the effective wavelength inside the cavity, t_1 the amplitude transmission coefficient for the first mirror, and $r_1^{R/L}$ as well as r_2^L the amplitude reflection coefficients for the first mirror on the right/left side and second mirror for the left side, respectively.

The use of this definition allows normalisation for both laser relative intensity noise (RIN), as well as shot noise which are the dominant sources of noise in typical *FPI – PAT* systems. Estimation of S_o requires calculation of $E(r, \phi, z, \lambda)$ for different z planes (**Equation 5.4**), which cannot be done analytically for aberrated Gaussian

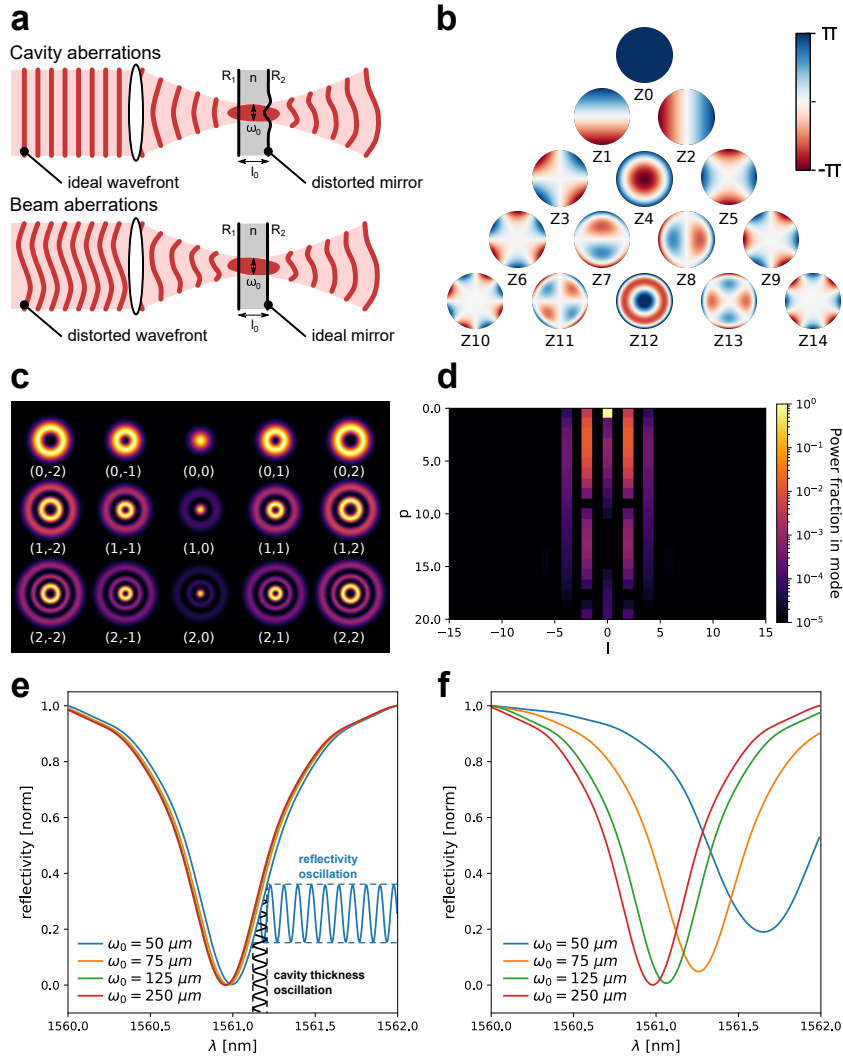


FIGURE 5.1: **Interaction between optical aberrations and cavity modes** a) A schematic conceptualising the effects of beam and cavity aberrations on the wavefront of the beam, where: R_1, R_2 - reflectivity of the two mirrors, ω_0 - beam waist radius, l_0 - cavity thickness, n - refractive index of the elastic material inside the cavity. b) Phase profile of the first 15 Zernike aberrations. c) Intensity profile of some of the low order (l, p) Laguerre-Gaussian modes. d) Decomposition of an arbitrarily aberrated beam into Laguerre-Gaussian modes. e, f) Effect of beam size on FPI transfer functions for two LG modes. e) The fundamental LG_{00} displays little dependence on increasing divergence of the beam (decreasing the spot size). Here we also show schematically how changes in cavity thickness are optically amplified at the bias wavelength. f) In contrast, a higher order LG_{55} mode displays pronounced TF distortions as a function of beam divergence. Additionally simulations for large spot sizes ($\omega_0 = 250 \mu\text{m}$) show little difference between the two modes confirming the calculations for an ideal FPI (Appendix A). For the simulations we chose the following cavity parameters: $l_0 = 20 \mu\text{m}$, $R_{1/2} = 0.95$ which are commonly used design parameters for photoacoustic tomography systems (Zhang, Laufer, and Beard, 2008). Figure reproduced from: Czuchnowski and Prevedel, 2020.

beams in general and thus requires a new theoretical framework. A number of potential approaches exist (e.g. numerically solving the Fresnel integral [Sears, 1949], or using the extended Zernike-Njober theory [Janssen, 2002]).

In this thesis Gaussian beam mode analysis (GBMA) was chosen because of the following reasons. GBMA is an established method based on decomposing optical fields into Gaussian mode bases (e.g. Laguerre-Gauss base) and is an efficient way of performing diffraction calculations (Tsigaridas et al., 2003), also for beam propagation of aberrated fields (Trappe, Murphy, and Withington, 2003) and analysis of beam aberrations in *confocal* FP cavities (Mah and Talghader, 2019). Our choice was motivated by the fact that LG-beams (**Figure 5.1c**) are natural modes for FP cavities and, as such, possess several useful characteristics (see **Section 5.1.2**). Additionally, there is an interesting correspondence between aberration magnitude and LG mode order (Mah and Talghader, 2019), where small aberrations cause significant coupling to low order LG-modes which constrains the analysis to a small number of modes speeding up the computations. We start by defining the general LG mode with indices l, p as:

$$LG_{lp}(r, \phi, z, \lambda) = C_{lp}^{LG} \left(\frac{r\sqrt{2}}{w(z)} \right)^{|l|} L_p^{|l|} \left(\frac{2r^2}{w^2(z)} \right) \exp(-il\phi) G(r, z, \lambda) \quad (5.5)$$

where C_{lp}^{LG} is a normalisation constant, $L_p^{|l|}(x)$ is the Laguerre polynomial and $G(r, z, \lambda)$ denotes a general Gaussian beam:

$$G(r, z, \lambda) = E_0 \frac{w_0}{w(z)} \exp\left(\frac{-r^2}{w(z)^2}\right) \exp\left(-i\left(\frac{2\pi}{\lambda}z + \frac{\pi r^2}{\lambda R(z)} - \psi(z)\right)\right) \quad (5.6)$$

with $w(z)$ the local beam radius,

$$w(z) = w_0 \sqrt{1 + \left(\frac{z}{z_R}\right)^2}, \quad (5.7)$$

$R(z)$ the local beam curvature,

$$R(z) = z \left[1 + \left(\frac{z_R}{z}\right)^2 \right], \quad (5.8)$$

$\psi(z)$ the Gouy phase

$$\psi(z) = \arctan\left(\frac{z}{z_R}\right), \quad (5.9)$$

and z_R the Rayleigh range of the beam

$$z_R = \frac{\pi w_0^2 n_0}{\lambda}. \quad (5.10)$$

Here, n_0 is the refractive index of the propagation medium and w_0 is the beam radius in focus. We now consider an *aberrated* Gaussian beam of the form:

$$G_a(r, \phi, z_0, \lambda) = G(r, z_0, \lambda) \exp\left(2\pi i \sum_j \alpha_j Z_j\right), \quad (5.11)$$

where α_j are the amplitude coefficients of Zernike type aberrations expressed in waves and Z_j are Zernike polynomials indexed using the OSA/ANSI standard indices ($Z_j = Z_n^m$, where $j = \frac{1}{2}(n(n+2) + m)$).

$$Z_n^m(r, \phi) = \begin{cases} A_n^m R_n^m(r) \cos(m\phi) & \text{for } m \geq 0 \\ A_n^m R_n^m(r) \sin(m\phi) & \text{for } m < 0, \end{cases} \quad (5.12)$$

with

$$R_n^m(r) = \sum_{s=0}^{(n-m)/2} \frac{(-1)^s (n-s)!}{s!((n+m)/2-s)!((n-m)/2-s)!} r^{(n-2s)}, \quad (5.13)$$

and A_n^m being a normalisation factor chosen so that:

$$\max_{r \in [0,1]} Z_n^m(r, \phi) - \min_{r \in [0,1]} Z_n^m(r, \phi) = 1. \quad (5.14)$$

The normalisation allows a direct comparison with experimental systems using deformable mirrors since their dynamic range is limited by the maximum mode amplitude they can display and thus DMs are often calibrated in mode amplitude units.

The coupling of an aberrated Gaussian beam expressed in Zernike modes with the LG-modes that propagate inside the FP cavity can now be calculated. For this we seek the electric field $E(r, \phi, z, \lambda)$ of the cavity,

$$E(r, \phi, z, \lambda) = \sum_{l=0}^{\infty} \sum_{p=0}^{\infty} c_{lp} LG_{lp}(r, \phi, z, \lambda), \quad (5.15)$$

where $|c_{lp}|^2$ denotes the fraction of optical power coupled into a particular LG_{lp} mode. These decomposition coefficients can be calculated from:

$$c_{lp} = \iint_A LG_{lp}(r, \phi, z_0, \lambda)^* G_a(r, \phi, z_0, \lambda) dA \quad (5.16)$$

where A is the field aperture. This approach allows numerical simulation of the FP interfering field (**Equation 5.4**) by calculating the aberrated electric fields for subsequent reflections inside the FPI.

5.1.2 Effects of beam aberrations on FPI sensitivity

This framework can be used to explore the effects of beam aberrations on the sensitivity of the FP cavity. We start by exploring the properties of ideal Gaussian beams and note that for a non-aberrated beam 100% of the power is confined in the fundamental cavity mode (LG_{00}). However, in the presence of beam aberrations significant coupling into higher order LG-modes can be observed (**Figure 5.1d**). This effect is also present in confocal cavities (Mah and Talghader, 2019), although there it does not degrade the sensitivity as the ITFs of different LG-modes are spectrally fully separated.

Limit case for ideal FP cavity illuminated with a non-diverging beam

We start by considering an ideal FP cavity with flat mirrors. The properties of a planar FP cavity illuminated with non-diverging beams can be analysed analytically to

evaluate the effect of optical aberrations on the ITF. We aim to calculate the transfer function $I_{FPI}^{ND}(\lambda)$ where the superscript *ND* denotes non-divergence of the beam. From **Equation 5.3** it is known that:

$$I_{FPI}^{ND}(\lambda) = \iint_A E_{FPI}^{ND}(r, \phi, \lambda)^* E_{FPI}^{ND}(r, \phi, \lambda) dA \quad (5.17)$$

And by combining **Equation 5.15** and **Equation 5.4** the interfering electric field E_{FPI}^{ND} can be expressed in terms of Laguerre-Gaussian modes:

$$E_{FPI}^{ND}(r, \phi, \lambda) = \sum_{l=0}^{\infty} \sum_{p=0}^{\infty} c_{lp} \sum_{i=0}^{\infty} \beta_i LG_{lp}^{ND}(r, \phi, z_i, \lambda) \quad (5.18)$$

where,

$$\beta_i = \begin{cases} r_1^L & \text{for } i = 0 \\ 2(t_1)^2 (r_1^R)^{i-1} (r_2^L)^i & \text{for } i > 0 \end{cases} \quad (5.19)$$

Now, we need to explore the properties of non-diverging LG modes, which can be defined as the limit when the Rayleigh range of the beam (z_R) approaches infinity:

$$LG_{lp}^{ND}(r, \phi, z, \lambda) = \lim_{z_R \rightarrow \infty} LG_{lp}(r, \phi, z, \lambda) = \lim_{z_R \rightarrow \infty} C_{lp}^{LG} \left(\frac{r\sqrt{2}}{w(z)} \right)^{|l|} L_p^{|l|} \left(\frac{2r^2}{w^2(z)} \right) \exp(-il\phi) \frac{w_0}{w(z)} \exp\left(\frac{-r^2}{w(z)^2}\right) \exp\left(-i\left(\frac{2\pi}{\lambda}z + \frac{\pi r^2}{\lambda R(z)} - \psi(z)\right)\right) \quad (5.20)$$

The limits of all the parts dependent on z_R can be evaluated separately:

$$\lim_{z_R \rightarrow \infty} w(z) = \lim_{z_R \rightarrow \infty} w_0 \sqrt{1 + \left(\frac{z}{z_R}\right)^2} = w_0 \quad (5.21)$$

$$\lim_{z_R \rightarrow \infty} \psi(z) = \lim_{z_R \rightarrow \infty} \arctan\left(\frac{z}{z_R}\right) = 0 \quad (5.22)$$

The value of r is also indirectly dependent on z_R because $r \sim w_0$ for proper beam sampling and from **Equation 5.10** we know that $w_0^2 \sim z_R$ so $r^2 \sim z_R$:

$$\lim_{z_R \rightarrow \infty} \frac{r^2}{R_z(z)} = \lim_{z_R \rightarrow \infty} \frac{z z_R}{z^2 + z_R^2} = 0 \quad (5.23)$$

With these we come back to **Equation 5.20**:

$$LG_{lp}^{ND}(r, \phi, z, \lambda) = \lim_{z_R \rightarrow \infty} LG_{lp}(r, \phi, z, \lambda) = \lim_{z_R \rightarrow \infty} C_{lp}^{LG} \left(\frac{r\sqrt{2}}{w(z)} \right)^{|l|} L_p^{|l|} \left(\frac{2r^2}{w^2(z)} \right) \exp(-il\phi) \frac{w_0}{w(z)} \exp\left(\frac{-r^2}{w(z)^2}\right) \exp\left(-i\left(\frac{2\pi}{\lambda}z + \frac{\pi r^2}{\lambda R(z)} - \psi(z)\right)\right) = C_{lp}^{LG} \left(\frac{r\sqrt{2}}{w_0} \right)^{|l|} L_p^{|l|} \left(\frac{2r^2}{w_0^2} \right) \exp(-il\phi) \exp\left(\frac{-r^2}{w_0^2}\right) \exp\left(-i\frac{2\pi}{\lambda}z\right) \quad (5.24)$$

where we reach our first conclusion by observing that $LG_{lp}^{ND}(r, \phi, z, \lambda)$ is separable:

$$LG_{lp}^{ND}(r, \phi, z, \lambda) = LG_{lp}^{ND}(r) LG_{lp}^{ND}(\phi) LG_{lp}^{ND}(z, \lambda) \quad (5.25)$$

which leads to the first property of non-diverging LG modes:

$$LG_{lp}^{ND}(r, \phi, z_i, \lambda) = LG_{lp}^{ND}(r, \phi, z_{i'}, \lambda) \exp\left(-\frac{2\pi i(z_i - z_{i'})}{\lambda}\right). \quad (5.26)$$

The second property is a consequence of orthonormality of LG-modes:

$$\delta_{l'l'} \delta_{p'p} = \iint_A LG_{lp}^{ND}(r, \phi, z_i, \lambda) LG_{l'p'}^{ND}(r, \phi, z_i, \lambda)^* dA. \quad (5.27)$$

These can be combined to achieve:

$$\delta_{l'l'} \delta_{p'p} \exp\left(-\frac{2\pi i(z_i - z_{i'})}{\lambda}\right) = \iint_A LG_{lp}^{ND}(r, \phi, z_i, \lambda) LG_{l'p'}^{ND}(r, \phi, z_{i'}, \lambda)^* dA \quad (5.28)$$

Now, we return to **Equation 5.17** and proceed to calculate the transfer function of an ideal FP cavity:

$$\begin{aligned} I_{FPI}^{ND}(\lambda) &= \iint_A E_{FPI}^{ND}(r, \phi, \lambda)^* E_{FPI}^{ND}(r, \phi, \lambda) dA \stackrel{(5.18)}{=} \\ &\iint_A \left(\sum_{l=0}^{\infty} \sum_{p=0}^{\infty} c_{lp} \sum_{j=0}^{\infty} \beta_j LG_{lp}^{ND}(r, \phi, z_j, \lambda) \right) \left(\sum_{l'=0}^{\infty} \sum_{p'=0}^{\infty} c_{l'p'} \sum_{j'=0}^{\infty} \beta_{j'} LG_{l'p'}^{ND}(r, \phi, z_{j'}, \lambda) \right)^* dA = \\ &\sum_{l=0}^{\infty} \sum_{p=0}^{\infty} \sum_{l'=0}^{\infty} \sum_{p'=0}^{\infty} c_{l'p'}^* c_{lp} \sum_{j=0}^{\infty} \sum_{j'=0}^{\infty} \beta_j^* \beta_j \iint_A LG_{lp}^{ND}(r, \phi, z_j, \lambda) LG_{l'p'}^{ND}(r, \phi, z_{j'}, \lambda)^* dA \stackrel{(5.28)}{=} \\ &\sum_{l=0}^{\infty} \sum_{p=0}^{\infty} \sum_{l'=0}^{\infty} \sum_{p'=0}^{\infty} c_{l'p'}^* c_{lp} \sum_{j=0}^{\infty} \sum_{j'=0}^{\infty} \beta_j^* \beta_j \delta_{l'l'} \delta_{p'p} \exp\left(-\frac{2\pi i(z_j - z_{j'})}{\lambda}\right) = \\ &\sum_{l=0}^{\infty} \sum_{p=0}^{\infty} |c_{lp}|^2 \sum_{j=0}^{\infty} \sum_{j'=0}^{\infty} \beta_j^* \beta_j \exp\left(-\frac{2\pi i(z_j - z_{j'})}{\lambda}\right) = \\ &\sum_{l=0}^{\infty} \sum_{p=0}^{\infty} |c_{lp}|^2 \sum_{j=0}^{\infty} \beta_j \exp\left(-\frac{2\pi iz_j}{\lambda}\right) \sum_{j'=0}^{\infty} \beta_{j'}^* \exp\left(-\frac{2\pi iz_{j'}}{\lambda}\right)^* \quad (5.29) \end{aligned}$$

Taking in consideration the following relation:

$$\sum_{j=0}^{\infty} \beta_j \exp\left(-\frac{2\pi iz_j}{\lambda}\right) = E_{FPI}^{Airy}(\lambda) \quad (5.30)$$

where $E_{FPI}^{Airy}(\lambda)$ is the well known solution for an ideal FPI illuminated with a plane wave. And normalisation of the power of the beam:

$$\sum_{l=0}^{\infty} \sum_{p=0}^{\infty} |c_{lp}|^2 = 1 \quad (5.31)$$

We conclude:

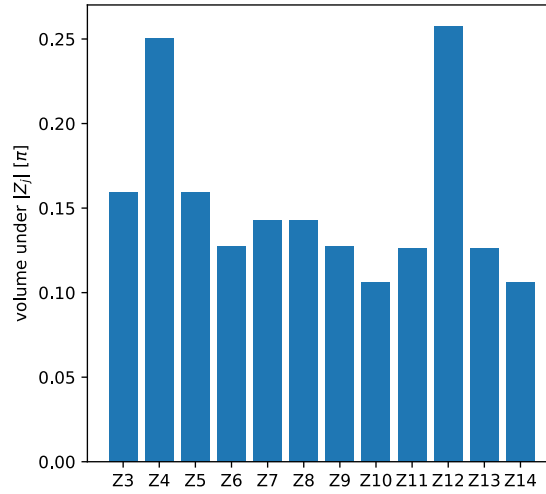


FIGURE 5.2: **Volume under the absolute value of the Zernike polynomial (VuP)** showing differences which may contribute to differential effects of Zernike aberrations on FPI sensitivity ($VuP_j = \int_0^1 \int_{-\pi}^{\pi} |Z_j(r, \phi)| r d\phi dr$). Figure reproduced from: Czuchnowski and Prevedel, 2020.

$$I_{FPI}^{ND}(\lambda) = E_{FPI}^{Airy}(\lambda) E_{FPI}^{Airy}(\lambda)^* = I_{FPI}^{Airy}(\lambda) \quad (5.32)$$

This shows that a non-diverging beam will create an ideal Airy interference pattern inside of an FP cavity regardless of its decomposition into LG-modes. As any beam can be represented as a linear combination of LG-modes this shows that an FP cavity illuminated with a non-diverging beam is inherently resistant to beam aberrations. Important to note is that this conclusion does not hold for confocal cavities because the interference patterns of different LG-modes experience a spectral shift due to the curvature of the mirrors.

Case of an ideal FP cavity illuminated with a diverging beam

Calculations show that all LG modes create the same transfer function (**Figure 5.1e, f**) if the beam diameter is sufficiently large compared to the thickness of the FP cavity. This extreme case serves as a check of the analytical result from the previous section. However, in realistic experimental conditions the interrogation light is focused on the FP cavity to a spot size $w_0 \leq 50 \mu\text{m}$ which will significantly reduce the Rayleigh range of the beam, effectively leading to spectrally shifted and distorted ITFs, especially for higher order LG modes (**Figure 5.1f**). Consequently, this will have serious implications on the cavity robustness as coupling into higher order modes will cause broadening of the ITF and deterioration of the sensitivity.

With this general observation in mind, we now start investigating the effects of *single* Zernike modes on the sensitivity of the FPI. The conceptual procedure of our simulations is shown in **Figure 5.3a** and is based on numerical evaluation of equations outlined in **Section 5.1.1**. We observe that while FP sensitivity (S_o^\pm) generally declines with increasing amplitude for all types of Zernike aberration, the magnitude of their effect is highly heterogeneous (selected examples in **Figure 5.3b**). To directly compare all selected Zernike modes, we calculate the mode amplitude (α_j)

that reduces sensitivity to 50% of the initial value (**Figure 5.3c**). This characteristic point S_{50}^{\pm} assesses the effective strength of different modes in degrading the optical sensitivity and as such, is important from a practical perspective. Interestingly, we find that Z12 (primary spherical aberration) has the strongest negative effect on the FPI sensitivity, followed by Z4 (defocus) and Z11/Z13 (secondary astigmatism). These modes cause the strongest coupling to higher order LG modes, presumably because of a combination of factors. Firstly, Zernike polynomials display different values of the volume under the polynomial (VuP) for a constrained amplitude resulting in variations of the overall phase aberration introduced in the beam (**Figure 5.2**). Z12 and Z4 have the largest VuP which might explain their strong effects on the sensitivity of the FPI. VuP does not, however, fully account for the differences between individual Zernike modes (e.g. the case of Z11/Z13). Additionally, there are more subtle properties of Zernike modes in play, such as the ring-shaped phase of Z12 (**Figure 5.1b**) matching well the profiles of higher order LG-modes (**Figure 5.1c**), therefore facilitating an efficient coupling.

In realistic experimental systems, aberrations are never present in isolation, but rather occur as a mixture of many modes with varying weights. Hence, we decided to explore the interactions between different types of Zernike aberrations by using a Monte-Carlo approach to analyse these interactions in a high-throughput manner (**Figure 5.3a**). In order to segregate optical aberrations into groups we decided to keep the total aberration magnitude constant for each group ($Z_{tot} = \sum \alpha_j = const$). In such situation the mean sensitivity decreases as the total aberration magnitude increases (**Figure 5.3d**). Additionally, the variance in sensitivity increases for stronger aberrations. The source of this variation can be analysed by calculating the correlation between the sensitivity (S_o) and the aberration magnitude for each of the modes (α_j) within a group where $Z_{tot} = const$. For $Z_{tot} = 2$ there is a strong negative correlation with mode Z12 (spherical aberration) (**Figure 5.3e**) which is in line with the results for single modes where Z12 has a much stronger impact on the optical sensitivity than the rest of modes (**Figure 5.3c**).

A very interesting finding of these investigations of the effects of beam aberrations is that a single parameter shows a strong linear correlation with the simulated optical sensitivity S_o^{\pm} (**Figure 5.3f**). This parameter is the power fraction conserved in the fundamental Gaussian (LG_{00}) mode which suggests that the principal mechanism behind loss of sensitivity might be the aberration induced loss of power in the fundamental mode.

5.1.3 Effects of cavity aberrations on FPI sensitivity

The previous section discussed the effect of beam aberrations on the transfer function of the FPI. However, there is a special class of optical aberrations that needs to be treated separately in this framework, namely, the aberrations that are accumulated while the beam is propagating *inside* the cavity. Since the beam makes several round trips ($\sim 35 - 45$ as reported in Zhang, Laufer, and Beard, 2008) in the cavity any phase delay induced *inside* will add up at each reflection. These spatially varying phase delays can e.g. be induced by mirror imperfections (**Figure 5.4a**) and require a more elaborate theoretical treatment.

We start by describing the cavity mirror shape by a combination of Zernike polynomials (following Bond et al., 2011):

$$\mathcal{M}(r, \phi, \lambda) = \sum_j \gamma_j(\lambda) Z_j(r, \phi) \quad (5.33)$$

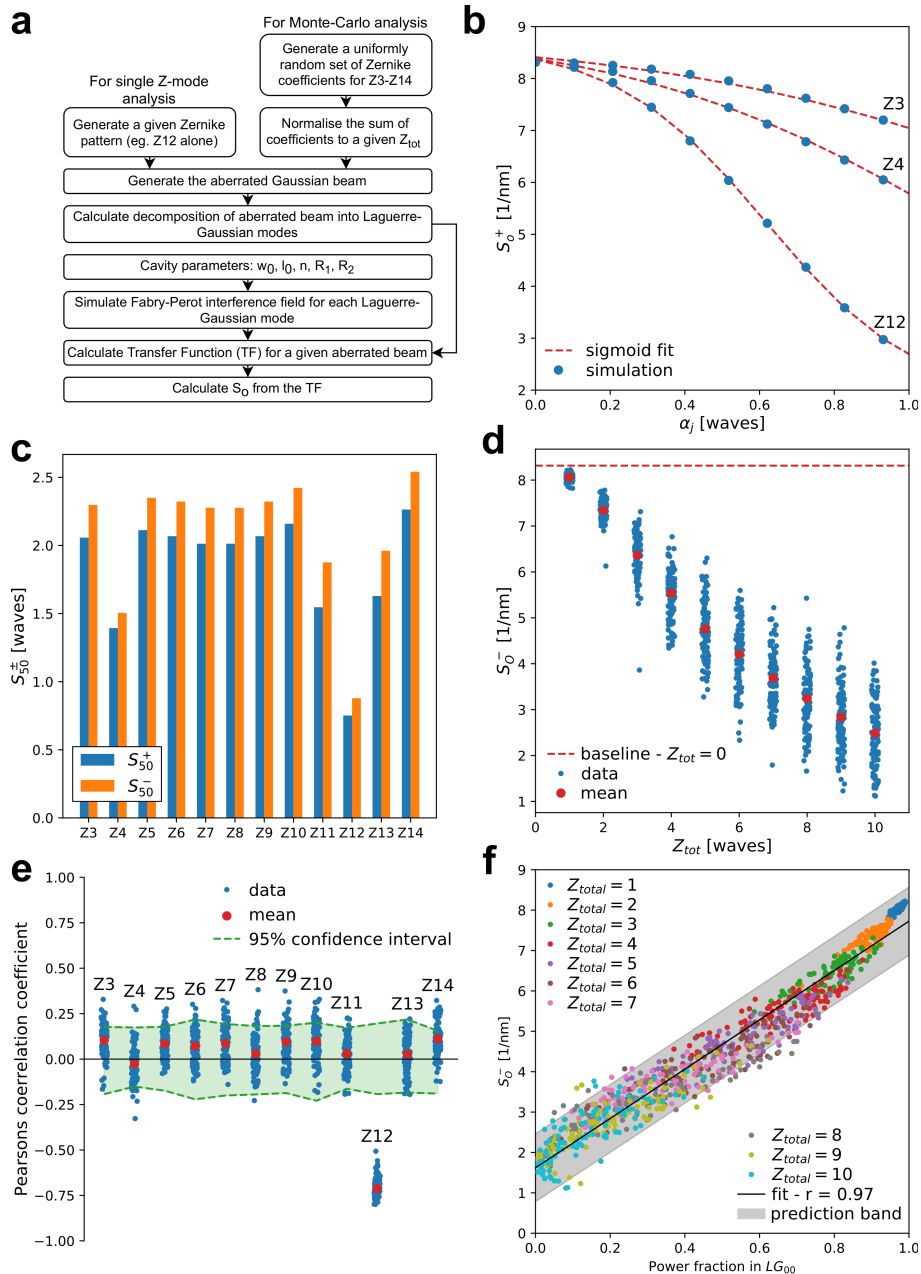


FIGURE 5.3: **Effects of beam aberrations** **a**) Flowchart of the simulation procedure. **b**) Exemplary graphs of the dependence of S_0^+ on the mode amplitude (α_j) for modes Z3, Z4 and Z12. All Zernike modes display a sigmoidal dependence. **c**) Quantification of the effect of different Z-modes on the FPI sensitivity expressed as the aberration magnitude required to lower the sensitivity to 50% the initial value (Z_{50}) for both the falling as well as the rising edge. **d**) Dependence of the sensitivity (S_0^+) on the total aberration (Z_{tot}). Each data point is the outcome of an independent simulation with randomly generated aberration. **e**) Correlation between the magnitude of a particular Z-aberration and the overall sensitivity for a given mixture of aberrations with $Z_{tot} = 2$. The slight positive correlation for modes other than Z4 and Z12 is the result of the way we constrain the Zernike amplitudes ($Z_{tot} = const$). Consequently a high amplitude of a weaker mode will reduce the amplitude of modes Z12 and Z4 resulting in a higher overall sensitivity for a constant Z_{tot} . **f**) Correlation between the falling edge sensitivity (S_0) and the power conserved in the fundamental LG_{00} mode. The prediction band is the confidence interval for predicting a sensitivity value (S_0) given the power contained in the LG_{00} mode, taking into consideration both the confidence of the fit as well as the variance of the data. The band is set for a 95% confidence interval and thus contains 95% of the measured points. Figure reproduced from: Czuchnowski and Prevedel, 2020.

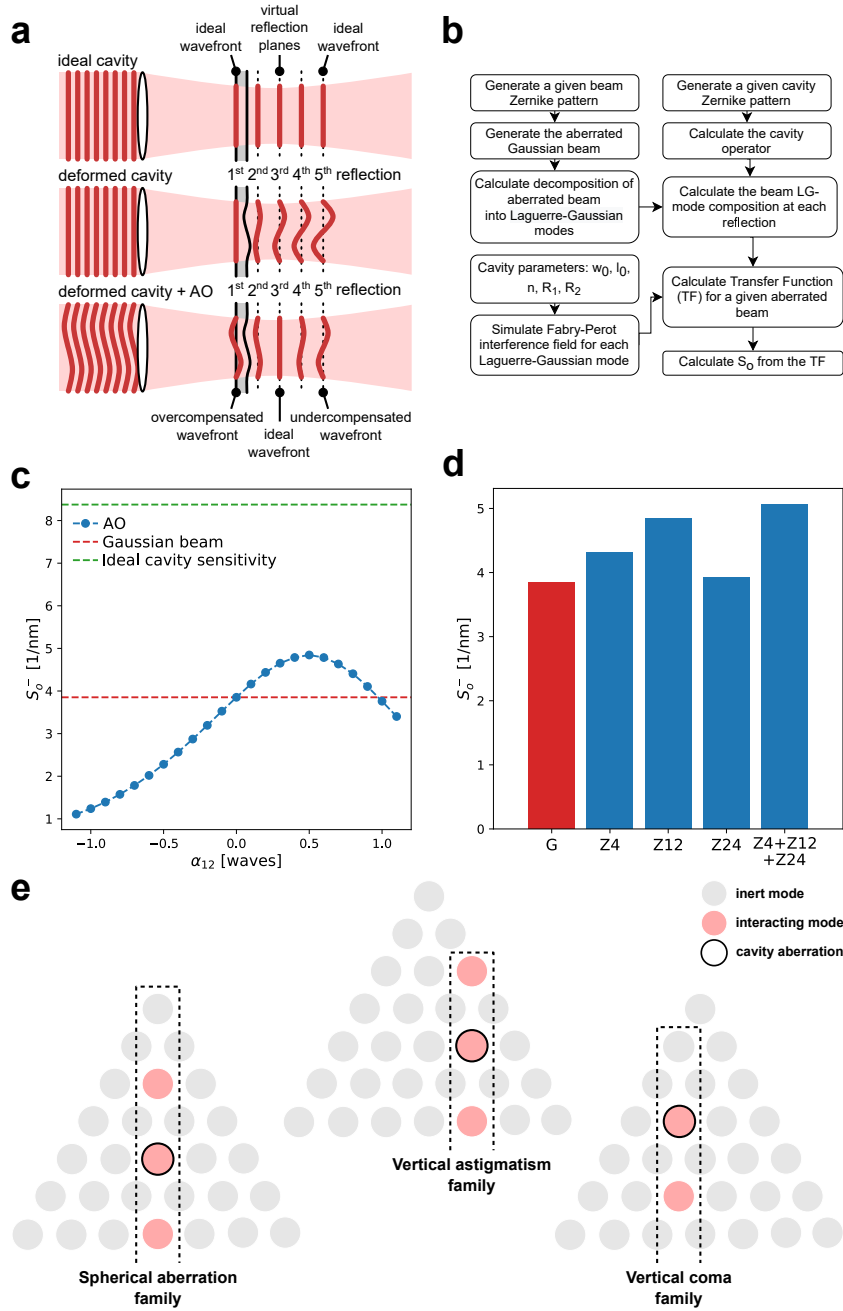


FIGURE 5.4: **Effects of cavity aberrations** **a)** A schematic conceptualising the limitations of adaptive optics in fully compensating the effects of cavity aberrations. **b)** Flowchart of the simulation procedure. **c)** AO correction of a $\gamma_{12} = 0.02$ aberrated cavity using mode Z12. **d)** Quantification of sensitivity for correcting γ_{12} using different Z-modes as well as their combination, which achieves the highest sensitivity. Here, the cavity deformation was chosen as $\gamma_{12} = 0.02$. **e)** Z-mode interactions in different deformed cavities. For all cavities: $\gamma = 0.02$. Figure reproduced from: Czuchnowski and Prevedel, 2020.

where, $\gamma_j(\lambda)$ is the magnitude of the phase delay introduced to the beam by the mirror deformation (expressed in waves). As mentioned before, because this phase delay is reapplied at each reflection, it requires a modified approach as compared to beam aberrations. By combining Equation 5.15 with Equation 5.4 the interfering electric field $E_{FPI}(r, \phi, \lambda)$ can be expressed in terms of Laguerre-Gaussian modes:

$$E_{FPI}(r, \phi, \lambda) = \sum_{s=0}^{\infty} c_s \left[r_1^L LG_s(r, \phi, 0, \lambda) + \sum_{k=1}^{\infty} \beta_k LG_s(r, \phi, z_k, \lambda') \right] \quad (5.34)$$

where $s = (|l| + p)^2 + l + |l| + p$ and l, p are LG indices. However, due to cavity aberrations the decomposition of beam into LG modes of weight c_s changes at each reflection k . Therefore, the interfering electric field in an distorted (aberrated) cavity takes the form:

$$E_{FPI}^M(r, \phi, \lambda) = \sum_{s=0}^{\infty} \left[c_s^0 r_1^L LG_s(r, \phi, 0, \lambda) + \sum_{k=1}^{\infty} c_s^k \beta_k LG_s(r, \phi, z_k, \lambda') \right] \quad (5.35)$$

where $|c_s^k|^2$ denotes the fraction of power coupled into mode LG_s at reflection k . Because the beam decomposition into LG modes changes at each reflection, the coefficients c_s^k need to be calculated iteratively:

$$c_s^k = \sum_{s'} c_{s'}^{k-1} \iint_A LG_s(r, \phi, z_k, \lambda)^* LG_{s'}(r, \phi, z_k, \lambda) \mathcal{M}(r, \phi, \lambda) dA \quad (5.36)$$

This approach is computationally expensive in practice, but can be greatly simplified by assuming that the increase of beam diameter inside the cavity during propagation is small. In this particular case when the beam diameter $w_0 = 50 \mu m$ and cavity thickness $l_0 = 20 \mu m$, the beam will only increase in diameter $\sim 10\%$ for an optical path length of 100 reflections. To validate that this approximation is negligible for the qualitative conclusions this section aims to draw, I performed an extended simulation that additionally models the effects of beam divergence and compared it with the results of the approximated simulation (**Figure 5.5**).

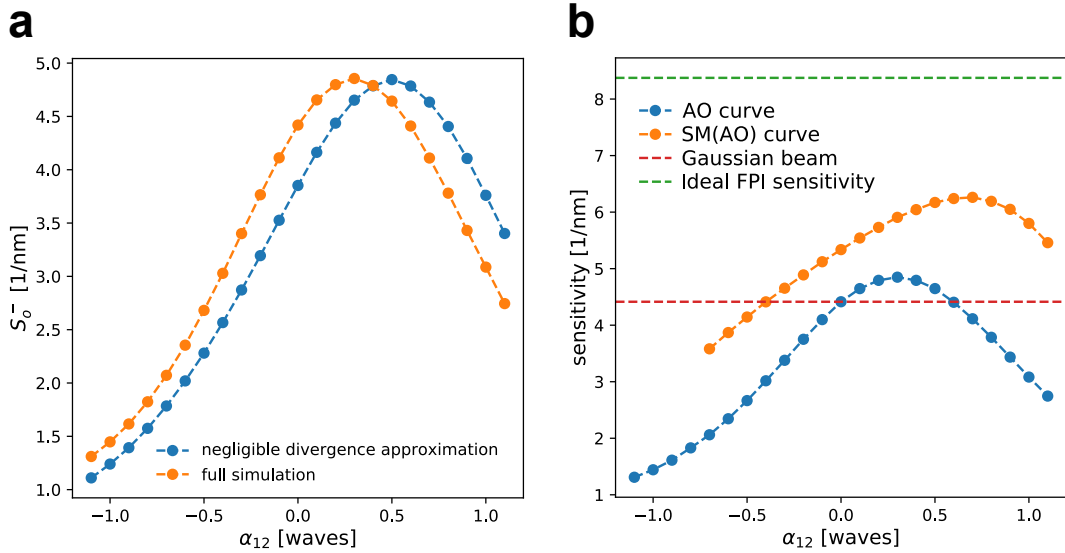


FIGURE 5.5: **Validation of the non-divergence approximation** **a)** Comparison between the simplified simulation from **Figure 5.4c** with a full simulation taking into account the changing beam diameter during propagation inside the cavity. **b)** Simulation of the effects of AO and SM on an aberrated cavity using the full simulation approach (for comparison see **Figure 5.6d**). Figure reproduced from: Czuchnowski and Prevedel, 2020.

Because the electric field E_k for reflection k can always be expressed as:

$$E_k(r, \phi, \lambda) = \sum_s c_s^k LG_s(r, \phi, z_k, \lambda), \quad (5.37)$$

where $s = (|l| + p)^2 + l + |l| + p$, we can consider the electric field E_k as a vector in a vector space with LG-modes as an orthonormal base $\{\mathbf{e}_s = LG_s(r, \phi, z_k, \lambda)\}$ and c_s^k as coefficients:

$$\mathbf{E}_k = \sum_s c_s^k \mathbf{e}_s \quad (5.38)$$

This allows us to define an algebraic operator (\mathbb{M}) that describes the mode evolution of the beam inside the cavity:

$$\mathbf{E}_k = \mathbb{M}\mathbf{E}_{k-1} \quad (5.39)$$

or, in terms of coefficients:

$$c_s^k = \sum_{s'} \mathbb{M}_{ss'} c_{s'}^{k-1} \quad (5.40)$$

We calculate the operator elements $\mathbb{M}_{ss'}$ by determining the cross-coupling between all LG modes and their aberrated counterparts:

$$\mathbb{M}_{ss'} = \iint_A LG_s(r, \phi, z_0, \lambda)^* LG_{s'}^{\mathcal{M}}(r, \phi, z_0, \lambda) dA \quad (5.41)$$

where $LG_s^{\mathcal{M}}(r, \phi, z_0, \lambda)$ is the mirror aberrated LG mode:

$$LG_s^{\mathcal{M}}(r, \phi, z_0, \lambda) = LG_s(r, \phi, z_0, \lambda) \exp(2\pi i \mathcal{M}(r, \phi, \lambda)). \quad (5.42)$$

One can then use **Equation 5.35** to calculate the fields required for **Equation 5.3**. The initial mode decomposition of the beam c_s^0 needs to be calculated from the input field:

$$c_s^0 = \iint_A LG_s(r, \phi, z_0, \lambda)^* G_a(r, \phi, z_0, \lambda) \exp(2\pi i \mathcal{M}(r, \phi)) dA \quad (5.43)$$

where G_a can be an aberrated beam from **Equation 5.11** or a non-aberrated beam by setting $\sum |\alpha_j| = 0$. This simplifies the calculations of the amplitude coefficients c_s^k coupled into mode LG_s and speeds up determining the interfering electric field $E_{FPI}^{\mathcal{M}}(r, \phi, \lambda)$ (that can be calculated according to **Equation 5.35**).

Cavity aberrations have important properties that set them apart from beam aberrations when considering active aberration correction (*adaptive optics*, AO). Because experimental AO methods only allow wavefront control at a single chosen plane along the optical axis at any given moment, it is not possible to fully correct cavity aberrations as they evolve and strengthen with subsequent reflections (**Figure 5.4a**). Thus, it is important to explore to which extent cavity aberrations can be corrected. In particular, *in silico* AO experiments for various cavity deformations can be performed by establishing an appropriate simulation pipeline (**Figure 5.4b**). Here the AO correction is simulated by applying Z-modes with amplitudes $\alpha_j \in [-1, 1]$ to the illuminating beam. Utilizing this simulation routine, the capability of individual Z-modes to correct a given cavity deformation is investigated (**Figure 5.4c**).

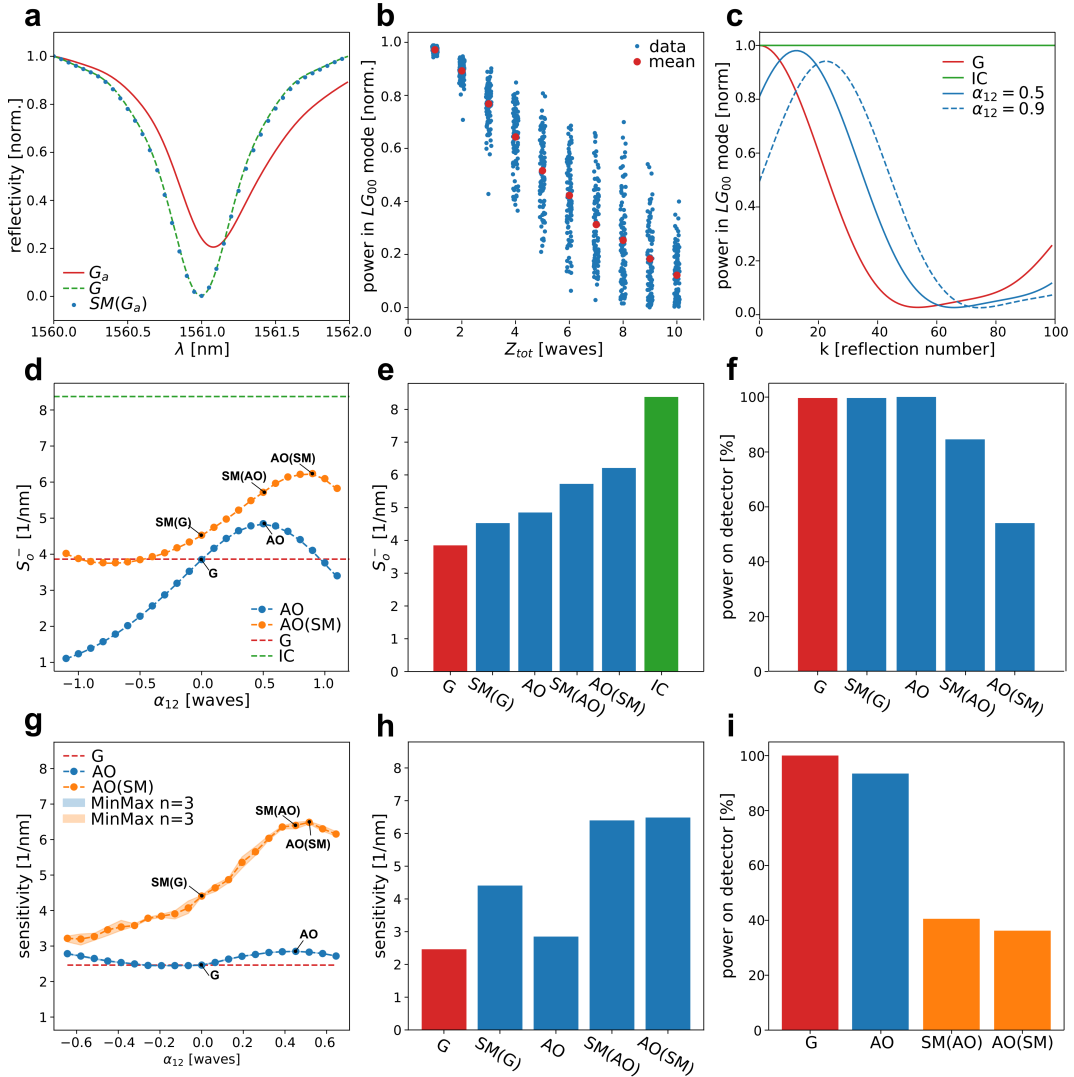


FIGURE 5.6: Characterization of FPI sensitivity improvement using active and passive aberration correction **a**) Exemplary plot showing the simulated effects of mode filtering on the transfer function of the FPI. G_a - Aberrated Gaussian beam, G - ideal Gaussian beam, $SM(G_a)$ - mode filtered aberrated Gaussian beam. **b**) Dependence of the power contained in the fundamental mode (LG_{00}) on the total aberration (Z_{tot}). For large aberrations passive AO rejects significant portions of the light. **c**) Dependence of power contained in the fundamental LG_{00} mode on the reflection number k inside the FPI. **d**) Simulation of AO correction using mode Z12 comparing the correction with and without mode filtering. Cavity parameters: $w_0 = 50 \mu m$, $l_0 = 20 \mu m$, $R_{1/2} = 0.95$, $\gamma_{12} = 0.2$ **e**) Comparison of the 5 characteristic points from **d**, showing that AO on fiber-coupled detection achieves highest sensitivity. **f**) Comparison of theoretical power on the detector for different AO methods. Combination of AO and SM leads to considerable power loss. **g**) Experimental AO correction using mode Z12 with and without additional mode filtering. Cavity parameters: $w_0 \sim 50 \mu m$, $l_0 \sim 22 \mu m$, $R_{1/2} \sim 0.98$, γ -unknown. **h**) Comparison of the 5 characteristic points from **g**. Combinations of AO and SM can increase sensitivity almost three-fold. **i**) Comparison of experimentally measured power on the detector for different AO methods. $SM(AO)$ and $AO(SM)$ are normalised to the fibre coupled power at $\alpha_{12} = 0.0$ to disentangle the experimental power loss due to fibre coupling. G - Gaussian beam, IC - ideal cavity, AO - AO corrected beam, $SM(G)$ - mode filtered Gaussian beam, $SM(AO)$ - mode filtered AO corrected beam, $AO(SM)$ - AO correction performed while mode filtering. Figure reproduced from: Czuchnowski and Prevedel, 2020.

We found that more than a single Z-mode can interact with the cavity, even when the cavity is deformed using only a single Zernike polynomial. This led to the observation that e.g. γ_{12} can be corrected by Z4, Z12 as well as Z24 (**Figure 5.4d**). We explored this in a more rigorous fashion and revealed that Z-modes within the same ‘family of aberrations’ have the ability to partially compensate each other (**Figure 5.4e**). Furthermore, when combined, they can act synergistically further improving the FPI sensitivity (**Figure 5.4d**). This finding has interesting general implications for AO that are further explored in **Appendix A**.

5.1.4 Active and passive aberration correction in FPI systems

Beam aberrations

We can now proceed to explore potential approaches for correcting both beam as well as cavity aberrations. Typically, beam aberrations in light microscopy are addressed with the use of active optical elements (such as deformable mirrors [DMs] or spatial light modulators [SLMs]) which can apply spatially varying, well defined phase delays. However, simulations also allow to hypothesize that a much simpler approach could in principle be effective. Since the loss of sensitivity is caused mainly by leakage of power from the fundamental mode to higher-order cavity modes (**Figure 5.3f**), we speculated that sensitivity could be improved by so called laser mode filtering (e.g. by using a passive element such as a single mode fibre). This enables the rejection of all the reflected light that propagates outside the fundamental Gaussian mode (LG_{00}) before it reaches the detector.

This hypothesis can be tested both by simulations as well as experimentally. In the simulations the coupling of light power from the interfering field E_{FPI} into the fundamental Gaussian mode can be calculated:

$$I_{FPI}^{SM}(\lambda) = \left| \iint_A E_{FPI}(r, \phi, \lambda) * G(r, \phi, 0, \lambda) dA \right|^2 \quad (5.44)$$

This shows that a mode filtering approach has the same effect as active AO correction in recovering the ideal transfer function (**Figure 5.6a**), while is simpler to implement. The only disadvantage is that for large aberrations there can be a significant power loss induced through mode filtering (**Figure 5.6b**).

Cavity aberrations

It is important to state that similarly to the case of active correction, passive mode filtering will also not be fully effective in tackling the effects of cavity aberrations. The reason being that since the power distribution between the modes changes in-between reflections, the interference pattern even within the fundamental Gaussian mode will be distorted (**Figure 5.6c**). This stresses the importance of improving techniques for manufacturing cavities (to achieve high uniformity of thickness) as cavity deformations cannot be fully corrected and therefore lead to an potentially irreversible loss of sensitivity. One hypothetical possibility of tackling this loss is by employing techniques to actively alter the cavity structure locally. As some of such techniques are currently actively developed by Villringer et al., 2019; Chen, Chen, and Ma, 2020, it remains to be seen if they are capable to tackle cavity aberrations under experimental conditions.

The simulations show that both AO and single-mode filtering (SM) individually do improve sensitivity compared to the standard aberrated Gaussian case (**Figure**

5.6d,e). Contrary to beam aberrations, for cavity aberrations, AO and SM have different correction mechanisms which additionally can synergize with each other. Interestingly, if the AO correction is performed *while* the beam is being mode filtered one can achieve an even higher sensitivity improvement than by just mode filtering the AO corrected beam ($AO(SM) > SM(AO)$). The explanation for this is connected to the fact that for $AO(SM)$ only the fundamental mode is being optimized for amplitude and phase distribution between reflections (as higher order modes are being rejected). This results in a different overall correction as compared to optimizing reflections for all LG modes (higher modes included) in case of AO. However, combining both passive and active aberration correction at the same time can lead to rejection of significant amounts of light, which may prove prohibitive for some applications (**Figure 5.6f**).

Experimental validation

To validate the theoretical findings we performed experiments using an all-optical photoacoustic tomography setup based on a FP sensor. The design of the system conceptually follows the one in **Figure 3.3a**, but was modified by the addition of an adaptive optics module (**Figure 5.7a**) consisting of a deformable mirror conjugated to the back focal plane (BFP) of the scan lens.

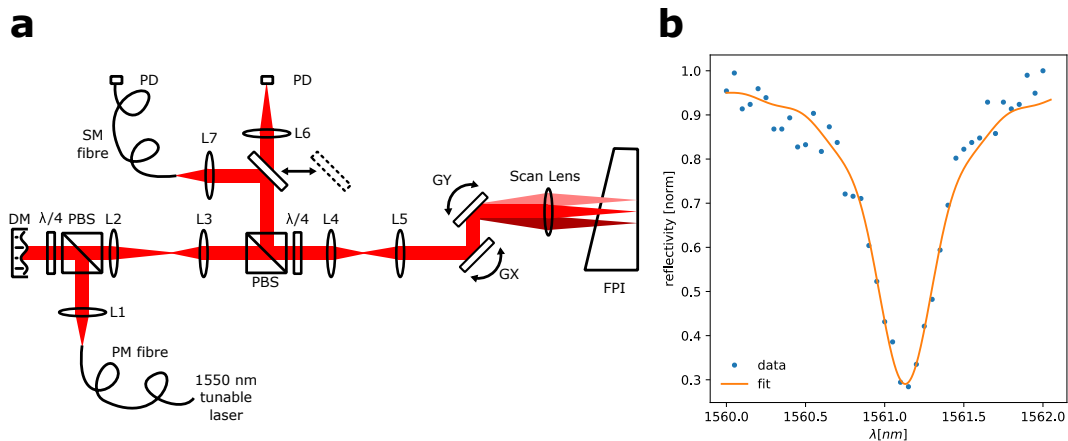


FIGURE 5.7: Experimental validation scheme a) Schematics of the experimental setup. **L1** - collimates the output of the interrogation laser's fiber to match the diameter of the active aperture of the deformable mirror (**DM**, DMP40/M-P01, Thorlabs). Two optical relays (**L2-L3** and **L4-L5**) then reduce the beam diameter appropriately to achieve $\sim 50 \mu\text{m}$ spot radius on the Fabry-Pérot Interferometer (**FPI**). **GX**, **GY** - galvanometric mirrors, **PD** - photodiode, **PBS** - polarising beamsplitter, $\lambda/4$ - quarter-wave plate, **PM fibre** - polarisation-maintaining fibre, **SM fibre** - single-mode fibre. **b)** Exemplary data of an experimental, mode filtered ITF, showing good agreement between experimental data points and respective fit from which the optical sensitivity is inferred). Figure reproduced from: Czuchnowski and Prevedel, 2020.

First, the output of the interrogation laser is collimated to a beam diameter that matches the size of the active aperture ($\sim 10 \text{ mm}$) of the deformable mirror (**DM**, DMP40/M-P01, Thorlabs). Two relays (**L2-L3** and **L4-L5**) then reduce the beam diameter by 0.6x and 0.625x, respectively, to match the appropriate NA for the scan lens (TSL-1550-15-80, Wavelength Opto-Electronic) to achieve a $\sim 100 \mu\text{m}$ spot diameter on the Fabry-Pérot Interferometer (**FPI**). The back-reflected interrogation light is then redirected by a quarter-waveplate ($\lambda/4$) and polarising beamsplitter (**PBS**) to the detection arm and then either focused, or fiber coupled into a single-mode fibre, before being detected by a photodiode (**PD**, PDA05CF2, Thorlabs). The DM used

was factory-precalibrated to display Zernike aberrations 3 to 15. The FPI transfer function (ITF - **Equation 4.5**, **Figure 5.7b**) is acquired by setting a particular Zernike mode phase pattern on the DM and then tuning the wavelength of the laser in a stepwise manner (in order to avoid spectra deformation connected to wavelength sweeping).

For accurate estimation of the FPI sensitivity, the ITF data is fitted numerically, using a simulation of a Gaussian beam propagating in an ideal cavity and varying the reflectivity of the two mirrors (R_1, R_2 - **Figure 5.7b**). The fitting approach by (Varu, 2014) showed good performance and can be computed efficiently for the purpose of this application. However it is still significantly slower than the Pseudo-Voigt fitting approach described in **Section 4.1.2**.

It is important to note that (contrary to the simulations) in the experiments both the exact beam (α_j) as well as cavity (γ_j) aberrations remain unknown and therefore prevent precise modeling of the experimental situation. Nonetheless, qualitative comparisons can be made to gain intuitive insights into the system. The experiments show that mode filtering does indeed increase the sensitivity compared to performing adaptive optics only, which stands in agreement with the simulations (**Figure 5.6g**). Furthermore the characteristic points of the curves also show similarities, with the relative sensitivity improvements being mostly conserved $AO(SM) > SM(AO) > AO/SM(G) > G$ (**Figure 5.6h**). There is one small difference to the simulation ($AO < SM(G)$). However, this may be due to contributions from other cavity and beam aberrations which are not experimentally characterised, as mentioned above. Further, the full simulation incorporating the effects of beam divergence on the coupling coefficients also hints towards $AO < SM(G)$ (**Figure 5.5b**). Finally, the experimental power loss of various AO approaches also show qualitative agreements with the simulations (i.e. $AO(SM) < SM(AO) < G$, see **Figure 5.6i**). It is important to note that $SM(AO)$ and $AO(SM)$ are normalised to the power coupled at $\alpha_{12} = 0.0$ ($SM(G)$) to remove the effect of the experimental power loss due to fibre coupling **Figure 5.6i**.

5.1.5 Discussion

This chapter introduced a theoretical framework for understanding the effects of both beam as well as cavity aberrations on the sensitivity of the FPI pressure sensor. Based on the theoretical framework, I predicted possible approaches for tackling the aberration-induced loss of sensitivity and validated them experimentally. One unexpected and interesting finding of this chapter is the fact that mode filtering can lead to significant gains in optical sensitivity. This can impact practical realizations of FPI-PAT systems because of the simplicity of implementation. The only disadvantage of this approach lies in the fact that, depending on the nature of the aberrations, a large portion of the interrogating laser light might be rejected thus leading to lowered SNR due to shot noise contributions. Furthermore, we showed that in more experimentally realistic cases when both cavity and beam aberrations are present, combining both active and passive approaches yields the best overall improvements in optical sensitivity (**Figure 5.6e,h**). Here, because the power loss of the passive filtering might be limiting, the optimal solution may not only depend on the increase in sensitivity, but also on the effects of the reduced power one signal-to-noise of the measurement. Consequently, a more complex optimisation metric which takes into account these additional considerations might be required.

An insight of this work with much broader applicability and potential impact is the theoretical observation that higher order aberrations can actually be partially corrected by lower order modes (e.g. Z_4 can correct γ_{12} , more on this topic in **Appendix A**). This has important practical implications since it might allow the use active optical elements such as DMs with lower number of degrees of freedom. This would greatly reduce both the cost as well as technical complexity (and required characterisation time) of experimental AO correction, and thus might lead to a broadened uptake of AO in the imaging field.

5.2 Applying Adaptive optics enhancement in photoacoustic tomography

As discussed in the previous section proof-of-principle demonstrations showed that the aberration-induced loss of optical sensitivity can be partially compensated by the use of optical aberration correction approaches based on Adaptive Optics (AO) (Czuchnowski and Prevedel, 2020, **Figure 5.8a**). That section, however, focused on theoretical aspects of the interactions between optical aberrations and the FP cavity. The experimental validation was limited to point-wise measurements of the interferometers sensitivity. In particular, it did not attempt to specify to which extent AO can be used in practical imaging settings to improve the quality of the detected PA signals and PA images.

This section investigates the requirements for AO-enhanced photoacoustic tomography in realistic PAT imaging systems. Specifically, it discusses how AO-induced focal spot shifts can be experimentally tracked and corrected. This is crucial for correct spatial sampling of the photoacoustic field over the entire FPI field-of-view which is important for high-resolution 3D image reconstruction. Additionally, shift-correction ensures optimal convergence of the indirect AO optimisation routine. This newly developed routine is shown to achieve significant improvements in the FPI optical sensitivity and photacoustic signal level.

5.2.1 Correction of DM induced focal shifts

Optical aberrations in laser beams manifest as deviations from the ideal Gaussian profile (phase or amplitude) of the beam and are induced either by imperfections in the optical elements or their alignment. These deviations were recently shown to be correctable with the use of active optical elements such as deformable mirrors (DMs, **Figure 5.8b**) which can be calibrated in the so-called Zernike mode basis, providing a convenient approach for experimental AO correction (**Figure 5.8c**). Ensuring that the profile of the beam matches the local FPI cavity shape can lead to significant improvements in the local optical sensitivity (**Figure 5.8d**). This observation is also in line with our earlier theoretical work (previous section, see also Czuchnowski and Prevedel, 2020).

One major challenge of using AO correction in PAT stems from the fact that the used corrections will effectively induce a lateral shift of the interrogating laser spot on the surface of the FPI dependent on the correction (Zernike) mode and amplitude (**Figure 5.8e**). These DM-induced shifts can be significant when compared to the laser spot radius for particular correction modes (**Figure 5.9a**). This results in two negative effects, which significantly reduce image quality in PAT. Firstly, lateral spot shifts deform the spacing of the scan grid which directly affects the image reconstruction algorithms (as most current image reconstruction methods assume a

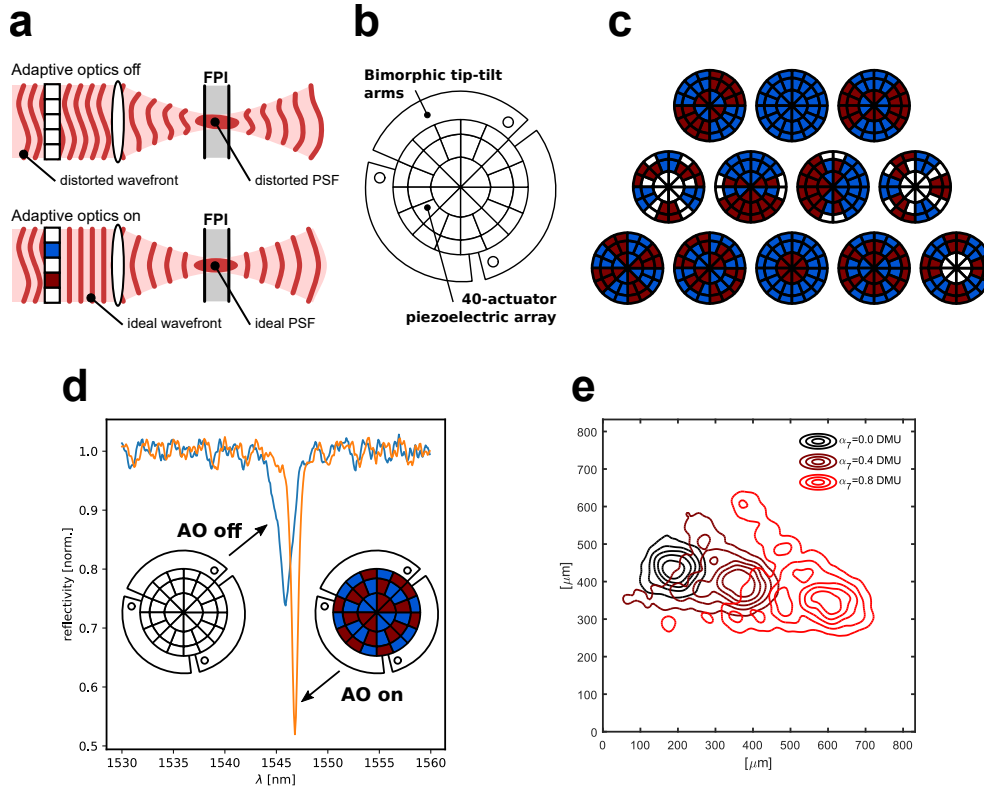


FIGURE 5.8: **Effects of Zernike modes on focal spot shift** a) Schematic illustrating the role of adaptive optics in optimizing the light coupling into the FPI cavity. b) Schematic of the deformable mirror used to correct the aberrated wavefronts via modulation of its 40 individual segments. c) Basic patterns displayed on the mirror recapitulating low order Zernike aberrations (Z3-Z14, top left to bottom right). d) Exemplary FP transfer function at the same sensor position with and without adaptive optics correction. e) Interrogation beam shape and positions measured on the sensor surface depend on the magnitude of the aberration displayed by the deformable mirror, here shown for coma aberration (Z7).
Figure reproduced from: Czuchnowski and Prevedel, 2021.

uniformly spaced grid; Treeby and Cox, 2010) and lowers the achieved spatial resolution. Secondly, since cavity imperfections are also spatially varying, this creates an undesired feedback into the AO optimization routine that can affect the algorithms convergence and lead to sub-optimal corrections. Tackling this problem requires careful characterization as well as compensation of these DM-induced focal shifts both during the AO correction characterisation as well as during the experiments. To achieve this, a novel hardware-based approach was developed, which is presented in the following section.

Predicting the spot drift

As a real-time measurement of the spot drift during AO correction is unpractical in realistic imaging conditions, a computational model to predict the shift based on the applied correction was developed. The model exploits the orthogonality of Zernike polynomials and assumes that their effect on the focal spot shift should be largely independent from each other (linear model (LIN), Figure 5.9b):

$$\vec{f}_{shift}(\sum_j \alpha_j Z_j) = \sum_j \vec{f}_{shift}(\alpha_j Z_j) \quad (5.45)$$

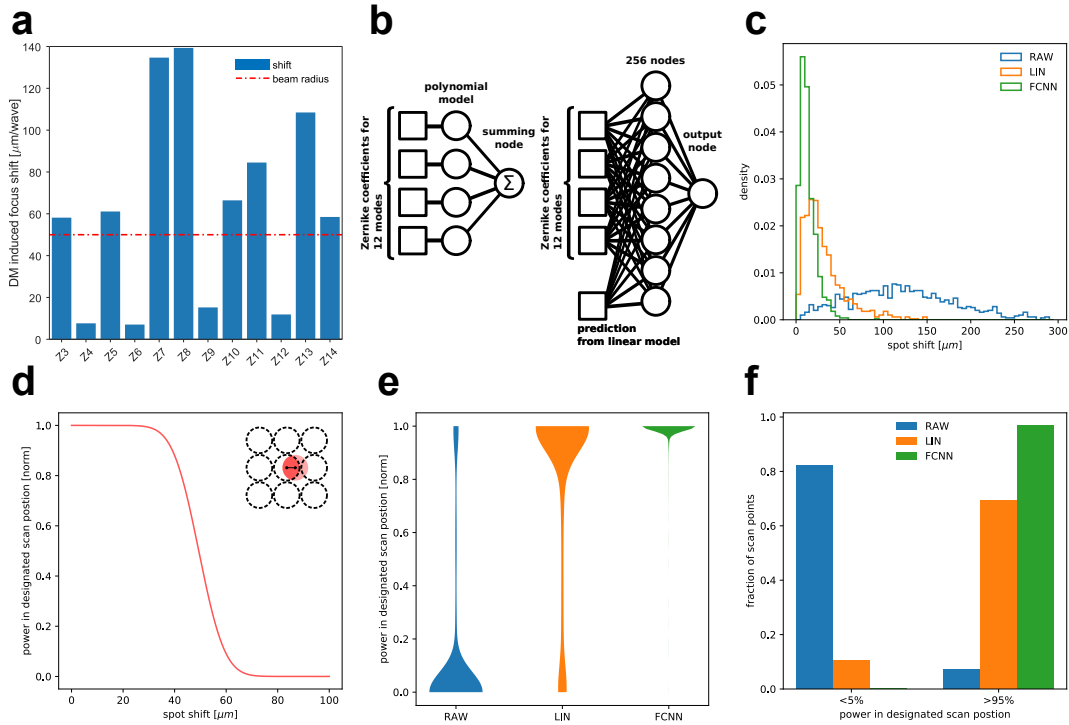


FIGURE 5.9: **Correcting the focal spot shift** **a)** Experimentally measured DM-induced focus shift for individual Z-modes. Several modes exhibit lateral spot shifts that are larger than the beam radius. **b)** Left: The linear model for shift prediction represented in a network convention. Right: The schematic of the fully connected neural network (FCNN) consisting of a single layer with 256 nodes. Here, the input consists of the 12 Zernike coefficients with the prediction from the linear model serving as a prior. **c)** Histogram of experimentally measured focal spot shifts for a randomly generated sets of aberrations $\max\{A_n^m\} = 0.2 DMU$. Here, using the linear model (LIN) as well as our neural network (FCNN) leads to significantly reduced spot shifts compared to the uncorrected case (RAW). **d)** Power contained within the designated scan position on the FPI dependent on the focal spot shift (see **Equation 5.47**). **e)** Violin plots visualising the loss of power from designated scan position (from **a**) induced by the DM shifts for the uncorrected case (RAW), and after correction based on LIN and FCNN models. **f)** Binning of data from **f** shows drastic differences in predicted performance between the corrected (LIN, FCNN) and uncorrected (RAW) use of the DM. Figure reproduced from: Czuchnowski and Prevedel, 2021.

This model can be realised experimentally by measuring the shift induced by isolated Zernike aberrations of varying amplitudes and fitting low order polynomials ($n=3$):

$$\vec{f}_{shift}^j(\alpha_j Z_j) = \left[\sum_{i=0}^n (\alpha_j)^i c_x^{j,i}, \sum_{i=0}^n (\alpha_j)^i c_y^{j,i} \right] \quad (5.46)$$

where α_j is the amplitude of the correction applied for mode Z_j and $(c_x^{j,i}, c_y^{j,i})$ are the parameters of the fit.

Compared to the uncorrected case (RAW), the linear model (LIN) strongly reduces the overall spot shift (**Figure 5.9c**). However, the shift itself is not a good indicator of the actual functional improvement gained by correcting the shift as it does not scale linearly with the predicted system performance. As for PAT proper spatial sampling of the acoustic field is crucial, an appropriate quality metric can be defined. Intuitively, it should be based on the optical power fraction contained in the desired scan position for different shift values:

$$P_{DSP}(\vec{f}_{shift}) = \frac{\int_{DSP} |G(\vec{f}_{shift})|^2}{\int_{\infty} |G(\vec{f}_{shift})|^2} \quad (5.47)$$

where, DSP is the Desired Scan Position and G is a Gaussian beam. For example for a $100 \mu\text{m}$ beam diameter and a $100 \mu\text{m}$ step size grid the result is a sigmoid displaying a rapid loss of contained power around $50 \mu\text{m}$ (Figure 5.9d).

This metric allows a quantitative evaluation of the effects of DM-induced drift and the comparison of different correction approaches (Figure 5.9e). It can be observed that for weaker aberrations (i.e. $DMU < 0.1$) the linear model is sufficient to correct the effects of the drift (Figure 5.10e, f). However, for stronger aberrations (i.e. $DMU > 0.1$) a large fraction of points exhibiting a signification power loss can be observed (Figure 5.10a, b).

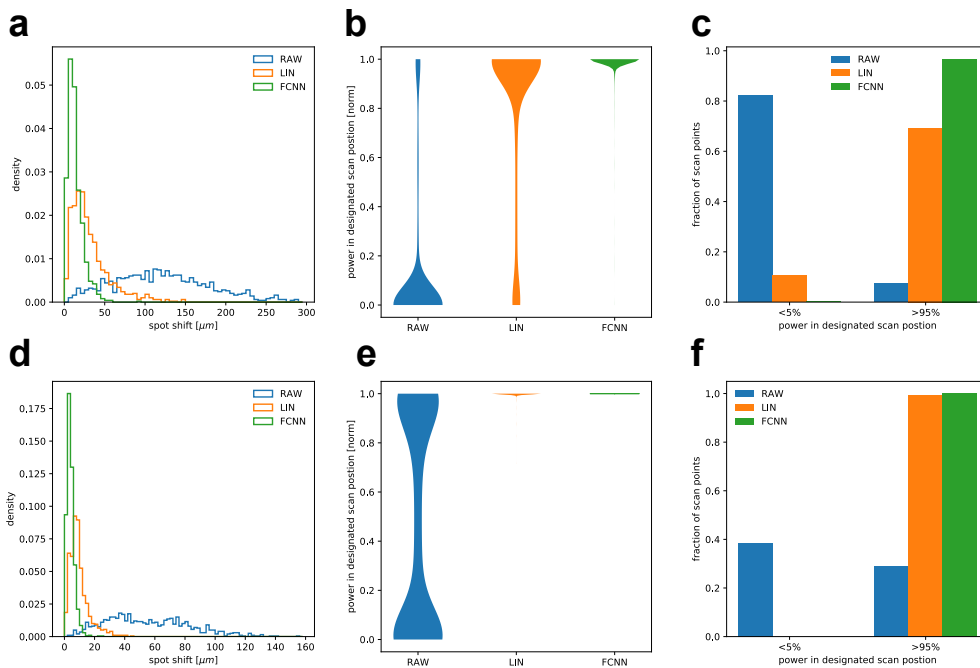


FIGURE 5.10: **Comparison of focal shift corrections** Panels **a,b,c** are replotted from Figure 5.9 for side-by-side comparison ($\max\{A_n^m\} = 0.2 DMU$). Panels **d,e,f** are analogs of panels **a,b,c** respectively, but gathered for aberrations where $\max\{A_n^m\} = 0.1 DMU$. Figure reproduced from: Czuchnowski and Prevedel, 2021.

The shortcomings of the linear algorithm can be attributed to the assumption of Z-mode independence that breaks for stronger aberrations, presumably due to the imperfections in how the DM displays the Z-modes. To address this limitation, a more complex model based on fully connected neural networks (FCNNs) can be developed that can account for mode interactions in an agnostic, data driven way (Figure 5.9b). This FCNN can efficiently learn cross-interactions between the low order Zernike modes (Z3-Z14) from a moderate data size of 5000 random aberrations if provided with a prior (the linear model prediction). Due to the ability to predict Z-mode interactions the FCNN outperforms the linear model in both the strong and weak aberration regimes (Figure 5.10a, d). Moreover, even in case of strong aberrations it can limit the power losses in the desired scan grid to below 5% in over 96% of scan positions (Figure 5.9f).

5.2.2 Indirect wavefront sensing with iterative refinement

With the shift correction scheme ready the use of the adaptive optic routines for FPI sensing can be explored. In this particular case an **indirect** wavefront sensing approach (in which the sensitivity of the system is directly optimized via iterative improvement) is superior to using a **direct** wavefront sensing approach (Ji, 2017; Booth, 2014) because of several reasons. **Direct** wavefront sensing in the FPI case is not only challenging in its technical implementation, but also requires a complex modeling approach to relate the observed wavefront distortions to changes in sensitivity (because of the non-trivial interactions between beam and cavity aberrations in FP interferometers; Czuchnowski and Prevedel, 2020).

Aberrations present in the FPI-PAT system come predominantly from two sources: **(1)** Beam aberrations (that are assumed to be **weakly** varying between scan positions on the FPI) and **(2)** cavity aberrations (that are assumed to be **strongly** varying between scan positions on the FPI). Therefore the effective aberrations present in the system can be expected to vary significantly between scan positions on the FPI. This presents a large experimental challenge to this approach as characterising the entire FPI field-of-view in a point-by-point manner requires an impractically long optimization time. This is because for an iterative AO optimization where 12 Zernike modes are used, each iteration takes ≈ 30 s per scan position which translates to ≈ 80 hours for the whole field-of-view (10^4 scan positions). In practice, this would extend even further as multiple iterations (2-3) over the same Z-modes are required to compensate for cross coupling between Z-modes (see **Appendix A** for more details).

However, since the overall aberrations consist partially of beam aberrations (which are expected to vary weakly) a certain extent of spatial correlation between neighbouring scan positions can be assumed. Capitalising on this, a sub-sampling scheme can be developed that drastically reduces the overall characterisation time while still significantly improving the FPI sensitivity over the whole field-of-view. We hypothesised that the same AO correction can cause a sensitivity improvement in the neighbourhood of the point on which the characterisation was performed (reminiscent of the 'isoplanatic patch' concept in AO corrected microscopy). To test this hypothesis we divided the whole 99×99 point scan grid into 9×9 regions, and applied the measured AO correction of the center point to the entire region. This approach has the advantage of reducing the required characterisation time by two orders of magnitude (to within one hour). A significant improvement of the sensitivity can be observed (**Figure 5.11a,b**) for almost all the FPI positions as can be seen by pairwise plotting of the sensitivity values for all AO 'on' versus AO 'off' scan positions (**Figure 5.11c**). The magnitude of the improvement can be inferred from the plot as the vertical distance from the diagonal and visualises that the vast majority of scan points display a significant improvement in sensitivity.

As a result of the subsampling approach the surface of the interferometer is largely undersampled for calculating the AO correction. This makes it interesting to investigate to which extent the AO improvement could be refined through denser sampling which can be achieved either by using a denser grid in the initial step or by refining the corrections during a second round. We explored the latter option by randomly characterising points on the FPI which were left out during the first characterization and compared the AO-improvement achieved in a 9×9 region centered around this point with the previous AO-improvement. This allowed to update the correction where it yielded an improvement in sensitivity. This refinement approach, termed AO 'ref', allows a further enhancement of the effective sensitivity of

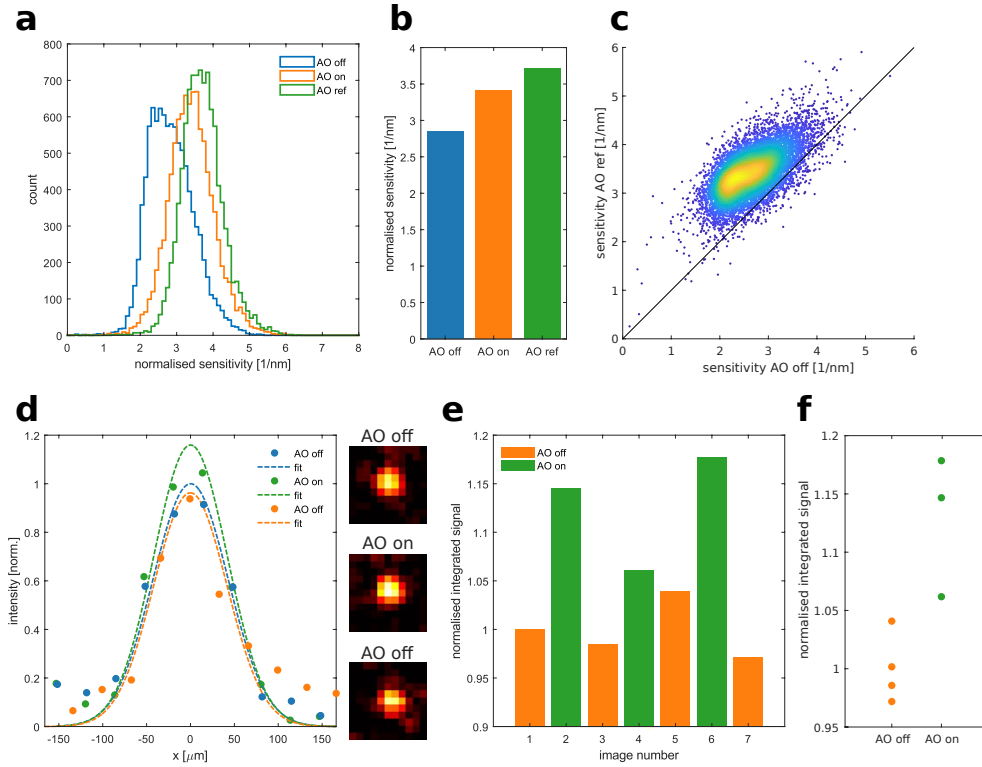


FIGURE 5.11: Characterisation of the AO improvement **a)** Histograms of the FP interferometer sensitivity between AO ‘off’ and AO ‘on’ conditions. AO ref refers to the ‘refined’ AO case. **b)** Mean sensitivity of the FP interferometer between AO ‘off’ and AO ‘on’ conditions. **c)** Pointwise correlation between the AO ‘off’ and AO ‘ref’ sensitivity for all the scan positions on the FPI. **d)** Experimentally measured cross-sections of diffraction limited beads taken with the photoacoustic system with AO ‘off’, AO ‘on’ and AO ‘off’ again, respectively, showing improvement for the AO ‘on’ condition. Insets show images from which the cross-sections were taken. **e)** Integrated signal level for consecutive bead images taken while alternating between AO ‘off’ and AO ‘on’ conditions, showing consistently higher signal levels for AO ‘on’. **f)** Dot plot for data shown in **e)**. The images of the beads were corrected for bleaching prior to quantification by fitting an exponential decay curve to the AO ‘off’ conditions and normalising the intensities. Figure reproduced from: Czuchnowski and Prevedel, 2021.

the interferometer in an iterative fashion (**Figure 5.48**) and achieves a higher sensitivity improvement than the standard AO ‘on’ condition (**Figure 5.11a,b**). This iterative refinement leads to an overall increase in (mean) sensor sensitivity with additionally refined scan positions, which can be described by a saturating function inspired by the Michaelis-Menten equation (**Figure 5.48**):

$$S_o(n) = S_{max} \frac{n}{k_s + n} + S^0 \quad (5.48)$$

where, S_{max} is the maximum achievable sensitivity improvement, k_s is the iteration number at which the function reaches half of S_{max} , S^0 is the starting sensitivity and n is the number of additionally characterised points on the FPI. This allows the quantification of the sensitivity improvement versus time trade-off and informs choosing of an optimal stop condition. The results presented in this section were acquired using a refinement with additional 500 points (5% of the scan grid) which took ~ 8 h. More points were not refined as significant saturation could already be observed (**Figure 5.48**).

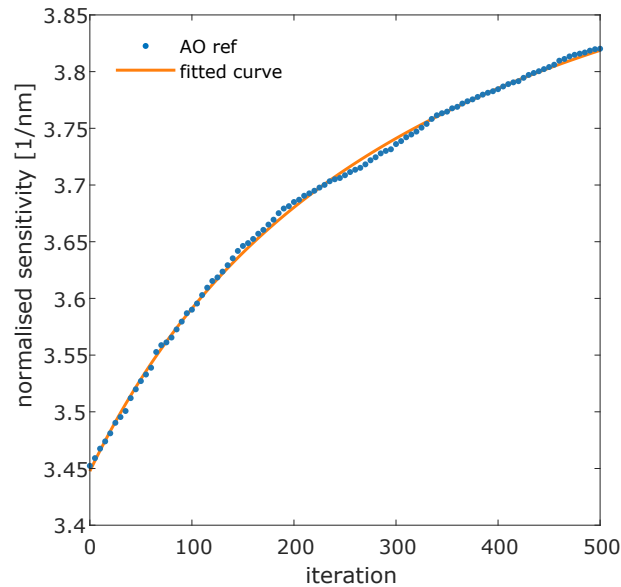


FIGURE 5.12: **Modeling the adaptive optic refinement with a saturating function** Iterative sensitivity improvement over the number of additionally characterised points using AO refinement and the fit with a saturating function (Equation 5.48). Figure reproduced from: Czuchnowski and Prevedel, 2021.

The improvement in sensitivity due to AO originates from an increased slope in the ITF of the FPI, however, as a result it also changes the whole ITF affecting the visibility and shifts the overall signal level. This change in the DC signal level effectively changes the working point of the photodetector, which goes in hand with the DC related noise sources (such as the relative intensity noise [RIN] and shot noise), therefore, affecting the overall sensitivity of the system. To account for this effect we developed a simple model which allowed to correct the input power of the PA system in order to equalize the working between the two conditions (Figure 5.13, for details see Section 4.1.4). This is important in order to maximise the effects of any improvements in coupling of light into the FPI due to the AO correction, and to ensure that they actually translate into improved overall sensitivity of PAT imaging.

5.2.3 Adaptive-optics enhanced photoacoustic imaging

To validate the potential of the described approach for improving PAT, imaging experiments were performed using resolution phantoms made of $10\ \mu\text{m}$ sized dye loaded beads (1010KB, Degradex[®]) embedded in 1% agarose. The improvement in signal level when using AO enhanced cavity coupling was quantified (Figure 5.11d) and we observed that the peak intensity of the reconstructed bead images increased when AO corrections were applied. To further ascertain that the observed improvement in sensitivity indeed originates from applying adaptive optics we performed sequential AO 'on' and 'off' imaging and observed a reproducible switching pattern showing a clear improvement whenever AO was turned 'on' (Figure 5.11e,f).

Next, the approach was applied to biological samples by performing *in vivo* label free imaging of blood (hemoglobin) in the abdominal area of anaesthetised mice. Using the AO correction scheme described in Section 5.2 we were able to show a significant improvement of PA signal level under realistic imaging conditions (Figure 5.14a). In particular, the AO correction led to a strong enhancement of signal level

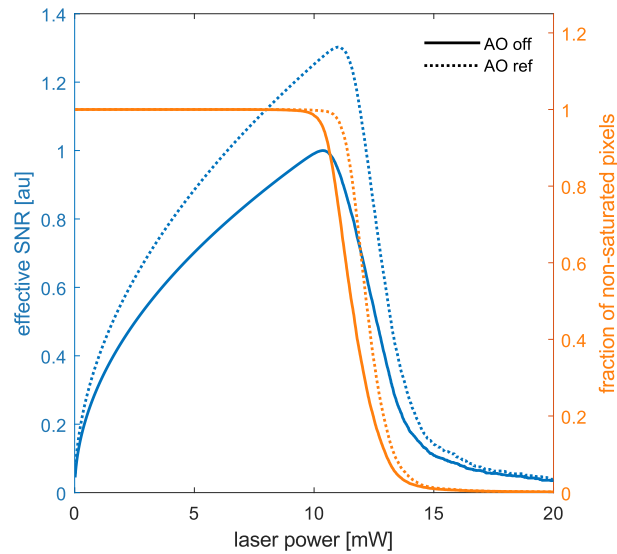


FIGURE 5.13: **Optimal working point characterisation for the AO system** Effective SNR as a function of interrogation laser power incident on the photodiode, comparing between the AO 'off' and AO 'ref' conditions as described by our model. Figure reproduced from: Czuchnowski and Prevedel, 2021.

in the typical PAT frequency band (1-20 MHz; **Figure 5.14b**), as quantified by calculating the power spectrum of the recorded PA signals. Integrating the power spectrum over this bandwidth shows a large 3-fold improvement in signal level concentrated in this band (**Figure 5.14c**). Due to the spatial heterogeneity of the FPI sensor used, some extent of spatial variation of the AO improvement is expected, causing stronger local enhancements of image quality. This can be seen by comparing sequentially taken PA images (**Figure 5.14d-f, top row**), where while global quality metrics only show a moderate improvement in image quality (**Figure 5.14g, top**), locally much larger improvements can be observed (**Figure 5.14d-g, bottom row**). However, this is expected given the spatial variation in the AO improvement measured across the FPI field-of-view.

5.2.4 Discussion

Section 5.2 described a new experimental paradigm that uses adaptive optics to enhance the sensitivity in all-optical photoacoustic tomography based on FPIs and allows to translate these improvements into practical imaging conditions. This can be achieved by a careful characterization of the influence of active wavefront shaping on the shift of the interrogating beam on the surface of the FPI sensor, and by actively adjusting the interrogating beam power on the photodetectors to ensure optimal SNR. Furthermore, the presented subsampling approach allows the characterization and iterative refinement of the AO corrections on a practical time-scale. Altogether, the described AO approach enables an enhancement in photoacoustic signal detection by up to 3.5-fold. Practically, this considerably improves image quality in *in-vivo* mouse PAT experiments.

It is important to highlight that the proposed use of AO in our PAT system significantly differs from its typical application in optical microscopy. In our case, AO is utilized to improve the sensitivity of the photoacoustic readout by adapting the beam profile to the local cavity structure. This, however, is contrary to the usual application of AO in microscopy where it is used predominantly to yield improvement

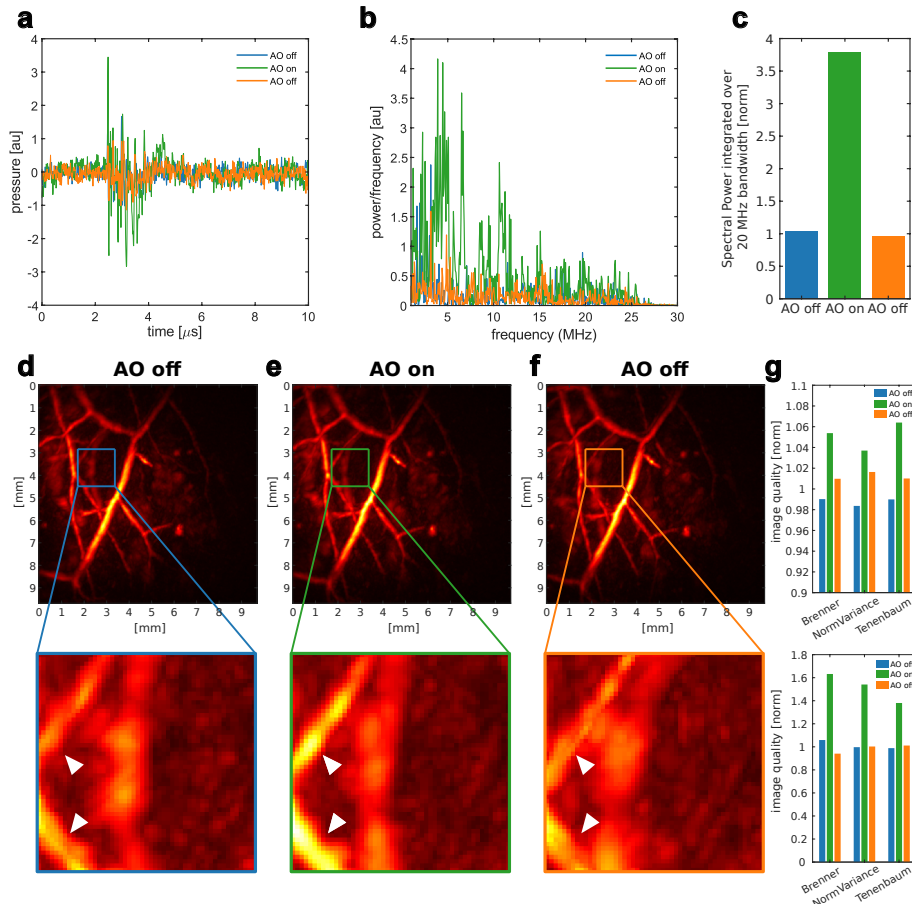


FIGURE 5.14: **Effects of AO correction on PA signals and images** **a)** Raw PA time traces from an *in-vivo* imaging experiment comparing signal level between AO 'off' and AO 'on' conditions. **b)** Power spectrum from time traces in panel (a) showing frequency enhancement in the 1 - 30 MHz band. **c)** Quantification of the overall increase in signal level in the 1 - 30 MHz band by integrating the power spectrum from panel (b). **d-f)** Maximum intensity projections of photoacoustic images of the abdominal part of the mouse taken at 600 nm showing label-free imaging of vasculature (**top**), as well as zoom-ins to regions that show especially good image quality improvement (**bottom, see arrows**). **g)** Commonly used image quality metrics calculated for images of the same area taken with AO 'off', AO 'on' and AO 'off' again, for both the whole images (**top**) and the zoomed in regions (**bottom**), respectively. Figure reproduced from: Czuchnowski and Prevedel, 2021.

in spatial resolution by recovering the ideal PSF shape. Recently, a computational PA wavefront correction technique was developed to address similar needs in PAT by tackling the problem of acoustic aberrations in photoacoustic image reconstruction (Cui et al., 2020).

While the experiments show significant improvements in both sensitivity and image quality, AO is incapable of restoring the theoretically possible maximum sensitivity of FPI sensors. **Section 5.1** discussed the potential (theoretical) reasons why a full recovery of optical sensitivity via AO is not attainable in realistic systems (see also Czuchnowski and Prevedel, 2020). To briefly recapitulate, cavity aberrations amplify the optical aberrations present in the interrogating beam while the beam is traveling within the FPI cavity. To completely correct these would require controlling the phase of the beam simultaneously at multiple focal planes (corresponding to subsequent reflections inside the FPI) which is not possible as the phase evolution

is controlled by the wave equation (which is to say that the phase profiles are at various focal planes are interdependent). Unfortunately, this limits AO to only partially correcting the effects of cavity aberrations.

The scope of these particular experiments was limited to lower order aberrations due to the low spatial resolution of the DM (40 active elements, only modes Z3-Z14). Utilizing active wavefront shaping devices with more active elements (such as spatial light modulators or SLMs) could allow to correct higher order aberrations and therefore further improve the sensitivity of the FPI.

Finally, it is important to note that **Section 5.2** also indirectly explores the area of wavefront shaping. As can be deduced from **Section 5.1**, because of the presence of cavity aberrations, the best beam profile to interrogate a deformed FPI cavity might not necessarily be a Gaussian beam. As a result, the iterative indirect wavefront sensing approach described in **Section 5.2** will possibly generate non-Gaussian beams that might more efficiently interact with particular local cavity shapes of the FPI. In this sense, this approach goes beyond classical aberration correction, where the aim is to restore a Gaussian beam profile. Unfortunately, as the DM employed in these particular experiments has only a limited number of degrees of freedom (40 active elements) it was impossible to explore more complex beam profiles (that are far from the fundamental Gaussian beam). Here again, the use of SLMs possessing thousands of degrees of freedom will allow to further explore this regime and study the effects of complex beam patterns on the sensitivity of the FPI.

5.3 Comparison of free-space and fibre-coupled detectors for FPI-PAT

The experimental implementation of AO correction for enhanced PAT sensitivity presented in the previous section is only one of two possibilities for improving the optical sensitivity of the FPI described by the theoretical framework introduced in **Section 5.1**. This section will discuss the alternative possibility, namely mode filtering of the back-reflected FPI light.

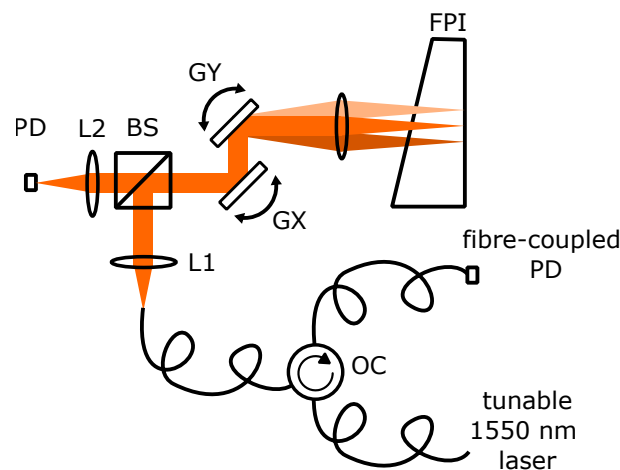


FIGURE 5.15: **Correlative free-space fiber-coupled setup** PD – photodiode; Lx – lens x; GX/Y – galvo mirror X/Y; BS – beam-splitter; OC – optical circulator; FPI – Fabry-Pérot interferometer

5.3.1 Correlative characterisation of the FPI

To characterise the effect of mode filtering across a large field of view of a realistic FPI ultrasound detector (5 mm x 5 mm), I designed a modified version of the setup that allowed for simultaneous characterisation of the setup using both a free-space and a fibre-coupled photodiode (**Figure 5.15**). This approach showed that (similarly to the simulations) an increase in overall FPI sensitivity is achievable via mode filtering (**Figure 5.16 left**). Practically, we observed this increase to be on the order of $\sim 37\%$ (**Figure 5.16 middle**) which is similar to the increase observed in case of active AO. Moreover, points also show a high heterogeneity of improvement, with some points achieving even an over 2-fold improvement in sensitivity (**Figure 5.16 right**).

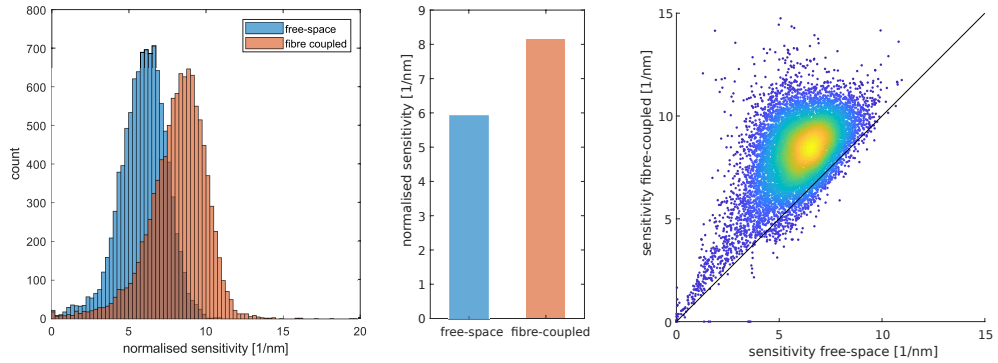


FIGURE 5.16: Comparison of the sensitivity across a FPI sensor between a fibre-coupled and free-space photodiode The histogram of sensitivity (left); mean value for the whole field of view (middle); point by point comparison (right).

Another interesting point is comparing the optimal wavelengths (λ_{opt}) between free-space and fibre-coupled conditions:

$$\Delta\lambda_{opt} = \lambda_{opt}^{fibre-coupled} - \lambda_{opt}^{free-space} \quad (5.49)$$

We see that λ_{opt} tends to shift towards shorter wavelengths after mode-filtering is employed ($\Delta\lambda_{opt}$ is on average = -6.6 ± 0.2 pm, **Figure 5.17**) which is in accordance to the predictions of our model in **Section 5.1** (**Figure 5.6a**).

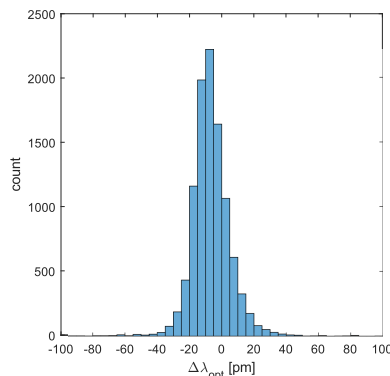


FIGURE 5.17: Shift of the optimal wavelength (λ_{opt}) between a fibre-coupled and a free-space photodiode

One of the challenges of employing mode-filtering are the experimental losses connected to coupling the back-reflected light into the single-mode fibre for a large scanning area on the FPI. In our experimental system this causes larger losses of

power on the edges of the field of view creating ‘uneven illumination’ effects which translate to a lower effective sensitivity. This loss of effective sensitivity can be understood by utilising the optimal working point model introduced in **Section 4.1.4**. By taking into account the uneven field illumination we can observe that the effective improvement in SNR drops from 37% to 24% (**Figure 5.18**). This can be tackled by a more complex design of the system that increases beam stability by conjugating the two galvo-mirrors or by evening the illumination of the FPI as described in **Section 4.1.4**.

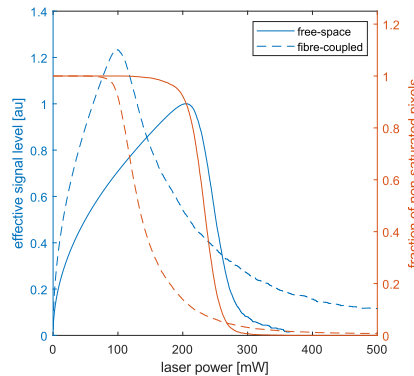


FIGURE 5.18: **Optimal working point comparison between a fibre-coupled and a free-space photodiode** Effective signal level is proportional to the SNR.

5.4 Reducing noise in FP-PAT

As fundamentally the data quality is not determined solely by the sensitivity itself, but by the SNR (see **Section 4.1.1**) an alternative strategy for effectively increasing the setups sensitivity is by lowering the measurement noise. There are multiple possible strategies for doing this, here we will discuss two of them: **Section 5.4.1** will discuss the hardware solution based on using passive signal amplification and high-saturation photodiodes, **Section 5.4.2** will discuss some software based solutions capitalising on the recent advances in the deep learning field.

5.4.1 Reducing electronic noise in photodiode detectors by passive signal amplification

As mentioned in **Section 4.1.1** the dominant sources of noise present in our setup are the shot-noise (N_{shot}) as well as the electronic noise of the detector ($N_{electronic}$). Shot noise is a fundamental physical limitation on the precision of a measurement and cannot be trivially overcome (although clever workarounds employing e.g. squeezed light exist [Loudon and Knight, 1987]) unless higher optical powers can be used. As the interrogation light does not come in contact with the biological sample the only limitations on the power come from: **(1)** the achievable laser power of the interrogation source; **(2)** the saturation power of the photodiode. **(1)** can be overcome with the use of a laser amplifier and **(2)** can be tackled by using biased photodiodes (BPDs) that have higher saturation limits (~ 10 mW) as opposed to amplified photodiodes (aPDs; ~ 1 mW).

There are however several challenges that need to be overcome. Laser amplifiers introduce additional noise which counteracts the gain in power. Fortunately this

can be tackled by the recently described digitally balanced detection that allows to suppress the optical noise to a limit close to that of shot noise ($N = \sqrt{2N_{shot}}$; Moon and Kim, 2007). Another problem is the fact that biased photodiodes do not provide strong enough signal amplification for the PA signal to be detectable with standard equipment (as the signal level at detector saturation is ≈ 0.5 V for a bPD [Equation 5.50] and ≈ 5 V for a standard aPD):

$$U = IR_{load} \sim P_{opt}R_{load} \approx 0.5V \text{ [at saturation]} \quad (5.50)$$

where U is the signal level expressed in Volts, I is the photocurrent expressed in Amperes, R_{load} is the load resistance in Ohms and P_{opt} is the optical power in Watts. A typical InGaS bPD has a saturation current of approximately 10 mA and uses a load resistance of 50 Ohm leading to a typical saturation voltage (U_{sat}) of 0.5 V. Theoretically, passive amplification using a large load resistance ($R_{load} = 500 \Omega$) could be used to increase the U_{sat} to 5 V typical for a aPD, however this would drastically reduce the bandwidth (f_{-3dB}) of the photodiode as $f_{-3dB} \sim 1/R_{load}$. There exists a solution to this problem capitalising on the existence of super-fast InGaS photodiodes used in telecommunication. These PDs have a low enough capacitance that they should theoretically be able to retain $f_{-3dB} > 20$ MHz for $R_{load} = 500 \Omega$. It is important to note that this solution also tackles the problem of the electronic noise of the measurement ($N_{electronic}$) which comes predominantly from active amplification.

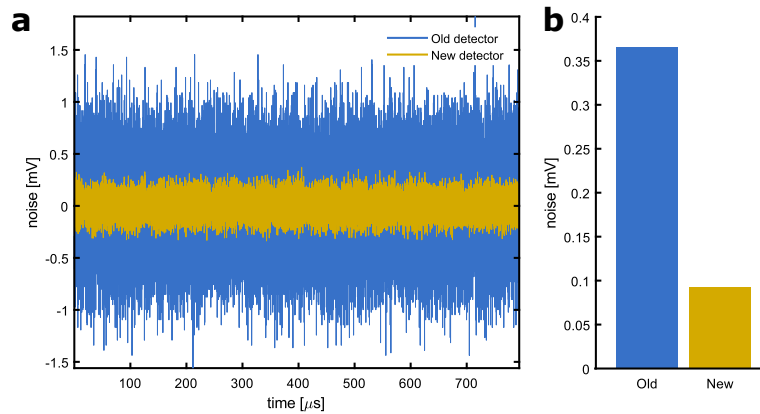


FIGURE 5.19: **Noise reduction using passive signal amplification** a) Time trace of system noise for both an actively amplified detector (old) and a passively amplified detector (new). b) Quantification of the noise expressed as the standard deviation of the time signal.

I have tested this hypothesis using a commercially available super-fast InGaS photodiode (DET08CL/M, Thorlabs) in combination with a laser amplifier and the digital balancing approach and found that this indeed allows for an over 3 fold reduction of the noise present in the system (Figure 5.19). Unfortunately the achieved bandwidth of the detector does not behave in accordance with the theoretical model suggesting the presence of parasitic capacitances which degrade the bandwidth. These parasitic contribution will need to be removed in the future to enable implementation of this detector into the PAT system.

5.4.2 Deep learning for signal denoising

Deep learning (Goodfellow et al., 2016; LeCun, Bengio, and Hinton, 2015) is a quickly evolving field which proved extremely powerful in both scientific as well as industrial applications. In the field of microscopy and image analysis, several advancements were made in the direction of signal and image denoising. In particular two approaches were developed which are potentially very interesting for photoacoustic imaging. One of them Noise2Noise (N2N, Lehtinen et al., 2018) is capable of removing noise from images by comparing two noisy images of the same object. As noise is stochastic in nature the noise pattern between two images differs and therefore the deep learning network is unable to learn the noise and actively removes it from the dataset in the process of training thus generating denoised images.

The second approach dubbed Noise2Void (N2V; Krull, Buchholz, and Jug, 2018) is a recently developed denoising algorithm that is even more minimalistic in its requirements. Just one set of noisy data is enough for training as the network uses a novel approach of trying to reconstruct the image pixel by pixel by having access always only to the pixels surrounding and not the actual pixel itself. This approach capitalises on lack of spatial coherence of noise contrasted with high spatial coherence of the sample signal.

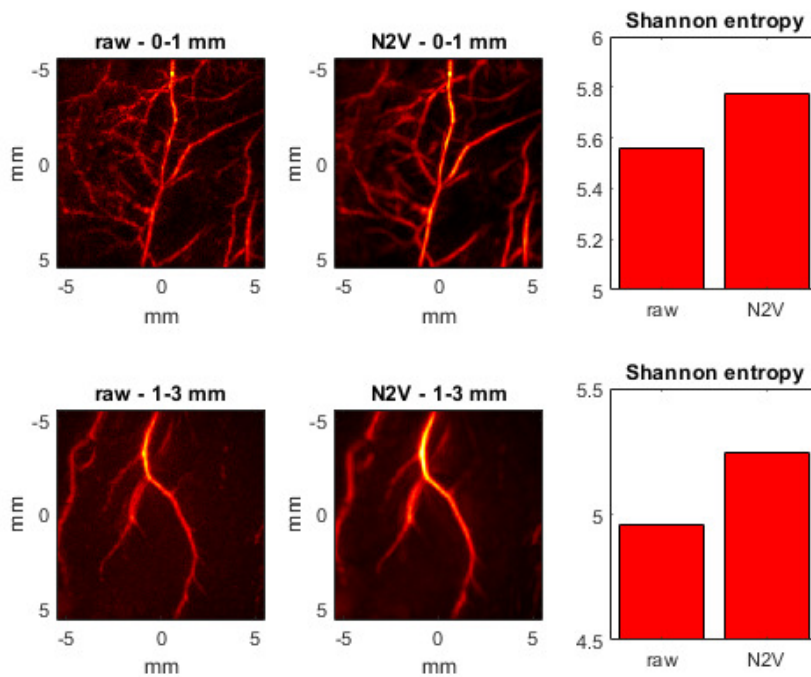


FIGURE 5.20: **PA signal denoising using N2V** Vasculature images reconstruction from raw data vs N2V denoised data showing significant denoising quantified by calculating the Shannon entropy of the images which is a metric of information content.

Both approaches have advantages and disadvantages in particular applications. For example, N2V requiring less data is preferential in situations where acquiring multiple images of the same object is challenging. However, it is incapable of removing noise displaying spatial coherence. N2N requires more data, but it might be more robust to noise displaying coherence provided that the noise pattern changes between acquisitions.

I have tested the available N2V implementation in Fiji to verify the capabilities of deep learning-based denoising of PA signals. In this implementation the raw PA data was treated as a 2D movie (xyt) of the acoustic field and denoised frame-by-frame by the 2D-N2V, afterwards 3D PA images were reconstructed from denoised raw data by using time-reversal (Treeby, Zhang, and Cox, 2010). N2V proved to be successful in denoising PA images which improved the information content of the reconstructed images (quantified by Shannon entropy), additionally a larger improvement in image quality was observed in deeper layers of the image as compared to the shallow layers (**Figure 5.20**).

5.4.3 Outlook

The preliminary results on noise reduction techniques shows great promise for increasing the SNR of available PAT systems as they have very broad applicability. In particular, because they can be combined with aberration correction approaches discussed in the previous sections to yield even larger increases in sensitivity. However, efforts to implement both of these approaches in working PAT systems are still underway and several challenges need to be addressed, including the possible bandwidth limitations of passively amplified photodiodes and the need to explore the best suited signal denoising approaches for PAT.

Chapter 6

Improving speed of Fabry-Pérot based photoacoustic systems

As calcium-imaging requires a high volume imaging rate (minimum 1 volume/s), it is crucial to improve the data acquisition speed of FP-PAT to achieve this limit. This is a challenging task as a full PA dataset consists of $\sim 10^4$ scan positions. In this chapter two separate strategies are discussed, one connected to trying overcome the imaging dead-time caused by the interrogation wavelength tuning to λ_{opt} and the second connected to parallellising the readout from the FP sensor by using optical multiplexing.

6.1 Tuning dependent dead-time

The spatial heterogeneity of the FPI cavity thickness requires changing of the λ_{opt} between scan positions to preserve optimal readout sensitivity from all points. While tuning, the system is unable to acquire data which generates a dead-time, limiting the achievable scan rate to 15 Hz (which limits the volume rate to ~ 1.8 mHz for a 100×100 px scan grid). To avoid this problem, two approaches are necessary: **(1)** binning the values of λ_{opt} to increase the number of point to be interrogated with a single wavelength **(2)** changing the scan pattern from a raster scan to a random-access scan, where all points within a binned group are accessed sequentially before moving on to the next binned group. These two solutions will be discussed below in **Sections 6.1.1** and **6.1.2**.

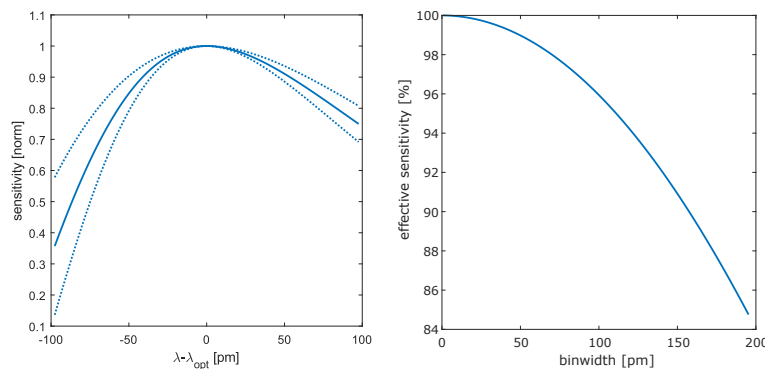


FIGURE 6.1: **Dependence of sensitivity on spectral distance from λ_{opt} (left)** Dependence of sensitivity on the detuning from the optimal wavelength for one FPI sensor. Full line - mean; dotted line - mean $\pm 2\sigma$ **(right)** Quantification of the effective sensitivity dependence on the bin width for the same sensor as in the left panel.

6.1.1 λ_{opt} binning

Binning the optimal wavelength poses the problem of choosing a proper bin width which has the inherent trade-off between absolute number of discrete wavelengths needed to interrogate the sensor and reduction of sensitivity for some points, where the used wavelength will be sub-optimal.

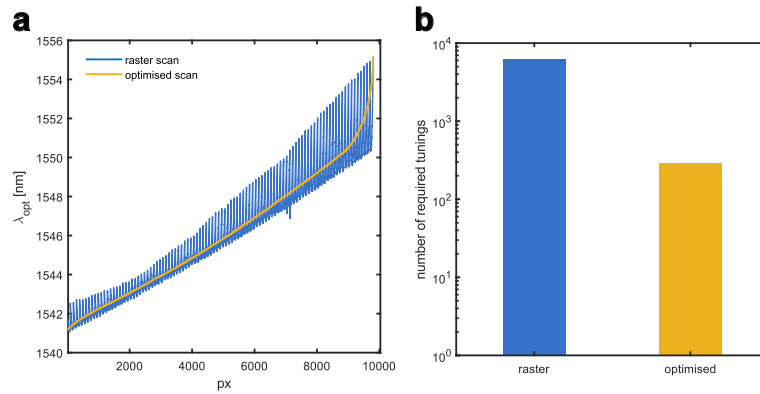


FIGURE 6.2: Wavelength sorting drastically reduces required number of tunings a) Values of λ_{opt} for subsequent scan positions along a raster scan and an optimised scan trajectory. b) Quantification of panel (a) showing a 22 fold reduction in the number of required tunings.

This loss of sensitivity is determined by the shape of the transfer function and can be characterised for each sensor (**Figure 6.1 left**). By binning these values and assuming an uniform distribution of λ_{opt} within each bin, the effective sensitivity trade-off with bin width can be predicted (**Figure 6.1 right**). It can be observed that even relatively large bins of 150 pm will only lead to 10% reduction of effective sensitivity which is very encouraging.

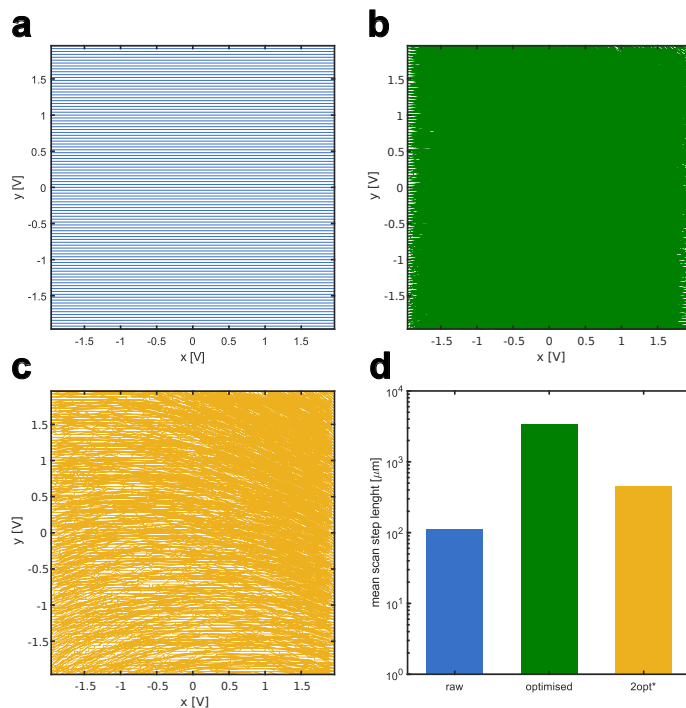


FIGURE 6.3: Optimisation of scan path Plots showing the scan trajectory expressed in the galvo-mirror voltage values for the: raster scan (a), optimised scan (b) and the 2opt* optimised scan (c). d. Quantification of the mean scan step length for all three trajectories.

We have chosen a bin width of 50 pm as an optimal number, because it is sufficient to achieve the desired increase in imaging speed. For a typical FP sensor this allows us to constrain the number of discrete wavelengths to 200-300 which theoretically reduces the dead time to only 2-3% (as we have 10.000 measurement points and only 200-300 tunings). Unfortunately, this also requires us to reshape the scan

trajectory as even with <300 discrete wavelengths the effective number of tunings can be significantly higher for a simple raster scan (**Figure 6.2**).

6.1.2 Optimising scan path length with the use of a modified 2opt algorithm

The drastic reduction of number of required tunings due to wavelength binning comes at a cost of severely distorting the scan grid (compare **Figure 6.3a** and **Figure 6.3b**) and increasing its effective length by ~ 30 fold (**Figure 6.3d**). This causes an erratic behaviour of the scanning system and introduces instabilities which severely affect the performance of the system.

The said increase is partially caused by the underlying spatial distribution of binned points (which cannot be altered) but also by the order at which these points are interrogated (which after the binning procedure is random). Thus the increase of scan path length can be partially tackled by changing the interrogation order of point within the binned groups to minimise the overall path length. As this problem is a variation of the well studied 'Traveling salesman problem' there exist a number of algorithmic methods for optimisation (Hoffman, Padberg, Rinaldi, et al., 2013; Flood, 1956).

Algorithm 1 2optSwap

```

1: procedure 2OPTSWAP(route, i, k)
2:   initialise new_route
3:   take route[0] to route[i - 1] and add them in order to new_route
4:   take route[i] to route[k] and add them in reverse order to new_route
5:   take route[k + 1] to end and add them in order to new_route
6:   return new_route
7: end procedure

```

Algorithm 2 2opt

```

1: procedure 2OPT(route)
2:   while improvement is made do
3:     best_distance = calculateTotalDistance(existing_route)
4:     for i ← 0 to number of nodes eligible to be swapped - 1 do
5:       for k ← i + 1 to number of nodes eligible to be swapped - 1 do
6:         new_route = 2optSwap(existing_route, i, k)
7:         new_distance = calculateTotalDistance(new_route)
8:         if distancenew < distancebest then
9:           existing_route = new_route
10:          best_distance = new_distance
11:         go to 3
12:       end if
13:     end for
14:   end while
15:   return existing_route
17: end procedure

```

▷ see Algorithm 1

In our application, there exists an additional constraint for time of optimisation as we need to perform it while the mouse is anaesthetised on the FP sensor. On the other hand, we do not need to achieve an optimal solution and only to significantly reduce the scan length which reduces the constraint on algorithm performance. Because of this, we chose the computationally most efficient 2opt algorithm (**Algorithm 2**, Watson et al., 1998) and further modified it to reduce computational

time at the expense of performance. We removed the feedback mechanism where after optimising a particular connection the algorithm loops back and again optimises all of the old connections reducing the computational complexity. Additionally, we changed the termination condition from convergence to a fixed number of iterations to ascertain a relatively constant computation time. This new 2opt* algorithm (**Algorithm 3**) is capable of reducing the length of the scan path by ~ 8 fold in ~ 30 s when running on a CPU under a Python implementation which we found to be acceptable for our application.

Algorithm 3 2opt*

```

1: procedure 2OPT*(route, iteration_limit)
2:   for iterations  $\leftarrow$  1 to iteration_limit do
3:     best_distance = calculateTotalDistance(existing_route)
4:     for i  $\leftarrow$  0 to number of nodes eligible to be swapped - 1 do
5:       for k  $\leftarrow$  i + 1 to number of nodes eligible to be swapped - 1 do
6:         new_route = 2optSwap(existing_route, i, k)            $\triangleright$  see Algorithm 1
7:         new_distance = calculateTotalDistance(new_route)
8:         if distancenew < distancebest then
9:           existing_route = new_route
10:          best_distance = new_distance
11:        end if
12:      end for
13:    end for
14:  end for
15:  return existing_route
16: end procedure

```

6.1.3 Validation of fast imaging

To validate the improvement in imaging speed phantom imaging experiments were performed using an agarose phantom with the embedded EMBL logo (**Figure 6.4**). The image showing 15 Hz data acquisition rate is the baseline when no trajectory optimisation is performed. Data acquisition is then limited by the laser tuning speed, effectively reducing the volume imaging rate to only 15% of the full capabilities (as the PRR of the excitation laser is set to 100 Hz). Performing trajectory optimisation (dubbed in the figure as 'software improvement') allows a large increase of the data acquisition rate to 88% of the PRR, by further changing the laser settings to allow faster scanning we can achieve an even higher rate of 96.5% of the PRR. The system was also tested with a 200 Hz PRR where the limit for the trajectory optimisation capped at around 131 Hz (or 65.5% of the PRR) or at 140 Hz (70% of the PRR) by including the fast laser settings. At this frequency the operating system (OS) performance actually starts to become a limiting factor and the overall performance can vary depending the OS status. Additional software solutions will need to be developed to ascertain optimal OS performance when attempting fast imaging experiments.

6.2 Optical multiplexing

Scan optimisation allows us to achieve pulse repetition rate (PRR) limited speed (for our excitation laser 200 Hz), however even this is not sufficient to allow calcium imaging in large volumes (a 100 x 100 px grid acquired at 200 Hz gives a 20 mHz volume rate). Since excitation lasers with higher PRR are not currently available, the

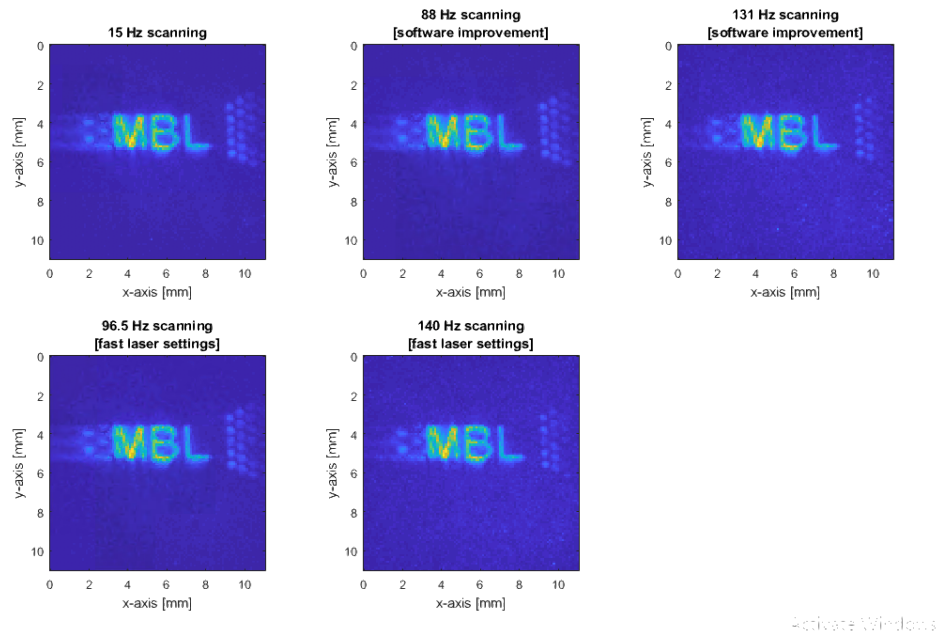


FIGURE 6.4: Validation of the trajectory optimisation scheme

alternative solution is to parallelise the readout from the interferometer with the use of optical multiplexing. Instead of reading out information from a single point we read out information from multiple scan positions at the same time.

6.2.1 Limitations of multiplexing

Optical multiplexing of FP-PAT systems can suffer from multiple limitations. On the hardware side, it requires acquisition of signals in the 20 MHz bandwidth over several tens of channels in parallel requiring multi-channel DAQ solutions that are not readily available commercially (see **Section 3.5** for details).

A more fundamental limitation comes from heterogeneity of cavity thickness. As multiple signals are read out in parallel using the same wavelength, the difference in λ_{opt} between all the simultaneously interrogated points needs to be small enough to facilitate efficient interrogation (**Figure 6.1 right**). This means that practically all the interrogated spots need to be within ~ 200 pm) to not deteriorate the effective sensitivity of the measurement.

6.2.2 Multibeam generation using a microlens array

Our initial idea of using an in-fibre beam splitter suffers from a few disadvantages. The less problematic one being: high price, susceptibility to damage and noticeable power loss. The more problematic and fundamental issue is that one is that a 1 to 46 beam splitter cannot be made in a single step and is built in a cascade fashion (a 1:3 combined with a 1:12 which also has an internal cascade structure). This, in turn, causes an exponentially decaying power uniformity between the beams causing a big variability in power between the beam which is detrimental to the measurement. That is why alternative solutions need to be explored.

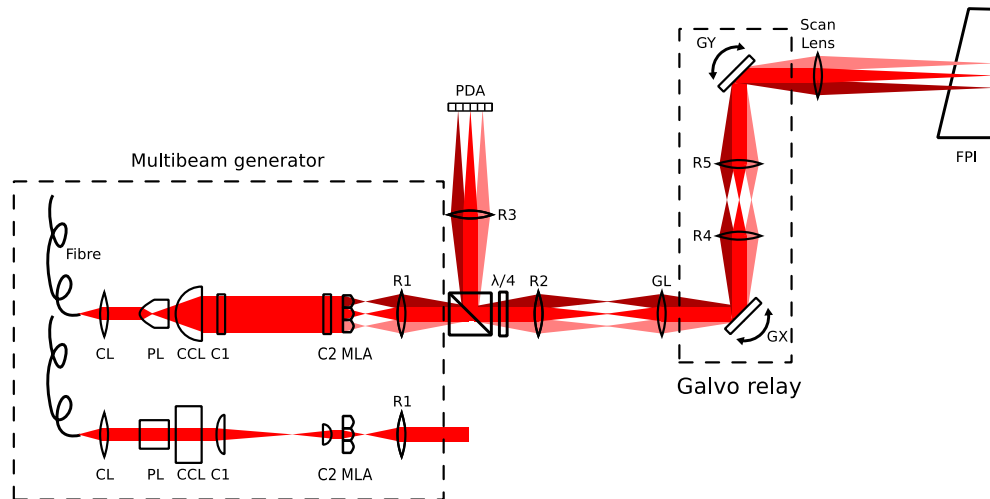


FIGURE 6.5: **Multibeam setup using a microlens array multibeam generator** R1-5 - relay lens, **PBS** - polarising beam splitter, **PDA** - photodiode array, **PL** - Powell lens, **CL** - Collimation lens, **CCL** - Cylindrical collimation lens, **C1-2** - Cylindrical lenses, **MLA** - Microlens array, **FPI** - Fabry-Perot Interferometer, **GX-GY** - Galvo mirrors.

One of the possibilities is to generate multiple beamlets by focusing light onto a single line of a spherical microlens array (MLA; or alternatively using a combination of cylindrical lens arrays). This, however, will also lead to power level heterogeneity as the envelope of these beamlets will have a Gaussian profile. To counteract this, the beam power needs to be homogenised along the line dimension prior to the MLA. Due to the requirement of high coherence for the interrogation light, some homogenising approaches (e.g. a Fly-eye condenser or an engineered diffuser) are unsuitable for this application leaving us with a field mapping approach. Here a special lens is used to generate a beam with a uniform intensity distribution (so called Powell lens). This beam is then reshaped to a thin and long light line which is next propagated through a single line of a microlens array (MLA) to generate a set of 46 parallel beams (Figure 6.5).

Multichannel readout using a laser line

Unfortunately, the use of microlens arrays strongly complicates the alignment of the whole system making it impractical to use. To simplify this problem, I explored an alternative approach where instead of several beams a laser line (or light-sheet) is used to interrogate the FPI. This simplifies tremendously both the optical design as well as the alignment. This solution is used in the initial implementation of the M-PAT (Figure 6.6).

6.2.3 Characterisation of the FPI using M-PACT

After developing the setup according to the design outlined in Figure 6.6, I performed validation experiments starting with the characterisation of the FPI sensor using all available 12-beams simultaneously. As the current setup lacks a homogeniser before lens C1, the intensity profile along the line is Gaussian; causing slightly lower signal levels for the edge beams. This effect can be compensated by fitting a low order polynomial ($n=4$) to the measured ITF to compensate both the

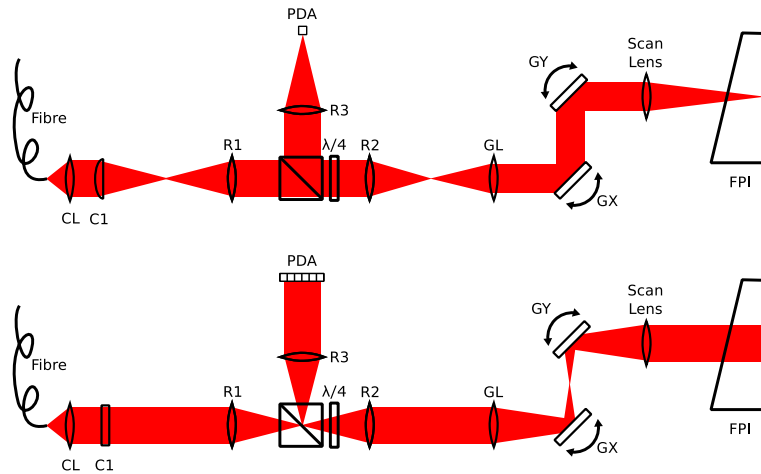


FIGURE 6.6: **Multibeam setup using a laser line generator** **top, bottom**) Two orthogonal views of the optical path. **R1-3** - relay lens, **PBS** - polarising beam splitter, **PDA** - photodiode array, **CL** - Colimation lens, **C1** - Cylindrical lens, **FPI** - Fabry-Perot Interferometer, **GX-GY** - Galvo mirrors.

power difference as well as the baseline curvature due to changing mirror reflectivity. The measured ITFs show very nice overlap (**Figure 6.7a**) even when zoomed in into the peak region (**Figure 6.7b**).

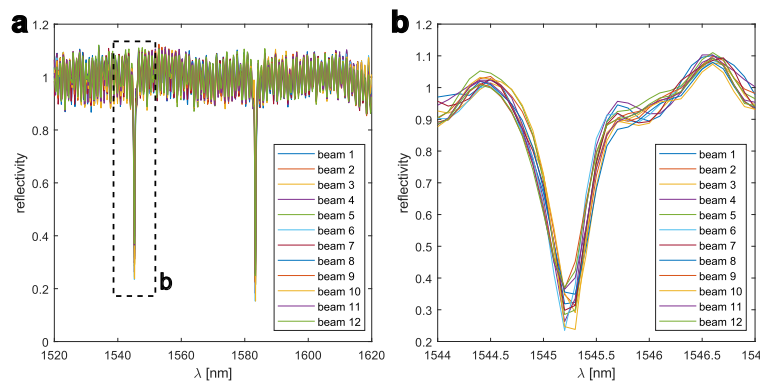


FIGURE 6.7: **12-beam characterisation of the FPI** **a)** The measured ITF of the FPI using 12 interrogation beams. **b)** Zoom-in to the a subregion of the ITF showing the spectral overlap between to 12 interrogated spots.

It is important to note here that the practical use of a laser line brings additional complexity to both the characterisation as well as the measurement scheme. Because the line needs to be aligned with the direction of the lowest variation of λ_{opt} , very careful consideration needs to be put in designing the scanning trajectory software which is still under development.

6.2.4 Measuring ultrasound signals using M-PACT

The next stage of validation is performing actual ultrasound measurements using the multibeam system. Here, I performed simultaneous 4-channel recording of synthetic ultrasonic signals generated by an ultrasound transducer. These preliminary measurements show that parallel recordings are possible with the M-PACT system as all channels show good SNR and a similar signal shape (**Figure 6.8**).

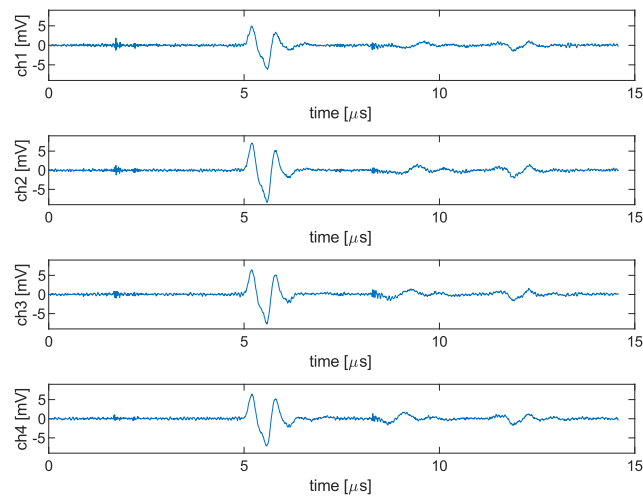


FIGURE 6.8: **Parallel 4-beam recording of US waves using M-PACT**

6.2.5 Discussion

Topics described in this chapter highlight both the importance and challenges of performing high speed PA measurements using the FPI-PAT system. Both the interrogation laser as well as the FPI properties need to be taken in careful consideration. The advancements presented in **Section 6.1** are already advanced and became the standard of performing photoacoustic imaging in our lab due to their stable performance and has achieved large increase in imaging speed.

On the other hand, **Section 6.2** describes work still under development, although considerable progress was made. The key challenges in optical design and multi-channel detection were solved, however, there are still considerations connected to calculation of the optimal scan path for a given optimal wavelength map on the surface of the FPI. These need to be solved before actual photoacoustic imaging using the multibeam setup can be performed.

Additionally, during my PhD, I have explored other potential schemes for speeding up all-optical photoacoustic tomography. As this schemes are not central to the topic of this thesis they are elaborated on in **Appendix B**.

Chapter 7

Outlook

All the topics discussed previously were connected to developed projects where a considerable amount of data was collected and analysed. In contrast, this section outlines other areas of my PhD work which are at a less advanced stage. Most of the topics presented in this section are connected to the challenges involved in PA based calcium imaging in living mice. **Section 7.1** will briefly discuss the general limitations of resolution in FP-PAT systems before focusing on tackling particular problems in trans-cranial PA imaging which are relevant for calcium imaging. On the other hand, **Section 7.2** will be connected to comparing and choosing proper calcium indicators for PA based neuroimaging.

7.1 Improving resolution of Fabry-Pérot based photoacoustic systems

7.1.1 Factors limiting resolution of FP-PAT

Several factors can limit resolution in FP-PAT. The most fundamental ones: the limited acoustic bandwidth of detected signals as well as the resolution of the detector grid (number of scans positions used in FP-PAT), are common for all PAT systems. However, due to the use of a finite planar detector geometry in FP-PAT systems, they show an additional limitation because of the limited view problem (lack of certain detection angles in the raw data). Additionally, inhomogenities in the acoustic properties of the imaged sample can give rise to acoustic aberrations which further limit the resolution of PAT systems.

Material	Speed of sound [m/s]
Water	1482
Blood	1559 - 1590
Brain	1506 - 1565
Fat	1412 - 1490
Skin	1537 - 1720
Kidney	1513 - 1565
Air	343
Esophagus lumen	343
Lung (inflated)	1190 - 1283
Cortical bone	2660 - 4200
Cancellous bone	1855 - 2450
Skull cortical	2190 - 3360
Skull cancellous	1854 - 2450

TABLE 7.1: Speed of sound in biological tissues

Acoustic aberrations

Acoustic aberrations stem from heterogeneity of speed of sound inside the imaged tissue. This is not a practical problem in most PA imaging situations as soft tissues tend to have a very similar speed of sound (SoS; **Table 7.1**). There are two key exceptions to this rule: **(1)** air filled cavities in the body such as the esophagus, lungs and the bowel, **(2)** stiff calcified tissues such as bones. This causes challenges for PAT to image through bones or lungs, and becomes especially important for some PA applications such as neuroimaging.

In case of neuroimaging, the soft tissue of interest (brain) is surrounded by a skull that has a significantly different SoS, which resembles the situation of refractive index mismatch connected to the use of coverslips in light microscopy. In both cases the sharp discontinuity of material properties (acoustic and optical respectively) induces optical aberrations which cause deterioration of resolution and contrast (see **Figure 7.1** for a comparison an ideal acoustic PSF [**right**] and an aberrated acoustic PSF [**left**]).

7.1.2 Modelling the effects of acoustic aberrations on the PAT PSF

To model the possible effects of acoustic aberrations on signal quality I performed computer simulations using the open source matlab toolbox for acoustic simulations (k-Wave, Treeby, Zhang, and Cox, 2010). To recapitulate a model situation in transcranial imaging of mice, I built a layered model incorporating a brain layer as well as a skull layer with physiologically relevant thickness of $\sim 300 \mu\text{m}$. As this was designed to be a proof of principle simulation, the skull was modeled as flat layer with randomly varying thickness within the physiological range. The simulation revealed strong aberrations of the acoustic PSF of the FP-PAT system leading to a loss of both resolution as well as contrast (**Figure 7.1**). This lead us to believe that developing aberration correction techniques for PA image reconstruction is particularly relevant for the context of transcranial imaging.

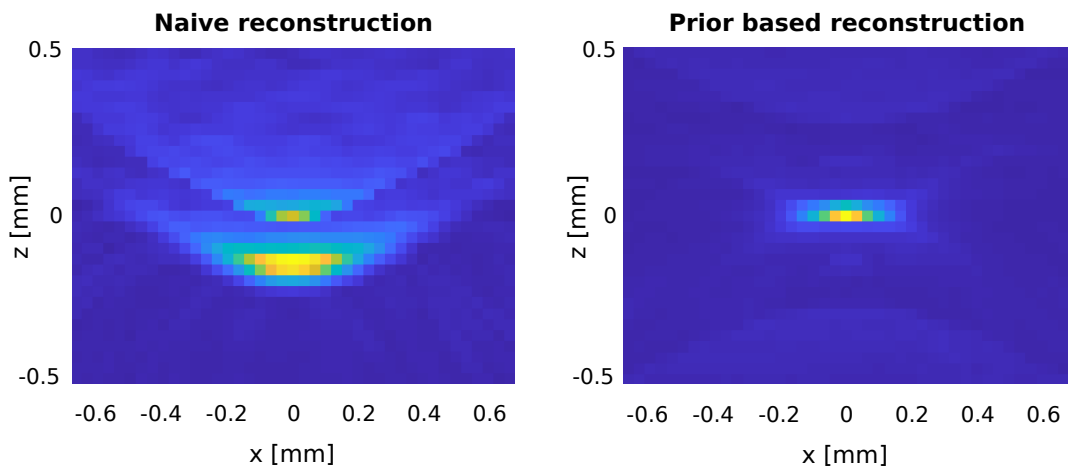


FIGURE 7.1: Comparison of PA image reconstruction schemes for trans-cranial PAT

7.1.3 Tackling aberration induced loss of resolution

Chapter 5 discussed effects of optical aberrations on the sensitivity of the FPI as well as the challenges connected to correcting those aberrations. Fortunately, tackling acoustic aberrations is more straightforward than tackling their optical counterparts because in acoustics, we usually have access to both the phase and amplitude information of the waves allowing for computational AO correction in the image reconstruction step.

Prior based reconstruction

While simultaneous PAT and speed-of-sound reconstruction is possible from the pure PA data, there are several challenges that need to be addressed and these techniques were developed only for 2D reconstructions (Cui et al., 2020). Upscaling them to 3D reconstructions would require a large increase in computational power and is thus impractical. Because of this we decided to pursue an alternative path where the speed-of-sound can be measured indirectly by using a complementary technique. Since our sample can be approximated to be composed of two mechanically distinct tissues (the soft brain and skin tissues and the stiff skull tissue) locating the bone in the imaged volume should be sufficient for speed-of-sound estimation based on the autofocus method (Treeby et al., 2011). This information can then be used in the PA reconstruction as a prior and is capable of improving image quality as can be shown using computer simulations (**Figure 7.1**).

Experimental acquisition of the prior using a dual-modality approach

To this end, I designed and developed a dual-modality system combining PAT with optical coherence tomography (OCT, **Figure 7.2**). OCT is an optical technique capable of label-free imaging using differences in refractive index as a contrast, it was also shown to successfully visualise the skull in living mice (Liu et al., 2012).

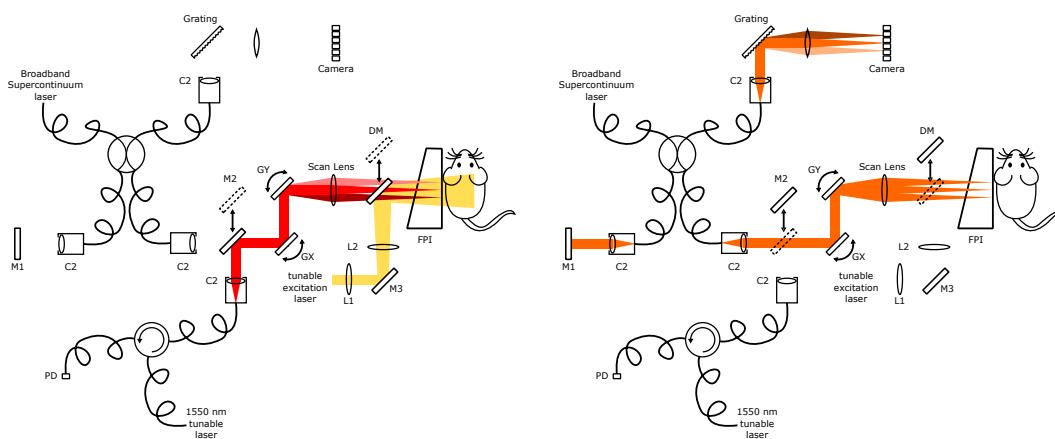


FIGURE 7.2: Scheme of the dual-modality Optical Coherence - Photoacoustic Tomography system (left) Photoacoustic tomography setup design. (right) Optical coherence tomography setup design.

7.2 Photoacoustic imaging of genetically encoded calcium indicators

Performing PA based calcium-imaging requires the use of proper calcium sensor which would show promising properties for PA imaging. As currently, dedicated PA calcium indicators are still lacking there is a need to choose among the readily available fluorescent genetically encoded calcium indicators (GECIs). The challenge here lies in the fact that most of the available GECIs were not characterised for their PA properties and thus their expected PA-performance need to be inferred from their photo-physical properties.

7.2.1 Inferring PA signal quality from photo-physical properties of GECIs

Following **Equation 2.2** the change in fluorescence of a calcium indicator can be defined as:

$$\frac{\Delta F}{F} = \frac{\phi_{th}^+ \mu_a^+ - \phi_{th}^- \mu_a^-}{\phi_{th}^- \mu_a^-} = \frac{\phi_{th}^+ \mu_a^+}{\phi_{th}^- \mu_a^-} - 1 \quad (7.1)$$

where ϕ_{th}^+ and ϕ_{th}^- denote the quantum efficiency in the calcium-bound and calcium-free state respectively and, similarly μ_a^+ and μ_a^- denote the absorption coefficient in the calcium-bound and calcium-free state respectively.

By assuming that $\eta_{th} = 1 - \phi_{th}$ and that the value of μ_a does not differ between fluorescence and PA the same photo-physical constants can be used to calculate the change in PA signal of a calcium indicator following **Equation 2.1**:

$$\frac{\Delta PA}{PA} = \frac{\eta_{th}^+ \mu_a^+}{\eta_{th}^- \mu_a^-} = \frac{(1 - \phi_{th}^+) \mu_a^+}{(1 - \phi_{th}^-) \mu_a^-} - 1 \quad (7.2)$$

It is important to note that there is no simple relation between the quality of a molecule as a fluorescent calcium indicator and its quality as a PA calcium indicator. The reason stems from the fact that the signal change is the effect of four independent variables: ϕ_{th}^+ , ϕ_{th}^- , μ_a^+ , μ_a^- . **Table 7.2** exemplifies the interplay between those variables on hypothetical examples:

case#	ϕ_{th}^-	μ_a^-	ϕ_{th}^+	μ_a^+	$\Delta F/F$	$\Delta PA/PA$
(1)	0.5	1	1	1	1	0
(2)	0.5	1	0.7	1.4	0.96	-0.22
(3)	0.5	1	0.5	2	1	1
(4)	0.95	1	0.90	2	0.89	4
(5)	0.05	1	0.10	2	4	0.89

TABLE 7.2: Comparison of abstract model calcium indicators

Cases **(1-3)** show that a good positive fluorescent calcium indicator (FCI) showing a 100% increase in fluorescence upon calcium binding can be either an equally good PA calcium indicator PACI **(3)** an absolutely terrible PACI **(1)** or a weak negative PACI **(2)**, among other options. Additionally, for very high quantum efficiencies an equally good FCI **(4)** can be an excellent PACI showing 400% increase in signal level upon calcium binding, naturally for very low quantum efficiencies the converse is true. This list is by no means extensive and was meant to just visualise the complexity of predicting the quality of PACI and FCI without having the proper photo-physical characterisations.

Fortunately, the majority of developed genetically encoded calcium indicators (GECIs) are photo-physically characterised with sufficient detail to use **Equation 7.2** to predict the theoretical $\Delta PA/PA$ values (**Table 7.3**).

name	ϕ_{th}^-	μ_a^-	ϕ_{th}^+	μ_a^+	$\Delta F/F$	$\Delta PA/PA$	$ \Delta PA $	$ \Delta PA /\sqrt{PA}$
jRGECO1a	0.120	5.5	0.22	41	12.67	5.61	27.14	12.34
f-RGECO1	0.124	4.2	0.26	13.4	5.69	1.70	6.24	3.25
f-RGECO2	0.161	2.9	0.265	21.5	11.20	5.49	13.37	8.57
jRCaMP1a	0.308	1.7	0.515	5.3	4.21	1.19	1.39	1.29
f-RCaMP1	0.188	3.4	0.425	7.8	4.19	0.62	1.72	1.04
f-RCaMP2	0.239	2.2	0.367	4.9	2.42	0.85	1.43	1.10
NIR-GECO1	0.063	62.0	0.019	20	-0.90	-0.66	38.47	5.05
GCaMP6s	0.110	33.3	0.61	77	11.82	0.01	0.39	0.07
FGCaMP	0.480	55.0	0.46	106	0.85	1.00	28.64	5.36
CaMPARI(G)	0.750	70.5	0.64	9.2	-0.89	-0.81	14.31	3.41

TABLE 7.3: Comparison of real GECI - the photo-physical data was collected from: Qian et al., 2019; Barykina et al., 2017; Mishin et al., 2015; Dana et al., 2016; Kerruth et al., 2019; Zarowny et al., 2020.

For these realistic sensors we also observe similar characteristics to those described in **Table 7.2** (e.g. GCaMP6s on of the brightest fluorescent GECI is predicted to be a poor PA GECI). Additionally, it is important to note that $\Delta PA/PA$ is not the sole parameter that determines the usability of a GECI in PAT. The other important factor is how strong the PA signal itself is, as due to limited sensitivity of PAT (as compared to optical imaging) having a sufficient signal level to even detect the GECI is not assured. Here, the absolute change in brightness ($|\Delta PA|$) provides a proxy on how strong a signal we can expect from the various GECIs (**Figure 7.3**), additionally if we assume that the PA images are shot noise limited we can use $|\Delta PA|/\sqrt{PA}$ as a metric approximating the SNR of these GECIs.

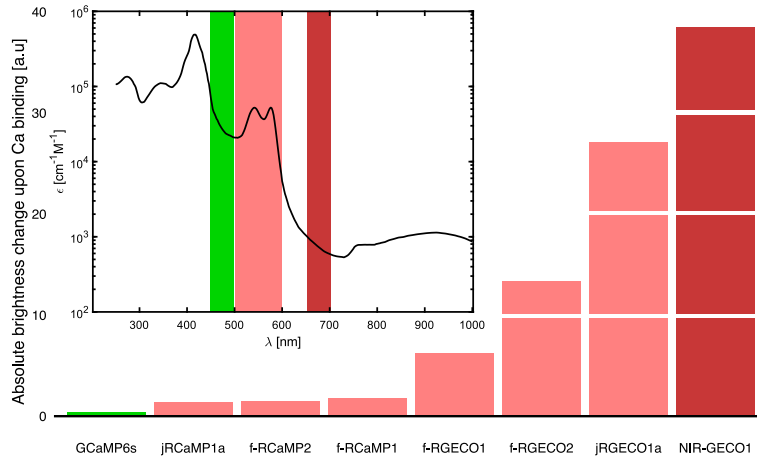


FIGURE 7.3: **Absolute brightness change ($|\Delta PA|$) for various GECIs inset) Blood absorption spectrum (Prahl, 1998) showing the predicted background for the three spectral windows used in currently developed GECI (green, red and NIR).**

By analysing all the discussed parameters we see that out of the considered GECIs jRGECO1a and f-RGECO2 seem to be the best candidates for PA based calcium imaging. Unfortunately, there are strong limitations for using both green and red GECIs in PA-based neuroimaging which become clear by analysing the blood absorption spectrum. As discussed in **Section 4.6.1** blood signal always forms background in PA imaging of mice and causes additional excitation light attenuation that

limits the achievable depth of penetration. A recent study on using UST based PAT for calcium imaging with GCaMP6m (Gottschalk et al., 2019) has shown that using 488 nm excitation limits the imaging depth to only a the superficial layers of the brain as opposed to using 650 nm.

This motivates the need for development of NIR shifted calcium indicators such as NIR-GECO1. Because of the better spectral window properties combined with the fact that NIR-GECO1 is predicted to be a good PACI we decided to use it as a candidate GECI in our experiments.

Chapter 8

Conclusions

Establishing novel and custom imaging systems is an arduous task as they need to be developed from scratch and carefully validated, while little relevant literature typically exists. This requires the researchers to often trace-back on their own developments to gain a deeper understanding on the underlying physics of the processes used in the systems. Here, the result of this is reflected in the introductory chapters, especially the sections connected to validation (**Chapter 4**) which collect the basic, but significant insights into the operating principles of FP pressure sensors I have gathered throughout my PhD. Most importantly, the main aim of this thesis, establishing a high-performance all-optical photoacoustic tomography system from scratch, was achieved (as described in **Chapter 3** and **Chapter 4**) and provided a base for possible future developments.

The ultimate, arguably very ambitious, aim of the project, namely achieving whole-brain photoacoustic calcium-imaging in mice, proved to be beyond the scope of this thesis. However, I would like use this chapter to briefly discuss the achievements included in this thesis in the context of possible neuroimaging.

A large portion of this work (**Chapter 5**) is concerned with improving the sensitivity of FP-based PAT systems. This topic is crucial for performing PA-based neuroimaging as calcium imaging requires much higher SNR than typical PAT applications (as discussed in **Section 7.2**). As the FPI is an optical device, possible improvements of its sensitivity require a very thorough understanding of the physics underlying its operation. The use of FP based pressure sensors was studied theoretically from many angles (Beard, Perennes, and Mills, 1999; Varu, 2014; Marques et al., 2020). However, how optical aberrations interact with FPI pressure sensor cavities and what is their effect on FPI sensitivity was not previously explored. Based on the preexisting literature I developed a new theoretical framework to address this questions and described possible ways of tackling this problem using both adaptive optics and mode filtering (**Section 5.1**, Czuchnowski and Prevedel, 2020). This work has important consequences as it potentially allows FP systems to perform at much higher sensitivities provided that the appropriate correction strategies are employed. We further capitalised on this finding by developing an experimental approach that allows AO enhanced PA imaging with increased sensitivity (**Section 5.2**, Czuchnowski and Prevedel, 2021) as well as by comparing the performance of free-space and fibre-coupled photodetectors for FP-PAT (**Section 5.3**). The work connected to AO enhancement of sensitivity was limited in scope by the low number of active elements in the deformable mirror used which limited the AO to lower order Zernike mode only. I believe that the use of larger DMs or SLMs with more active elements allowing finer control over the beam profile can lead to even further improvements in the achievable sensitivity. These particular advancements were focused specifically on FP based systems, however, I also worked on developing sensitivity enhancement scheme with more general applications. Using passive amplification

of photodiodes might prove useful in all types of all-optical photoacoustic imaging techniques (**Section 5.4.1**). Additionally, the deep learning-based denoising (**Section 5.4.2**) might find applications in all types of photoacoustic tomography. That being said, more effort needs to be put into validation and refining of these techniques before they are proven to be useful and are widely applicable.

Another large part of this thesis is the ongoing effort to increase the temporal resolution of FP-based photoacoustic methods (**Chapter 6**). The aim here is to match the minimal requirement for calcium activity imaging of 1 volume/s. Initial improvements are based on optimising the data acquisition procedure by utilising a random access scanning scheme that minimises the laser-dependent dead-time due to wavelength tuning (**Section 6.1**). This approach enables an order of magnitude improvement in the temporal resolution by allowing near PRR limited data acquisition. Further improvements are made by utilising optical multiplexing to go beyond PRR limited data acquisition (**Section 6.2**) and bridge the gap between the 0.02 volume/s achievable with a single interrogation beam and the required 1 volume/s. Currently, the setup operates at 12 beams which allows for a quarter the required volume rate (0.24 volume/s) for the full field-of-view ($\sim 1 \text{ cm} \times 1 \text{ cm}$) but can be used for 1 volume/s imaging at a reduced 5 mm x 5 mm field-of-view. Future developments and experiments are needed to determine whether this setup is capable of imaging calcium activity, however, purely from the technical side it does meet the minimal requirements.

Finally the last part of the thesis is concerned with efforts in tackling other problems associated with brain activity imaging. **Section 7.1** describes potential ways of tackling acoustic aberrations induced by skull by incorporating the information about the skull location and thickness into the reconstruction. This would allow imaging of the brain through an intact skull minimising the invasiveness of the process by removing the need for craniotomy. Also, it would be required for whole-brain imaging as cranial windows are limited in size to only a few millimeters in diameter. **Section 7.2** discusses the possible choices of genetically encoded calcium indicators for PA imaging. As no dedicated GECIs for PA exist there is a need to choose the best possibilities out of the available fluorescent protein toolkit. This section introduces a simple photophysical metric to evaluate possible candidates and motivates the need for near-infrared calcium indicators.

In conclusion, a high-performance all-optical photoacoustic setup was established as an outcome of this thesis and several improvements (compared to similar systems in the literature) to its performance were achieved. By taking those improvements further it is possible to attempt photoacoustic-based calcium imaging in living mice which will be the next stage of this project.

Appendix A

Fundamental cross-compensation of Zernike aberrations

Appendix A collects parts of the theoretical work done as the extension of the theoretical framework developed in **Chapter 5** to explain light-cavity interactions. Here, a similar framework is used to explain fundamental optical interactions between Zernike type aberrations and Gaussian beams often used in optical imaging.

Zernike polynomials are one of the most widely used theoretical models of optical aberrations in the fields of imaging and adaptive optics. Their mathematical orthogonality as well as isomorphisms with experimentally observable aberrations make them a very powerful tool in solving real-life problems in adaptive optics.

It has been shown previously that Zernike aberrations are orthogonal only in the case of the plane beam (Mahajan, 1994; Mahajan, 1995) and show cross coupling in the case of Gaussian beams. The effects of this cross couplings were analysed based on the Strehl ratio approach. Here we propose an alternative formulation based on analysing the effects Zernike type aberrations in inducing power coupling into higher order Laguerre-Gauss modes (Mah and Talghader, 2019; Bond et al., 2011; Czuchnowski and Prevedel, 2020) and use it to gain intuitive understanding of various model situations in Adaptive Optics such as iterative improvement of cross-compensating Zernike aberrations and cascading aberrations. We also extend our approach to shed light on Zernike aberrations interactions in the high aberration regimes.

A.1 Coupling between Zernike aberrations and Laguerre-Gauss modes in the low aberration regime

Laguerre-Gauss beams as eigenvectors of the wave equation are inherently orthogonal and therefore do not cross-couple between each other. However it has been shown that Zernike type aberration can induce cross coupling between different LG-beams Bond et al., 2011. The coupling coefficient can be expressed as:

$$k_{p,l,p',l'}^{n,m} = \int_S LG_{p,l} \exp(2ikZ_n^m) LG_{p',l'}^* dS \quad (\text{A.1})$$

in the low aberration regime we can approximate:

$$\exp(2ikZ_n^m) = 1 + 2ikZ_n^m \quad (\text{A.2})$$

which simplifies **Equation A.1** to an analytically solvable integral:

$$k_{p,l,p',l'}^{n,m} = \int_0^{2\pi} \int_0^R LG_{p,l} LG_{p',l'}^* (2ikZ_n^m) r dr d\phi \quad (\text{A.3})$$

The equation can be separated into azimuthal and radial parts which can be solved independently, starting with the azimuthal part:

$$\phi_{p,l,p',l'}^{n,m} = \int_0^{2\pi} e^{i\phi(l-l')} \frac{e^{im\phi} + e^{-im\phi}}{2} d\phi = \left[\frac{e^{i\phi(l-l'+m)}}{2i(l-l'-m)} + \frac{e^{i\phi(l-l'+m)}}{2i(l-l'-m)} \right]_0^{2\pi} \quad (\text{A.4})$$

which specifies the coupling condition:

$$\phi_{p,l,p',l'}^{n,m} = \begin{cases} 0 & \text{if } m \neq |l-l'| \\ \pi & \text{if } m = |l-l'|, \text{ even } Z_n^m \\ \text{sgn}(l-l')i\pi & \text{if } m = |l-l'|, \text{ odd } Z_n^m \\ 2\pi & \text{if } m = 0, l = l' \end{cases} \quad (\text{A.5})$$

This means that efficient coupling between modes can occur only under the condition that $m = |l-l'|$. As in most imaging applications we are mainly concerned with aberrations acting on the fundamental Gaussian mode (LG_{00}) this simplifies the coupling condition to $m = |l'|$. This has fundamental consequences for our analysis as it provides a mapping from particular sets of Z-modes into particular families of LG-beams (**Figure A.1a**).

A.1.1 Generalised Adaptive-Optics task

As we operate in the LG-beam space there is a need to define how we will quantify the effects of Zernike aberrations on the beam quality. The most intuitive metric would be to look at the power fraction coupled into higher order LG-beams. In this sense the goal of aberration correction in the general sense could be defined as redirecting the power back into the fundamental Gaussian mode. The coupling condition ($m = |l'|$) allows us to easily map all beams aberrated by a particular class of Zernike aberrations into a subspace of LG-beam vector space:

$$\mathbf{G}^{n,m} = \sum_p k_{p,\pm m}^{n,m} \mathbf{LG}_{p,\pm m} \quad (\text{A.6})$$

where $\mathbf{LG}_{p,\pm m}$ are understood as base vectors and $k_{p,\pm m}^{n,m}$ is the amplitude coupling coefficient Bond et al., 2011 (see **Figure A.1b, c**). The power coupled into higher order modes can then be simply calculated as the square of the vector length:

$$P_{n,m} = \|\mathbf{G}^{n,m}\|^2 \quad (\text{A.7})$$

Additionally in the low aberration regime interactions between different Zernike aberrations translate to simple vector additions and their effect on the outcoupled power can be expressed as follows (**Figure A.1b**):

$$P_{n^*,m^*}^{n,m} = \|\alpha \mathbf{G}^{n,m} + \beta \mathbf{G}^{n^*,m^*}\|^2 \quad (\text{A.8})$$

If we assume that α is fixed and β can be adjusted to attempt an AO correction the optimal reduction of outcoupled power can be calculated from geometrical relations between vectors:

$$\min\{P_{n^*,m^*}^{n,m}\} = \left[\alpha \|\mathbf{G}^{n,m}\| \sin \gamma \right]^2 \quad (\text{A.9})$$

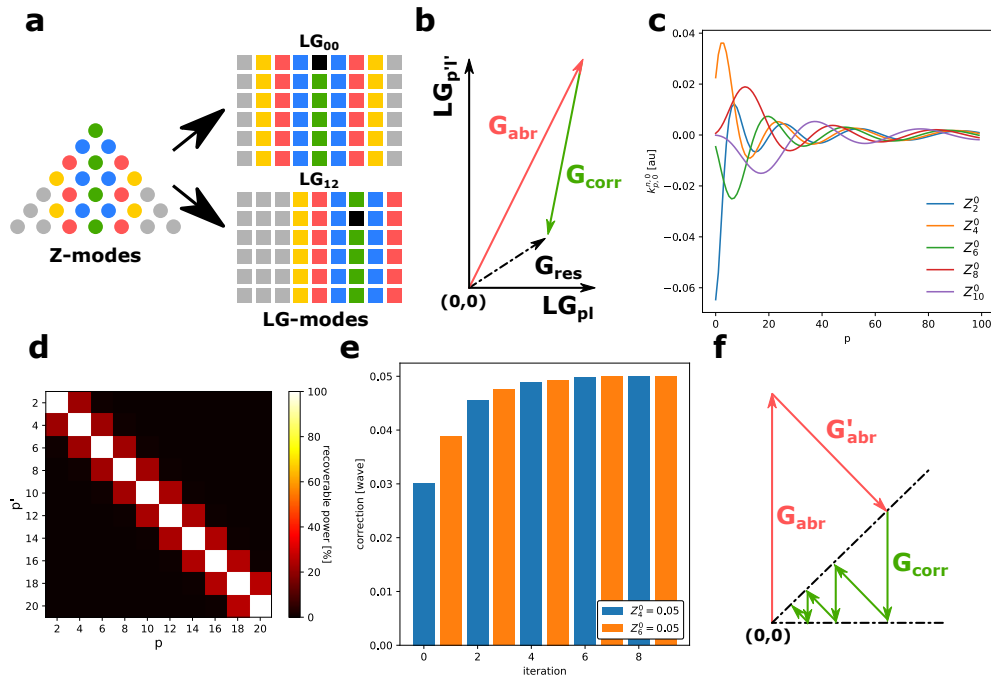


FIGURE A.1: **Description of Zernike cross-compensation in the weak aberration regime**
a) Coupling from classes of Z-modes to classes of LG-modes depending on which LG beam we assume as the fundamental beam we are using. **b)** Cartoon representation of aberrated beams (G_{abr}) as vectors in the LG space as well as the possibility of cross compensation by non-orthogonal aberrated beams (G_{corr}). **c)** Amplitude coupling coefficients into different LG-modes induced by Zernike aberrations of the Spherical aberration class. **d)** Quantification of the cross-compensation between different modes in the Spherical aberration class (Z_n^0), expressed as the percentage of power out-coupled from the fundamental G-mode that can be recovered. **e)** Iterative adaptive optics correction for two cross coupling aberrations. **f)** Geometric interpretation of iterative adaptive optics correction for two cross coupling aberrations. The iterative improvement is trapped between the two dotted lines which are the orthogonals of the aberration vectors.

where γ is the angle between vectors $\mathbf{G}^{n,m}$ and \mathbf{G}^{n^*,m^*} . In case $\gamma = \pi/2$ the two vectors are orthogonal and unable to cross-compensate, otherwise the vectors can cross-compensate at least residually. We investigate the cross-coupling characteristics in the spherical aberration class (Z_n^0) and show that there is significant cross-compensation only between neighbouring aberrations (**Figure A.1d**). As the angle between vectors was calculated numerically for a finite set of LG-beam it has an uncertainty from discarding the higher order beams.

We propose a simple estimation for the upper bound of this uncertainty based on vector properties and show that the angle is significantly different from $\pi/2$ for the considered cases. We can easily define the lower band (γ_{LB}) and upper band (γ_{UB}) respectively where:

$$\gamma_{LB}(\mathbf{G}^{n,m}, \mathbf{G}^{n^*,m^*}) = \gamma - \Delta\gamma^{n,m} - \Delta\gamma^{n^*,m^*} \quad (\text{A.10})$$

and

$$\gamma_{UB}(\mathbf{G}^{n,m}, \mathbf{G}^{n^*,m^*}) = \gamma + \Delta\gamma^{n,m} + \Delta\gamma^{n^*,m^*} \quad (\text{A.11})$$

where

$$\Delta\gamma^{n,m} = \arctan \sqrt{\frac{|k_{GG}^{n,m}|^2 - \|\mathbf{G}^{n,m}\|^2}{\|\mathbf{G}^{n,m}\|^2}} \quad (\text{A.12})$$

$$\begin{aligned} k_{GG}^{n,m} = & 1 + 2Aik \sum_{h=0}^{\frac{1}{2}(n-m)} \frac{(-1)^h (n-h)!}{(\frac{1}{2}(n+m)-h)! (\frac{1}{2}(n-m)-h)! h! X^{\frac{1}{2}(n-2h)}} \gamma(1-h + \frac{1}{2}n, X) \\ & - 2k^2 A^2 \sum_{h=0}^{\frac{1}{2}(n-m)} \sum_{g=0}^{\frac{1}{2}(n-m)} \frac{(-1)^{h+g} (n-h)! X^{h+g-n}}{(\frac{1}{2}(n+m)-h)! (\frac{1}{2}(n-m)-h)! h!} \times \\ & \times \frac{(n-g)!}{(\frac{1}{2}(n+m)-g)! (\frac{1}{2}(n-m)-g)! g!} \gamma(n-h-g+1, X) \quad (\text{A.13}) \end{aligned}$$

A.1.2 Correcting multiple cross-compensating aberrations

Now we can use our framework to model a typical correction scheme in indirect adaptive optics where different Zernike corrections are applied in an iterative fashion to see the effects of aberration cross-compensation:

$$\mathbf{G}^{n,m,n^*,m^*} = (\alpha_1 + \beta_1) \mathbf{G}^{n,m} + (\alpha_2 + \beta_2) \mathbf{G}^{n^*,m^*} \quad (\text{A.14})$$

where α_1 and α_2 are fixed aberrations and β_1, β_2 are the correction coefficients which are updated iteratively. Aberration cross-compensations will cause the coefficients to evolve over several iterations until they converge at the proper values (**Figure A.1e**). This behaviour can be intuitively understood by looking at the geometrical interpretation of our theory (**Figure A.1f**). The situation for only a single fixed aberration is conceptually the same. It is important to note here that odd ($m < 0$) and even ($m \geq 0$) Zernike aberrations do not cross-compensate, even though they couple into the same LG modes, because they are orthogonal in phase (as can be seen from **Equation A.5**).

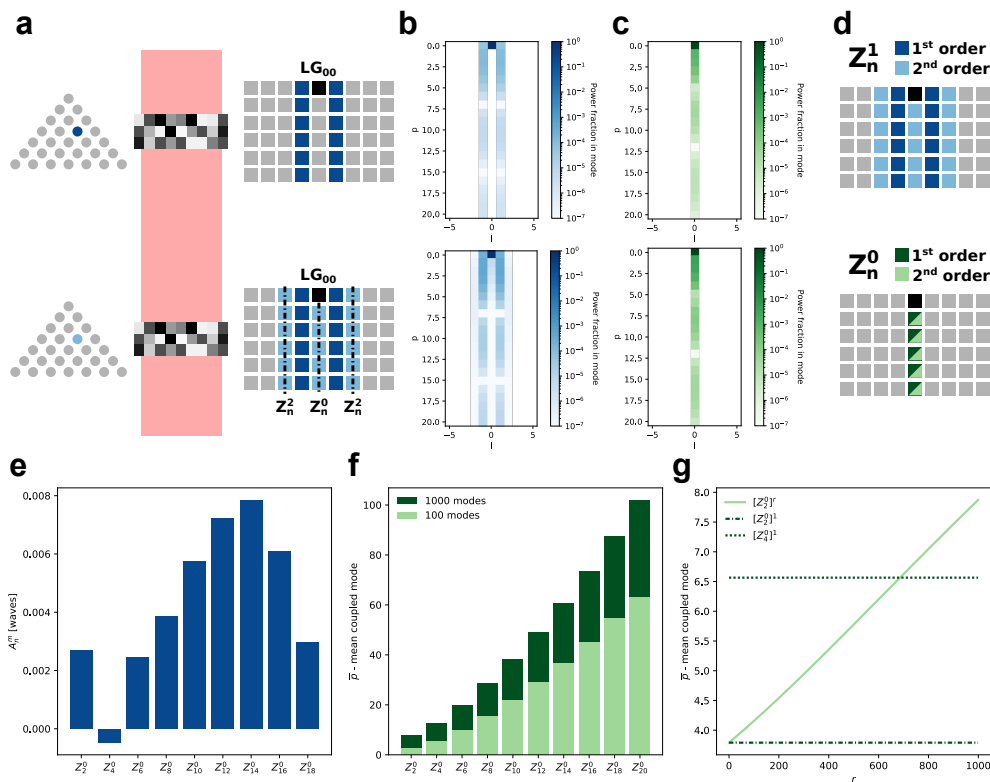


FIGURE A.2: Description of Zernike cross-compensation in the strong aberration regime
a) Sequentially cascading two Z_3^1 aberrations (Coma). **b)** Powered coupled to LG-modes for a cascading Z_3^1 aberration. **c)** Powered coupled to LG-modes for a cascading Z_2^0 aberration. **d)** Cartoon showing 1st and 2nd order coupling into LG-modes for $Z_n^{\pm 1}$ -class and Z_n^0 -class aberrations. **e)** Z-mode decomposition of the residual power coupled into the $LG_{p,0}$ -family caused by a cascading Z_3^1 aberration (**panel b**) showing possible cross-compensation between Z-classes. **f)** Mean coupled mode (\bar{p}) quantification for the Z_n^0 -class aberrations showing that higher order Z_n^0 -aberrations couple power into higher order LG-modes. **g)** Mean coupled mode (\bar{p}) quantification for a cascading Z_2^0 aberration showing that for higher order cascades (and consequently higher order coupling coefficients) power is being coupled into higher order LG-modes resembling the effects of higher order Z-aberrations.

A.2 Cascading aberrations and the high aberrations regime

The use of LG space in our framework allows us to look into aberrated beam evolution in a very straightforward manner as LG modes are eigenvectors of the wave equation. This allows us to address questions concerning effects of cascading aberrations where the evolving beam interacts twice with the same type of Zernike aberration (**Figure A.2a**). In this case we see that re-applying a Z_3^1 (Coma) aberration to a Z_3^1 -aberrated Gaussian beam will cause coupling into LG-modes characteristic for the Spherical aberration (Z_n^0) and Trefoil ($Z_n^{\pm 2}$) Z-mode classes (**Figure A.2b**).

Conceptually cascading aberrations show similarities to the effects of Zernike aberrations in the high aberrations regime which we will now discuss. In the high aberrations regime it becomes necessary to consider higher order coupling terms which modify the coupling conditions between Z-modes and LG-modes Bond, 2014:

$$\exp(2ikZ_n^m) = 1 + 2ikZ_n^m + 2(ikZ_n^m)^2 \quad (\text{A.15})$$

The resulting approximation of **Equation 1** is still solvable analytically in an analogical way Bond, 2014 and the resulting coupling condition from the azimuthal integral is the following:

$$\phi_{p,l,p',l'}^{n,m,2} = \begin{cases} 0 & \text{if } 2m \neq |l - l'|, l \neq l' \\ \frac{\pi}{2} & \text{if } 2m = |l - l'|, \text{ even } Z_n^m \\ -\frac{\pi}{2} & \text{if } 2m = |l - l'|, \text{ odd } Z_n^m \\ \pi & \text{if } l = l', m \neq 0 \\ 2\pi & \text{if } l = l', m = 0 \end{cases} \quad (\text{A.16})$$

We see now that 2^{nd} order coupling populates the same LG-modes as a cascading aberration, which allows us to intuitively look at the Z-mode cross-compensation in the high aberration regime (**Figure A.2a, d**).

We observe that there are two special classes of Zernike aberrations. The Z_n^0 -class (Spherical aberrations) is special, because of the coupling from Z_n^0 -modes is always constrained to the same class of LG-modes ($LG_{p,0}$) regardless of the strength of the aberration (**Figure A.2c, d**). Because of this we can define an easy metric to look at the scaling between the different orders of Z-modes and LG-modes. We show that higher order Z_n^0 -modes couple to higher order LG-modes (**Figure A.2f**), and interestingly that cascading lower order aberrations (Z_2^0) over several iterations start to shift the power coupling into higher order modes (**Figure A.2g**). Additionally due to **Equation A.16** all Zernike aberrations will cause coupling into the $LG_{p,0}$ -class if the 2^{nd} order is considered, facilitating possible cross-compensation between different Z-mode classes (**Figure A.2b, e**). Secondly, the $Z_n^{\pm 1}$ -class (Coma) is special because it densely populates the LG-space as the aberration magnitude becomes larger, which will also facilitate possible cross-compensation. Higher order Zernike aberration classes populate the LG-space in a progressively more sparse manner thus facilitating possible cross-compensation to a lower degree.

A.2.1 Translation to experimental quality metrics

In the previous sections we focused on the effects of aberrations in a generalised abstracted framework. It would also be interesting to explore whether this framework can be adapted to the use of different quality metrics that are often optimised in experimental Adaptive Optics. This can be in principle achieved by allowing weight

parameters (w_p) for different LG-modes that would tailor the vector space to particular metrics.

$$\mathbf{G}^{\mathbf{n},\mathbf{m}} = \sum_p k_{p,\pm m}^{n,m} w_p^\pm \mathbf{LG}_{p,\pm m} \quad (\text{A.17})$$

Unfortunately this is only possible if the effects of different $\mathbf{LG}_{p,\pm m}$ on the metric of choice are independent. For example we have previously shown that theoretically for μFPI sensitivity there exists an approximately linear relationship between the power contained in the fundamental mode and the expected optical sensitivity. In this framework that would translate to a set of weights:

$$\forall_{p \in \mathbb{N}^+} : w_p^\pm = 1 \quad (\text{A.18})$$

Appendix B

Alternative fast all-optical methods

Appendix B collects conceptual work on designing novel ultra-fast acoustic sensing methods utilising novel concepts of space-to-time and time-to-space mapping. Although some preliminary work was done on implementing these, the incomplete nature of the data does not allow for a convincing presentation so the sections are limited to presenting the concepts only.

Both of the methods presented here capitalise on specialised equipment developed for optical telecommunication that provides unique opportunities for making systems with interesting optical properties.

B.1 Space-to-time mapping (S2T)

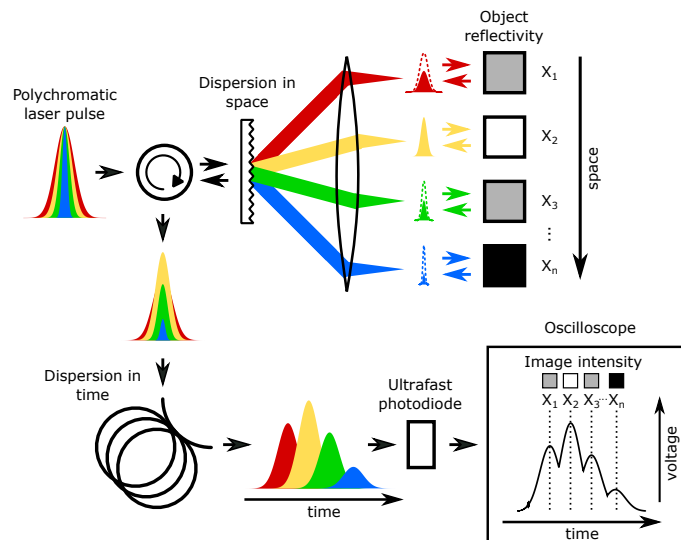


FIGURE B.1: Space-to-time mapping

The concept of space-to-time mapping is inspired by work done by Goda, Tsia, and Jalali, 2009 on using dispersive Fourier transformation (Goda and Jalali, 2013) for ultra-fast imaging of dynamic phenomena. The operating principle is very simple (Figure B.1) a polychromatic laser pulse (i.e. a laser pulse containing a broad range of wavelengths) is dispersed in space using e.g. a diffraction grating which then maps each separate wavelength is focused on a different spatial position. Assuming the reflectivity of the object varies in space, different amounts of light from each point will be reflected back and recombined again into a single pulse. Because of the wavelength-to-space mapping the spatial information about the object is still encoded within the recombined pulse and can be read out via temporal dispersion

(or wavelength-to-time mapping) where a special optical fibre is used which induces wavelength depended delay on the optical pulse. This dispersed pulse is then recorded by an ultra-fast photodiode and the spatial information can be decoded from the temporal profile of the pulse.

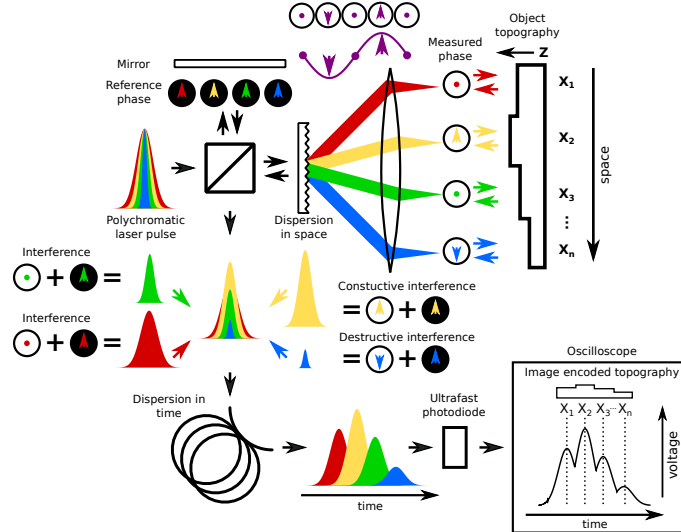


FIGURE B.2: **Principle of Time Encoded Interferometry** A polychromatic laser pulse is used as an input, this pulse is then divided by a beam splitter into the measurement arm and reference arm. In the reference arm the laser is reflected from a mirror set at the same optical path length as the object providing a reference. In the measurement arm however the wavelengths are dispersed in space using a grating so that each wavelength is reflected from a different point on the object. These reflections are then recombined on the grating to form a single pulse again. This pulse then interferes with the reference pulse in such a way that each wavelength interferes separately resulting in constructive and destructive interference. Afterwards this pulse is sent into a dispersing fibre which causes the pulse to broaden in a wavelength dependent manner. This way we achieve ordering of the wavelengths (equivalently pixels of our image) in time. Afterwards the intensity values for each wavelength are read with an ultrafast photodiode and stored in an oscilloscope.

This technique by itself cannot facilitate PA sensing (as it is based on variations in reflectivity) but it can become the basis of an ultra-fast interferometric technique (similar to described in Mahjoubfar et al., 2013) that could perform highly-multiplexed PA all-optical imaging (the concept is described by **Figure B.2**).

B.1.1 Advantages

Fundamentally this approach enables compression of spatial information into a single detector channel (or more generally a low number of detector channels) and capitalises on the use of ultra-fast photodetectors and sensing electronics. The gains can be quickly approximated, in PAT one aims at a detection bandwidth of ≈ 20 MHz and as currently ≈ 50 GHz PDs and oscilloscopes are available it is theoretically possible to accommodate 2500 sensing channels on a single 50 GHz photodiode which provides a very strong incentive towards developing such approaches.

B.1.2 Challenges

This approach however meets several challenges, the most important of which is connected to measurement sensitivity: **(1)** as noise is proportional to the square root

of the measurement bandwidth a 50 GHz photodiode will suffer from 50 fold higher noise than a 20 MHz photodiode; **(2)** FPI which boast one of the highest sensitivities for all-optical PA detection support by nature only a narrow selection of wavelengths for sensing applications which makes them incompatible with this scheme, alternative approach using e.g. Michelson type interferometers suffer from much lower sensitivities (Speirs and Bishop, 2013); **(3)** these types of setups require finely tuned low-noise lasers with broad spectral bandwidths which are not easy to acquire, the more widely available super-continuum based sources unfortunately also suffer from high-noise (Jensen et al., 2019).

B.1.3 Conclusions

All-in-all, while promising these approaches require much development and consideration in design as currently achieving sufficient sensitivity for PA measurements is very challenging.

B.2 Time-to-space mapping (T2S)

Space-to-time mapping relies on performing wavelength-to-space mapping prior to contact with the sample and wavelength-to-time mapping after. If one reverses the order time-to-space mapping can be achieved (**Figure B.3**), here the laser pulse is first dispersed in time so that each wavelength interacts with the sample at a different time point and that dispersed in space to form an image on i.e. a camera chip (this technique can be i.e. used for detection of femtosecond physical phenomena Mouradian et al., 2000). Similarly to S2T, T2S on it's own is incapable of PA sensing however it can similarly be incorporated into a interferometric system.

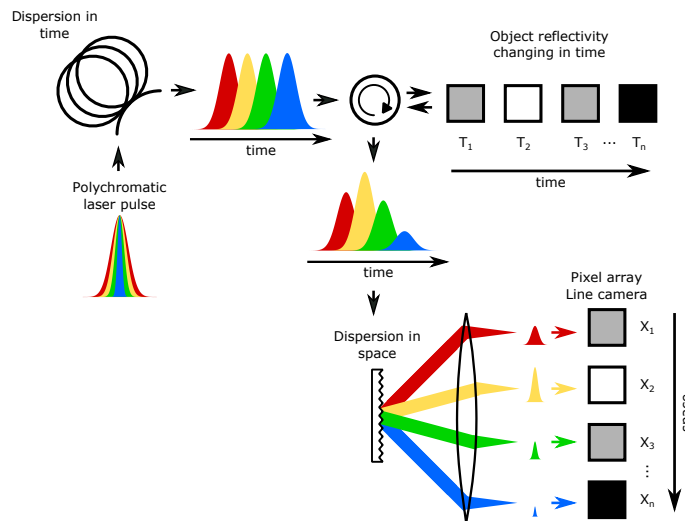


FIGURE B.3: Time-to-space mapping

B.2.1 Advantages

Similarly to S2T, T2S also offers interesting compressing capabilities, As the spatial dispersion is usually 1D the orthogonal dimension can be utilised to probe other spatial positions in parallel (by using laser line detection). This in principle allows to sample spatio-temporal information with as many samples as the camera detector

chip has pixels. As 4 Mpx scientific cameras are readily available this allows for sampling of ≈ 2000 spatial positions with each position being sampled at ≈ 2000 time points. As typical PA datasets consist of ≈ 500 time points (Jathoul et al., 2015) this is fully sufficient for PA sensing. Moreover the typical readout time of cameras (50-100 fps) matches very well the PRR of typical PAT excitation lasers (50 Hz) allowing for very efficient imaging.

B.2.2 Challenges

Similarly to S2T, T2S is also not compatible with FPI sensors as broad spectral bandwidths need to be used. Additionally as the time scales of photoacoustic measurements ($\sim \mu s$) are orders of magnitude longer than the delays that can be achieved with optical dispersion ($\sim ns$) alternative approaches to achieve wavelength-to-time mapping need to be used. Here, the use of swept-source lasers is possible as they usually display tuning dynamic in the microsecond regime.

B.2.3 Conclusions

While T2S is a promising approach for optical multiplexing of PAT measurements several challenges need to be overcome. However, it will be interesting to see if these or similar techniques will prove successful in enhancing the fast imaging capabilities of all-optical photoacoustic tomography.

Bibliography

- Abu-Safia, H. et al. (1994). "Transmission of a Gaussian beam through a Fabry–Perot interferometer". In: *Appl. Opt.* 33.18, pp. 3805–3811.
- Barykina, Natalia V et al. (2017). "Green fluorescent genetically encoded calcium indicator based on calmodulin/M13-peptide from fungi". In: *PloS one* 12.8, e0183757.
- Beard, Paul C, Frederic Perennes, and Tim N Mills (1999). "Transduction mechanisms of the Fabry-Perot polymer film sensing concept for wideband ultrasound detection". In: *IEEE Trans. Ultrason. Ferroelectr. Freq. Control* 46.6, pp. 1575–1582.
- Bond, Charlotte et al. (July 2011). "Higher order Laguerre-Gauss mode degeneracy in realistic, high finesse cavities". In: *Phys. Rev. D* 84.
- Bond, Charlotte Zoë (2014). "How to stay in shape: overcoming beam and mirror distortions in advanced gravitational wave interferometers". PhD thesis. University of Birmingham.
- Booth, Martin J (2007). "Adaptive optics in microscopy". In: *Philosophical Transactions of the Royal Society A: Mathematical, Physical and Engineering Sciences* 365.1861, pp. 2829–2843.
- (2014). "Adaptive optical microscopy: the ongoing quest for a perfect image". In: *Light: Science & Applications* 3.4, e165–e165.
- Buchmann, Jens et al. (2017). "Characterization and modeling of Fabry–Perot ultrasound sensors with hard dielectric mirrors for photoacoustic imaging". In: *Appl. Opt.* 56.17, pp. 5039–5046.
- Chen, Bohua, Yuwen Chen, and Cheng Ma (2020). "Photothermally tunable Fabry–Pérot fiber interferometer for photoacoustic mesoscopy". In: *Biomed. Opt. Express* 11.5, pp. 2607–2618.
- Costantini, Irene et al. (2019). "In-vivo and ex-vivo optical clearing methods for biological tissues". In: *Biomedical optics express* 10.10, pp. 5251–5267.
- Cui, Manxiu et al. (2020). "Adaptive photoacoustic computed tomography". In: *Photoacoustics*, p. 100223. ISSN: 2213-5979.
- Cutrale, Francesco et al. (2017). "Hyperspectral phasor analysis enables multiplexed 5D in vivo imaging". In: *Nature methods* 14.2, pp. 149–152.
- Czuchnowski, Jakub and Robert Prevedel (2020). "Improving the Sensitivity of Planar Fabry-Pérot Cavities via Adaptive Optics and Mode Filtering". In: *Advanced Optical Materials*, p. 2001337.
- (2021). "Adaptive optics enhanced all-optical photoacoustic tomography". In: *bioRxiv:2021.01.13.426260*.
- Dana, Hod et al. (2016). "Sensitive red protein calcium indicators for imaging neural activity". In: *elife* 5, e12727.
- Deliolanis, Nikolaos et al. (2007). "Free-space fluorescence molecular tomography utilizing 360 geometry projections". In: *Optics letters* 32.4, pp. 382–384.
- Dong, Biqin, Cheng Sun, and Hao Zhang (2016). "Optical detection of ultrasound in photoacoustic imaging". In: *IEEE Transactions on Biomedical Engineering* PP.99. ISSN: 15582531.
- Eils, Roland and Chaitanya Athale (2003). "Computational imaging in cell biology". In: *The Journal of cell biology* 161.3, pp. 477–481.

- Fenster, Aaron, Donal B Downey, and H Neale Cardinal (2001). "Three-dimensional ultrasound imaging". In: *Physics in medicine & biology* 46.5, R67.
- Flood, Merrill M (1956). "The traveling-salesman problem". In: *Operations research* 4.1, pp. 61–75.
- Fred, Herbert L (2004). "Drawbacks and limitations of computed tomography: views from a medical educator". In: *Texas Heart Institute Journal* 31.4, p. 345.
- Fuenzalida Werner, Juan Pablo et al. (2020). "Challenging a Preconception: Optoacoustic Spectrum Differs from the Optical Absorption Spectrum of Proteins and Dyes for Molecular Imaging". In: *Analytical Chemistry* 92.15. PMID: 32640156, pp. 10717–10724.
- Gao, Liang et al. (2013). "Photothermal bleaching in time-lapse photoacoustic microscopy". In: *Journal of biophotonics* 6.6-7, pp. 543–548.
- Gatto, ALBERTO et al. (2014). "Fabry-Pérot-Michelson interferometer using higher-order Laguerre-Gauss modes". In: *Phys. Rev. D* 90.12, p. 122011.
- Glatz, Jürgen et al. (2011). "Blind source unmixing in multi-spectral optoacoustic tomography". In: *Optics express* 19.4, pp. 3175–3184.
- Goda, K, KK Tsia, and B Jalali (2009). "Serial time-encoded amplified imaging for real-time observation of fast dynamic phenomena". In: *Nature* 458.7242, pp. 1145–1149.
- Goda, Keisuke and Bahram Jalali (2013). "Dispersive Fourier transformation for fast continuous single-shot measurements". In: *Nature Photonics* 7.2, pp. 102–112.
- Goodfellow, Ian et al. (2016). *Deep learning*. Vol. 1. 2. MIT press Cambridge.
- Gottschalk, Sven et al. (2019). "Rapid volumetric optoacoustic imaging of neural dynamics across the mouse brain". In: *Nature biomedical engineering* 3.5, pp. 392–401.
- Guggenheim, James A et al. (2017). "Ultrasensitive plano-concave optical microresonators for ultrasound sensing". In: *Nature Photonics* 11.11, pp. 714–719.
- Gusev, Vitalii E and Aleksandr A Karabutov (1991). *Laser optoacoustics*. Vol. 93, p. 16842.
- Gwosch, Klaus C et al. (2020). "MINFLUX nanoscopy delivers 3D multicolor nanometer resolution in cells". In: *Nature methods* 17.2, pp. 217–224.
- Hoffman, Karla L, Manfred Padberg, Giovanni Rinaldi, et al. (2013). "Traveling salesman problem". In: *Encyclopedia of operations research and management science* 1, pp. 1573–1578.
- Ida, T., M. Ando, and H. Toraya (2000). "Extended pseudo-Voigt function for approximating the Voigt profile". In: *Journal of Applied Crystallography* 33.6, pp. 1311–1316.
- "IEC 60825–1, Radiation Safety of Laser Products and Systems" (1994). In: *British Standards Institute* 2.
- Janssen, Augustus J. E. M. (2002). "Extended Nijboer-Zernike approach for the computation of optical point-spread functions". In: *J. Opt. Soc. Am. A* 19.5, pp. 849–857.
- Jathoul, Amit P et al. (2015). "Deep in vivo photoacoustic imaging of mammalian tissues using a tyrosinase-based genetic reporter". In: *Nat. Photonics* 9.4, p. 239.
- Jensen, Mikkel et al. (2019). "Noise of supercontinuum sources in spectral domain optical coherence tomography". In: *JOSA B* 36.2, A154–A160.
- Ji, Na (2017). "Adaptive optical fluorescence microscopy". In: *Nat. Methods* 14.4, pp. 374–380.
- Kerruth, Silke et al. (2019). "The kinetic mechanisms of fast-decay red-fluorescent genetically encoded calcium indicators". In: *Journal of Biological Chemistry* 294.11, pp. 3934–3946.

- Kherlopiyan, Armen R et al. (2008). "A review of imaging techniques for systems biology". In: *BMC systems biology* 2.1, pp. 1–18.
- Kim, Jongbeom et al. (2019). "Super-resolution localization photoacoustic microscopy using intrinsic red blood cells as contrast absorbers". In: *Light: Science & Applications* 8.1, pp. 1–11.
- Krull, Alexander, Tim-Oliver Buchholz, and Florian Jug (2018). *Noise2Void - Learning Denoising from Single Noisy Images*. arXiv: [1811.10980](https://arxiv.org/abs/1811.10980).
- Lashkari, Bahman and Andreas Mandelis (2010). "Photoacoustic radar imaging signal-to-noise ratio, contrast, and resolution enhancement using nonlinear chirp modulation". In: *Optics letters* 35.10, pp. 1623–1625.
- LeCun, Yann, Yoshua Bengio, and Geoffrey Hinton (2015). "Deep learning". In: *nature* 521.7553, pp. 436–444.
- Lehtinen, Jaakko et al. (2018). "Noise2noise: Learning image restoration without clean data". In: *arXiv preprint arXiv:1803.04189*.
- Lin, Li et al. (2015). "In vivo photoacoustic tomography of myoglobin oxygen saturation". In: *Journal of Biomedical Optics* 21.6, pp. 1–5.
- Liu, Gangjun et al. (2012). "A comparison of Doppler optical coherence tomography methods". In: *Biomedical optics express* 3.10, pp. 2669–2680.
- Liu, Wei and Joseph J Talghader (2006). "Spatial-mode analysis of micromachined optical cavities using electrothermal mirror actuation". In: *J. Microelectromech. Syst.* 15.4, pp. 777–785.
- Loudon, Rodney and Peter L Knight (1987). "Squeezed light". In: *Journal of modern optics* 34.6-7, pp. 709–759.
- Lustig, Michael, David Donoho, and John M Pauly (2007). "Sparse MRI: The application of compressed sensing for rapid MR imaging". In: *Magnetic Resonance in Medicine: An Official Journal of the International Society for Magnetic Resonance in Medicine* 58.6, pp. 1182–1195.
- Mah, Merlin L. and Joseph J. Talghader (2019). "Decomposition of aberrated or turbulent wavefronts into a spatial mode spectrum using optical cavities". In: *Appl. Opt.* 58.16, pp. 4288–4299.
- Mahajan, Virendra N (1994). "Zernike circle polynomials and optical aberrations of systems with circular pupils". In: *Applied optics* 33.34, pp. 8121–8124.
- (1995). "Zernike-Gauss polynomials and optical aberrations of systems with Gaussian pupils". In: *Applied optics* 34.34, pp. 8057–8059.
- Mahjoubfar, Ata et al. (2013). "Label-free high-throughput cell screening in flow". In: *Biomedical optics express* 4.9, pp. 1618–1625.
- Manwar, Rayyan, Karl Kratkiewicz, and Kamran Avanaki (2020). "Overview of ultrasound detection technologies for photoacoustic imaging". In: *Micromachines* 11.7, p. 692.
- Marques, Dylan M. et al. (2020). "Modelling Fabry-Pérot etalons illuminated by focussed beams". In: *Opt. Express* 28.5, pp. 7691–7706.
- Mishin, Alexander S et al. (2015). "Novel uses of fluorescent proteins". In: *Current opinion in chemical biology* 27, pp. 1–9.
- Moon, Suabei and Dug Young Kim (2007). "Normalization detection scheme for high-speed optical frequency-domain imaging and reflectometry". In: *Optics express* 15.23, pp. 15129–15146.
- Morris, Paul et al. (2009). "A Fabry-Pérot fiber-optic ultrasonic hydrophone for the simultaneous measurement of temperature and acoustic pressure". In: *The Journal of the Acoustical Society of America* 125.6, pp. 3611–3622.
- Mouradian, L Kh et al. (2000). "Spectro-temporal imaging of femtosecond events". In: *IEEE journal of quantum electronics* 36.7, pp. 795–801.

- Ntziachristos, Vasilis (2010). "Going deeper than microscopy: the optical imaging frontier in biology". In: *Nature Methods* 7.8, pp. 603–614. ISSN: 1548-7091.
- Ntziachristos, Vasilis and Daniel Razansky (2010). "Molecular imaging by means of multispectral optoacoustic tomography (MSOT)". In: *Chemical reviews* 110.5, pp. 2783–2794.
- Overwijk, Willem W and Nicholas P Restifo (2000). "B16 as a mouse model for human melanoma". In: *Current protocols in immunology* 39.1, pp. 20–1.
- Ozturk, Mehmet S et al. (2013). "Mesoscopic fluorescence molecular tomography of reporter genes in bioprinted thick tissue". In: *Journal of biomedical optics* 18.10, p. 100501.
- Prahl, Scott (1998). *Tabulated Molar Extinction Coefficient for Hemoglobin in Water*. URL: <https://omlc.org/spectra/hemoglobin/summary.html>.
- Prevedel, Robert et al. (2014). "Simultaneous whole-animal 3D imaging of neuronal activity using light-field microscopy". In: *Nature methods* 11.7, pp. 727–730.
- Qian, Yong et al. (2019). "A genetically encoded near-infrared fluorescent calcium ion indicator". In: *Nature methods* 16.2, pp. 171–174.
- Sears, Francis Weston (1949). *Optics*. Cambridge, USA: Addison-Wesley, 369, [16] p.
- Speirs, Rory W and Alexis I Bishop (2013). "Photoacoustic tomography using a Michelson interferometer with quadrature phase detection". In: *Applied Physics Letters* 103.5, p. 053501.
- Stelzer, Ernst HK (2015). "Light-sheet fluorescence microscopy for quantitative biology". In: *Nature methods* 12.1, pp. 23–26.
- Takeno, Kohei et al. (2011). "Determination of wavefront aberrations using a Fabry–Perot cavity". In: *Opt. Commun.* 284.13, pp. 3197–3201. ISSN: 0030-4018.
- Tian, Chao et al. (2021). "Spatial Resolution in Photoacoustic Computed Tomography". In: *Reports on Progress in Physics*.
- Trappe, Neil, J Anthony Murphy, and Stafford Withington (2003). "The Gaussian beam mode analysis of classical phase aberrations in diffraction-limited optical systems". In: *Eur. J. Phys.* 24.4, p. 403.
- Treeby, Bradley E and Benjamin T Cox (2010). "k-Wave: MATLAB toolbox for the simulation and reconstruction of photoacoustic wave fields". In: *Journal of biomedical optics* 15.2, p. 021314.
- Treeby, Bradley E, Edward Z Zhang, and Benjamin T Cox (2010). "Photoacoustic tomography in absorbing acoustic media using time reversal". In: *Inverse Problems* 26.11, p. 115003.
- Treeby, Bradley E et al. (2011). "Automatic sound speed selection in photoacoustic image reconstruction using an autofocus approach". In: *Journal of biomedical optics* 16.9, p. 090501.
- Tsigaridas, G et al. (2003). "Z-scan analysis for near-Gaussian beams through Hermite–Gaussian decomposition". In: *J. Opt. Soc. Am. B* 20.4, pp. 670–676.
- Varu, HS (2014). "The optical modelling and design of Fabry Perot Interferometer sensors for ultrasound detection". PhD thesis. UCL (University College London).
- Vaughan, M (2017). *The Fabry-Perot interferometer: history, theory, practice and applications*. Routledge.
- Villringer, Claus et al. (2019). "Development of tuneable Fabry-Pérot sensors for parallelised photoacoustic signal acquisition". In: *Photons Plus Ultrasound: Imaging and Sensing 2019*. Ed. by Alexander A. Oraevsky and Lihong V. Wang. Vol. 10878. International Society for Optics and Photonics. SPIE, pp. 28–33.
- Wagner, Nils et al. (2019). "Instantaneous isotropic volumetric imaging of fast biological processes". In: *Nature methods* 16.6, pp. 497–500.

- Watson, J et al. (1998). "The traveling salesrep problem, edge assembly crossover, and 2-opt". In: *International Conference on Parallel Problem Solving from Nature*. Springer, pp. 823–832.
- Wells, Peter NT (2006). "Ultrasound imaging". In: *Physics in Medicine & Biology* 51.13, R83.
- Wen, Xiang et al. (2010). "In vivo skin optical clearing by glycerol solutions: mechanism". In: *Journal of biophotonics* 3.1-2, pp. 44–52.
- Wissmeyer, Georg et al. (2018). "Looking at sound: optoacoustics with all-optical ultrasound detection". In: *Light Sci. Appl.* 7.1, pp. 1–16.
- Xia, Jun and Lihong V Wang (2013). "Small-animal whole-body photoacoustic tomography: a review". In: *IEEE Transactions on Biomedical Engineering* 61.5, pp. 1380–1389.
- Yang, Changchun et al. (2021). "Review of deep learning for photoacoustic imaging". In: *Photoacoustics* 21, p. 100215.
- Zarowny, Landon et al. (2020). "Bright and high-performance genetically encoded Ca²⁺ indicator based on mNeonGreen fluorescent protein". In: *ACS sensors* 5.7, pp. 1959–1968.
- Zhang, Edward, Jan Laufer, and Paul Beard (2008). "Backward-mode multiwavelength photoacoustic scanner using a planar Fabry-Perot polymer film ultrasound sensor for high-resolution three-dimensional imaging of biological tissues". In: *Appl. Opt.* 47.4, pp. 561–577.
- Zhang, Hao F et al. (2006). "Functional photoacoustic microscopy for high-resolution and noninvasive in vivo imaging". In: *Nature biotechnology* 24.7, pp. 848–851.